Orbital Engineering of Pulsed Laser Deposited Single-layered Manganite Thin Films

TECHNISCHE
UNIVERSITÄT
DARMSTADT

Fachbereich Material- und Geowissenschaften

genehmigte
Dissertation

zur Erlangung des akademischen Grades
eines Doktors der Ingenieurwissenschaften (Dr.-Ing.)

von

M.Sc. Mehran Vafaee Khanjani
geboren in Rasht, Iran

Darmstadt 2014
D 17

Prüfungskommitee:
1. Referent: Prof. Dr. Lambert Alff
2. Referent: Prof. Dr. Wolfgang Donner
Prüfer: Prof. Dr. Wolfgang Ensinger
Prüfer: Prof. Dr. Barbara Albert

Tag der Einreichung: 25.08.2013
Tag der Disputation: 29.11.2013

to my beautiful wife
for her support and indescribable love

to my mother and father and my sister
for their life-long love and help

Eidesstattliche Erklärung

Ich erkläre hiermit an Eides Statt, dass ich die vorliegende Arbeit selbständig sowie ohne unzulässige Hilfe Dritter und ohne Benutzung anderer als der angegebenen Hilfsmittel angefertigt habe. Die aus anderen Quellen direkt oder indirekt übernommenen Daten und Konzepte sind unter Angabe der Quelle gekennzeichnet.

Mehran Vafaee Khanjani Darmstadt, September 2014

Curriculum Vitae

Mehran Vafaee Khanjani, born on September 22nd 1980 in Rasht, Iran.

- September 1998 - August 2003, B. Sc. in Material Engineering
  Imam Khomeini International University, Material Engineering Dept.

- September 2003 - December 2005, M. Sc. in Material Science & Engineering
  Sharif University of Technology, Material Science Dept.
  Thesis: Liquid phase synthesis of ZnO nanopowders

- October 2009 - November 2013, PhD in Material Science
  Technical University of Darmstadt, Fachbereich Materialwiessenschft
  Thesis: Strain-induced Orbital Engineering of Pulsed Laser Deposited Single-layered Manganite Thin Film

- From October 2013, PosDoc
  Johannes Gutenberg University of Mainz, Institut für Physik

Content

Abstract

Single-layered manganite, $La_{1-x}Sr_{1+x}MnO_4$, crystallizes in a tetragonal structure in which (La, Sr)O layers separate MnO_6 octahedra along the *c* axis providing 2D MnO_2 sheets. Within this structure, anisotropic electrical resistivity was observed where the in-plane resistivity at room temperature is about three orders of magnitude smaller than the out-of-plane counterpart. In perovskite manganites, $La_{1-x}Sr_xMnO_3$, doping Sr turns insulating $LaMnO_3$ to metallic $La_{0.5}Sr_{0.5}MnO_3$ due to double exchange interaction. On the contrary, the tetragonal $La_{1-x}Sr_{1+x}MnO_4$ remains insulating at higher doping levels of Sr, although the resistivity reduces by about one order of magnitude. Herein, the insulating state of $LaSrMnO_4$ endures via doping with Sr up to x=0.5 and a charge-orbital order state forms where the Mn^{3+} cations show a preferential orbital occupation of $d_{3x^2-r^2}$ and $d_{3y^2-r^2}$.

Many investigations of perovskite manganites have shown that preferential orbital occupation and charge localization *i.e.* charge order, are interrelated with crystal structure. In this context, the key points are the Mn-O bond length, the cooperative rotation of MnO_6 octahedra and the Jahn-Teller distortion. These factors define whether the charge-orbital state is favorable or not. Owing to the layered structure of $La_{1-x}Sr_{1+x}MnO_4$, tilting the MnO_6 octahedra is restricted (no Mn-O-Mn bond along the *c* axis).

In this thesis two doping levels of x=0.0 and x=0.5 were chosen in which the MnO_6 octahedra are tetragonally distorted and non-distorted, respectively. The growth of thin films on different single-crystalline substrates allows us to alter the in- and out-of-plane lattice constants; to change the bond length of Mn with apical and planar oxygen atoms. In such a way, for each specific doping level, Mn^{3+} cations may show different orbital occupation than the one recognized in the bulk or single crystal. Indeed several studies have manifested preferential $d_{3z^2-r^2}$ or $d_{x^2-y^2}$ orbitals for Mn^{3+} cations in $La_{1-x}Sr_xMnO_3$ films under in-plane compressive or tensile strains, respectively, although there is no preferential orbital occupation for Mn^{3+} cations in bulk or single crystal of $La_{1-x}Sr_xMnO_3$.

In this study the thin films of $La_{1-x}Sr_{1+x}MnO_4$ (x=0.0, 0.5) were deposited on different substrates in order to generate in-plane tensile and compressive strains. The details of the thin film deposition conditions are given in section 2.4. The crystal parameters of the films were investigated carefully using x-ray diffraction techniques presented in sections 3.4 and 3.5. The stoichiometry of the films and oxidation state of Mn cations were investigated using x-ray photoelectron spectroscopy as shown in sections 4.3 and 4.4. The orbital occupation of Mn cations was studied by means of linearly polarized x-ray absorption spectroscopy where electron density in the valence shell of Mn cations was probed with respect to the

crystallographic direction. In this fashion, the orbital occupation along the in- and out-of-plane directions could be inspected. Our findings show that preferential orbital occupation in layered manganites on one the hand depends on the doping level, while on the other hand they are robust against artificially applied strain. The former is expected since the energy band level is a function of the electron density of Mn cations. However, unlike perovskite manganites, the artificial strain does not affect the orbital occupation. Such differentiation between doping levels and artificial strain can, based on our findings, be addressed only in the thin film of layered manganites, as in the Perovskite family members the strain can be compensated by rotation of MnO_6 octahedra, a feature which is absent in layered structures. The details of the linearly polarized x-ray absorption spectroscopy measurements are given in section 5.

Introduction

1.1. Fundamentals of Electronic and Crystal Structures of Perovskite Manganites

Perovskite structure with general formula of $\boldsymbol{AB}O_3$ is composed of ***A***-site cations on the corners, ***B***-site cations in the center and oxygen atoms on the faces of a cubic structure (Figure 1). The ***A***-site cations are usually the alkaline earth metals or lanthanides or a mixture of both. The ***B***-site, on the other hand, can be occupied by almost all the transition metals.

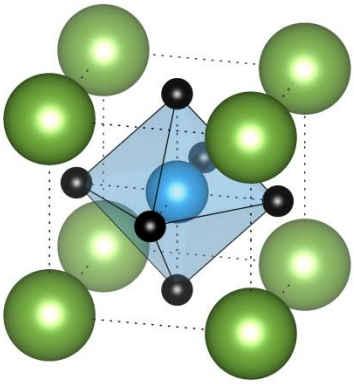

Figure 1: Cubic perovskite structure in which the ***B***-site cation (blue) is surrounded by six oxygen atoms (black) in an octahedra symmetry, while ***A***-site cations (green) occupy the corners.

The ***B***-site cation (transition metal) is surrounded by 6 oxygen atoms in an octahedral symmetry. Part of electrons in valence shell of transition metals are distributed in *d* orbital which splits into t_{2g} and e_g orbitals in octahedral symmetry due to crystal field splitting [1] shown in Figure 2. Crystal field splitting describes breaking of degeneracy in *d* and *f* orbitals in a system involving ligands [2]. Negatively charged ligands are considered as point charges, thus, in such system, the positively charged cations are surrounded by an array of point charges. In this way, the strength of hybridization between the cations and the ligands is not the same everywhere, which is actually the origin of breaking the degeneracy. As a result in an octahedral symmetry, the t_{2g} (d_{xz}, d_{yz}, d_{xy}) orbitals place at lower energy than the e_g $(d_{3z^2-r^2}, d_{x^2-y^2})$ orbitals by crystal field splitting energy (Δ_{oct}) (Figure 2).

Electrons reside in t_{2g} or e_g, the one which removes the degeneracy by lowering the symmetry (lowering the energy). For the undoped perovskite manganite, $La_{1-x}Sr_xMnO_3$ (x=0.0), the oxidation state of Mn is +3 with valence shell configuration of d^4 $\left(t_{2g}^3 e_g^1\right)$. If the e_g electrons occupy the $d_{3z^2-r^2}$ orbitals (z-axis elongated), the electron density will be mostly concentrated along the z axis. Thus, there will be greater Coulomb repulsion associated with the bond

between Mn with the apical oxygen atoms rather than the planar oxygen atoms[1]. Such preference in occupation of a certain orbital replicates itself in crystal structure as a distortion in MnO_6 octahedra, known as Jahn-Teller distortion [3].

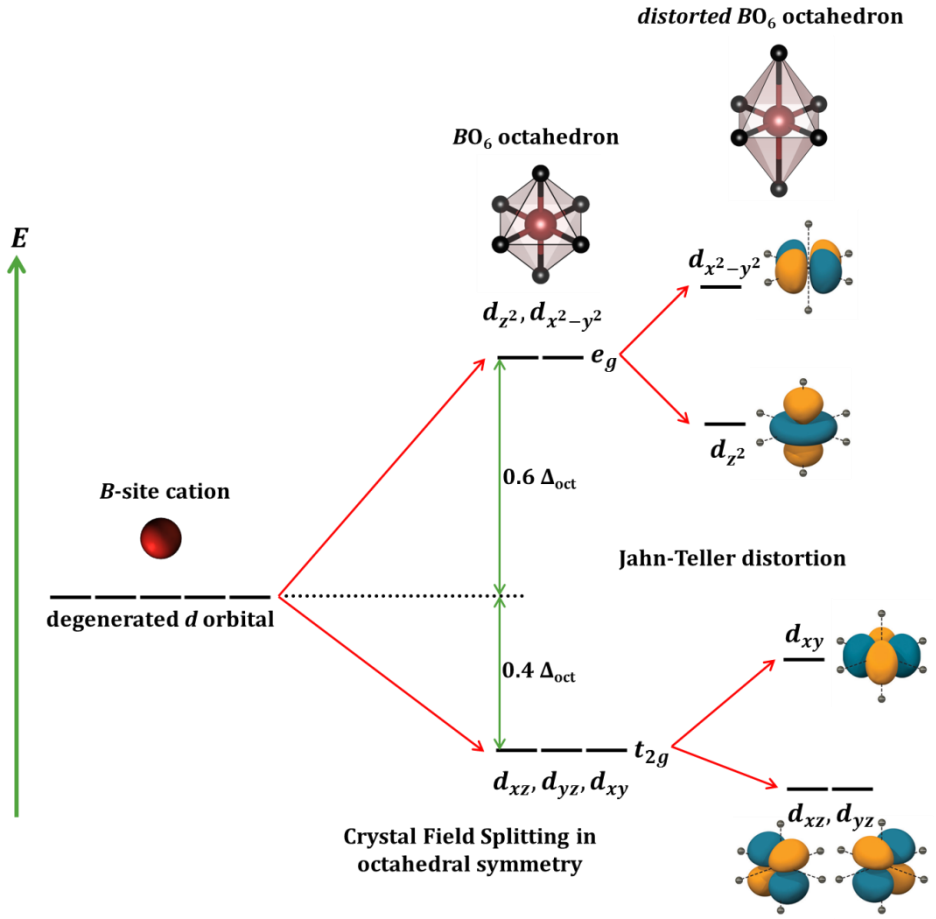

Figure 2: Breaking the degenerate 5-fold *d* orbital of transition metals to doubly degenerate e_g and triply degenerate t_{2g} orbitals due to crystal field splitting with energy difference of Δ_{oct}. In the octahedral symmetry, t_{2g} orbital is at lower energy than e_g orbital. The Jahn-Teller distortion is the splitting of the t_{2g} and e_g orbitals in favor of the *z*-axis elongated orbital occupation.

For high spin state of d^4 configuration (owing one unpaired e_g electron), the Jahn-Teller effect is the most pronounced comparing to the other *d* shell configurations. Doping perovskite manganite $La_{1-x}Sr_xMnO_3$ with Sr, increases the valence state of Mn where at (x=0.5), the ratio of Mn^{3+}/Mn^{4+} becomes one. Since Mn^{4+} (d^3) is Jahn-Teller inactive (lack of e_g electron), higher concentration of Mn^{4+} discourages the Jahn-Teller distortion in MnO_6 octahedra.

Perovskite manganites crystallize in structures with lower symmetry than cubic structure. Such crystal structure modifications originate from different sources. Firstly, Jahn-Teller

[1] The oxygen on the *z* axis of octahedron are called apical oxygen atoms, while the ones on the *x* and *y* axes are known as planar oxygen atoms.

distortion in MnO_6 octahedra modifies the structure to orthorhombic (Figure 3) where the Mn-O bond length is dissimilar in different crystal orientations leading to unequal a, b and c lattice constants. Secondly, dissimilar Mn-O and $\boldsymbol{A}$-O bond lengths modifies the structure by an equivalent rotation of MnO_6 octahedra resulting in a rhombohedral structure. Confirmed by neutron scattering measurements, orthorhombic and rhombohedral structures are the two common crystal structures for perovskite manganites [4-7].

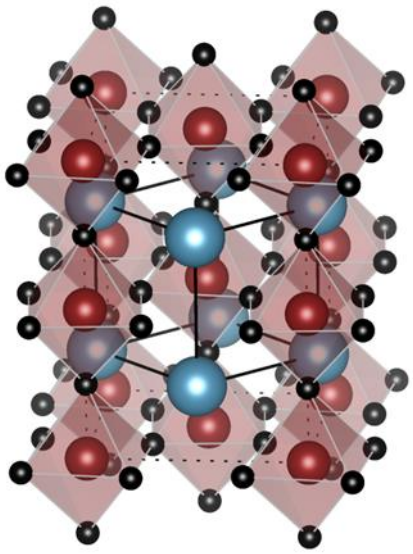

Figure 3: Perovskite structure of manganite where the color scheme of La/Sr, Mn, and O is blue, red, and black, respectively. The so-called pseudoperovskite cubic unit cell (solid black lines), is cut from the orthorhombic unit cell of $La_{1-x}Sr_xMnO_3$ (dotted black lines).

For perovskites, Goldschmidt tolerance factor (t) estimates the stability of the crystal structures depending on $\boldsymbol{A}$-and $\boldsymbol{B}$-site ionic radii:

$$t = \frac{r_{\boldsymbol{A}} + r_O}{\sqrt{2}(r_{\boldsymbol{B}} + r_O)} \qquad (1)$$

where r is the corresponding ionic radius. For the tolerance factors of $0.9 < t < 1$, the structure is cubic. Lower tolerance factor values of $0.7 < t < 0.9$ correspond to lower symmetries such as orthorhombic and rhombohedral [8]. Based on firstly, rare earth (RE) to alkaline earth (AE) ratio in $RE_{1-x}AE_xMnO_3$ and secondly, the average cations' radii, the crystal structure can be estimated regarding Jahn-Teller distortion and tolerance factor.

Electrical transport properties in manganites are highly related to the crystal structure where higher the distortion of MnO_6 octahedra (lower the tolerance factor) is, lower the electric conductance is. Therefore, as the doping level of AE cation increases (the tolerance factor decreases), the material shows more metallic transport properties. It has been shown that independent of the type of $\boldsymbol{A}$-site cations, by increasing the ionic radius, the insulating state suppresses and metalicity develops [9, 10].

For instance, the undoped manganite $LaMnO_3$, is an antiferromagnet insulator where the electrons spin of Mn^{3+} cations align antiferromagnetically in A-type configuration[2]. Super-exchange model which was developed by Goodenough [11] describes the antiferromagnetic order. Doping the structure with holes (AE cations) induces a ferromagnetic interaction through Mn^{3+}-O-Mn^{4+} described by double-exchange model. In the double exchange model suggested by Zener [12], the t_{2g} electrons are localized, and the conduction occurs via the hopping of e_g electrons of Mn^{3+} (d^4) through the oxygen atoms, to the empty e_g orbitals of Mn^{4+} (d^3). The effective hopping interaction t^{eff} can be expressed with reduced form of Anderson-Hasegawa relation [13] as follows:

$$t^{eff} = t_{ij}^0 \cos(\theta_{ij}/2) \qquad (2)$$

where t_{ij}^0 is the intersite hopping interaction of e_g electron between two neighboring i and j sites and θ_{ij} is the angle between the two adjacent sites. Therefore, deviation of $\theta_{ij,}$ from 180° upon rotation of octahedra affects the effective intersite hopping of the e_g electrons. In addition, a successful hopping depends on the spin configuration of neighboring sites. Accordingly, loss of conductivity near or at Curie temperature (T_C) can be expressed by the fact that due to thermally induced fluctuation of the spins, the amount of the effective hopping reduces.

The manganite has been in the center of research as magnetoresistive compounds. They show a large negative magnetoresistance (MR) which is the decrease in resistance induced by external magnetic field. The term colossal MR (CMR) has been given to manganites as comparing to giant MR (GMR) compounds, they show considerably larger MR derived by the following equation:

$$MR = \frac{[\rho(H) - \rho(0)]}{\rho(0)} \qquad (3)$$

[2] The spin structure forms in either ferromagnetic (FM) or antiferromagnetic (AFM) order. This is defined based on the strength of ferromagnetic or antiferromagnetic coupling energy (J_{FM} or J_{AFM}). In the figure below, FM and AFM spin orders are schematically illustrated. In the A-type AFM, the spin order along in- and out-of-plane directions are FM and AFM, respectively. This configuration for the C-type AFM is completely opposite where spin order along in- and out-of-plane directions are AFM and FM, respectively. In G-type AFM, all the spins align in AFM order. When J_{FM} and J_{AFM} are comparable, a canted FM or AFM order occurs. Moving from FM to G-type AFM, the strength of J_{FM} (J_{AFM}) decreases (increases).

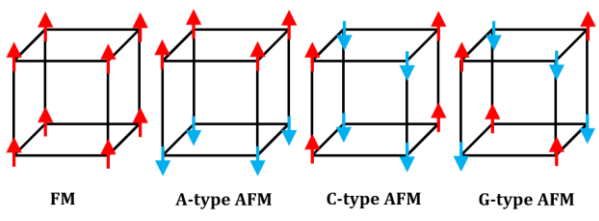

Doping the canonical manganite compound $La_{1-x}Sr_xMnO_3$, with Sr up to x=0.175 turns the antiferromagnetic insulator $LaMnO_3$ to a ferromagnetic metal with a metal-insulator (M-I) transition at $T_C = 283$ K [14] shown in Figure 4.

Increasing the doping level elevates the M-I transition temperature. The most studied family member of this series is $La_{1-x}Sr_xMnO_3$ (x=0.3) with T_C = 380 K. As it is shown in Figure 4 (right), the M-I transition temperature coincides with T_C. The compounds with M-I transition *i.e.* $x = 0.15, 0.175, 0.2, 0.3$ (Figure 4) show almost isotropic negative *MR* up to 100% near the corresponding T_C. The M-I transition has been attributed to charge carrier scattering due to thermal spin fluctuations [14].

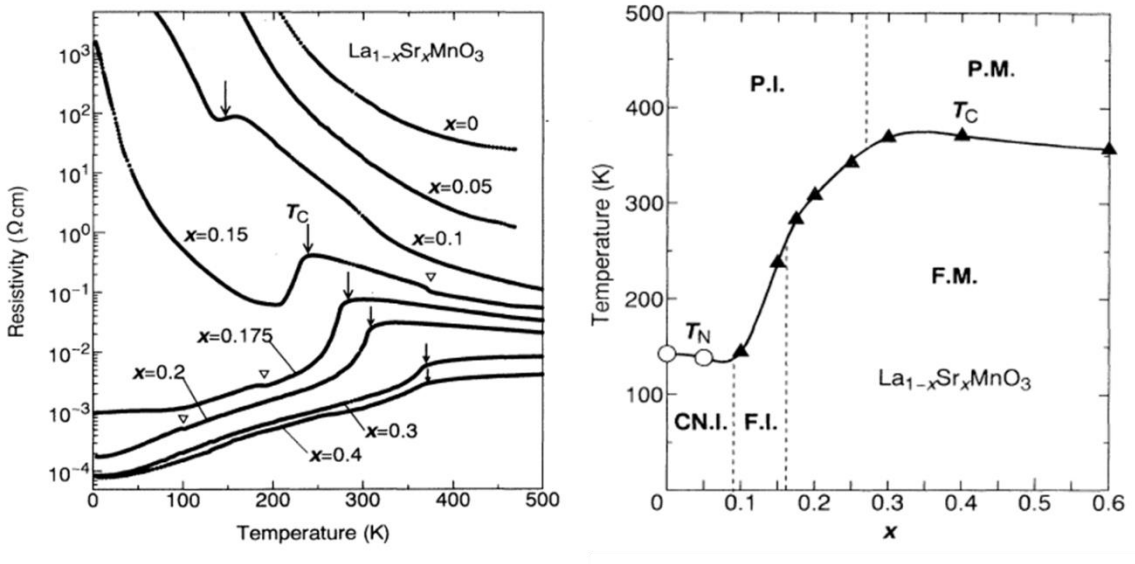

Figure 4: (left) Temperature dependence resistivity curves of $La_{1-x}Sr_xMnO_3$. The arrows indicate the Curie temperature T_C; (right) Electronic phase diagram of $La_{1-x}Sr_xMnO_3$ where open circles and filled triangles represent the Néel (T_N) and Curie temperatures. CN.I., F.I., F.M., P.I., and P.M. represent canted ferromagnetic insulator, ferromagnetic insulator, ferromagnetic metal, paramagnetic insulator, paramagnetic metal, respectively [14].

Spin alignment by external magnetic field causes reduction in resistivity suggesting the spin fluctuation as the origin of M-I transition.

Figure 5 Compares electronic and magnetic phase diagram with crystal structure phase diagram [15] revealing a strong correlation between spin, charge and crystal structures. The orthorhombic phase region coincides with the insulating antiferromagnetic phase. This is where Jahn-Teller distortion plays the major role. At higher doping levels, the metallic ferromagnetic phase possesses the rhombohedral structure. As shown in Figure 5 (right), transition from orthorhombic to rhombohedral structure forms an intermediate O* region. The compounds with the doping levels of $0.15 < x < 0.2$ which fall into the O* region actually show the largest M-I transition. X-ray powder diffraction measurements of these members show an orthorhombic structure with suppressed Jahn-Teller distorted MnO_6 octahedra [15].

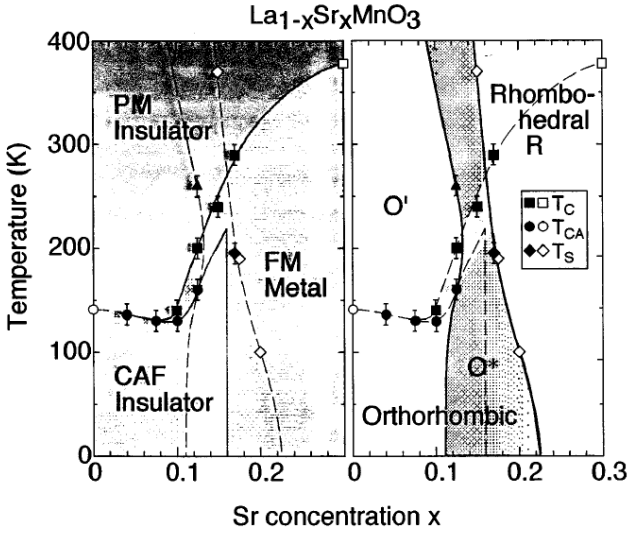

Figure 5: (left) Electronic and magnetic phase diagram; (right) Structural phase diagram of $La_{1-x}Sr_xMnO_3$.

The correlation between electronic and magnetic with crystal structure suggests that the emergence of M-I transition is the competition between localized electrons in Jahn-Teller distorted octahedra (orthorhombic structure) and charge carriers in cooperative rotated octahedra (rhombohedral structure).

1.2. The Ruddlesden-Popper series of Manganites

The Ruddlesden-Popper series (layered perovskite) of manganites have the general formula of $(RE, AE)_{n+1}Mn_nO_{3n+1}$ in which n represents the number of extra (RE, AE)O-layers in comparison to perovskite manganites. The extra layers isolate n layers of MnO_6 octahedra along the z direction. The schematic view of the crystal structure of Ruddlesden-Popper series of manganites is shown in Figure 6.

In single-layered manganites (n=1), every single MnO_2 sheet is isolated acquiring an absolute 2D network of MnO_6 octahedra. Many interesting physical phenomena such as two dimensional electron gas or exchange bias at the interface of an antiferromagnet and a ferromagnet layers have been observed in 2D confined matrices. The effective hopping of e_g electrons, as it was introduced in previous section, is a measure for transport properties. Such hopping in single-layered manganites, therefore, is restricted and eliminated by one dimension. Similarly, the spin interactions are stronger within the planes rather than interplanes. In fact, the 2D systems behave quit differently and many stunning phenomena such as colossal magnetoresistance and charge-orbital ordering have been observed in 2D layered manganites. For example, double-layered manganite (n=2) are known as the systems which show a colossal MR up to four orders of magnitude at their M-I transition temperatures. In these manganites, two MnO_2 sheets are

apically connected obtaining a miniaturized 3D network embedded in a 2D matrix. Increasing the number of isolated layers transforms gradually the 2D network of MnO_6 octahedra to a 3D one which, of course, affects the spin, charge and orbital degrees of freedom and in its microscopic scale, the magnetic and electronic properties.

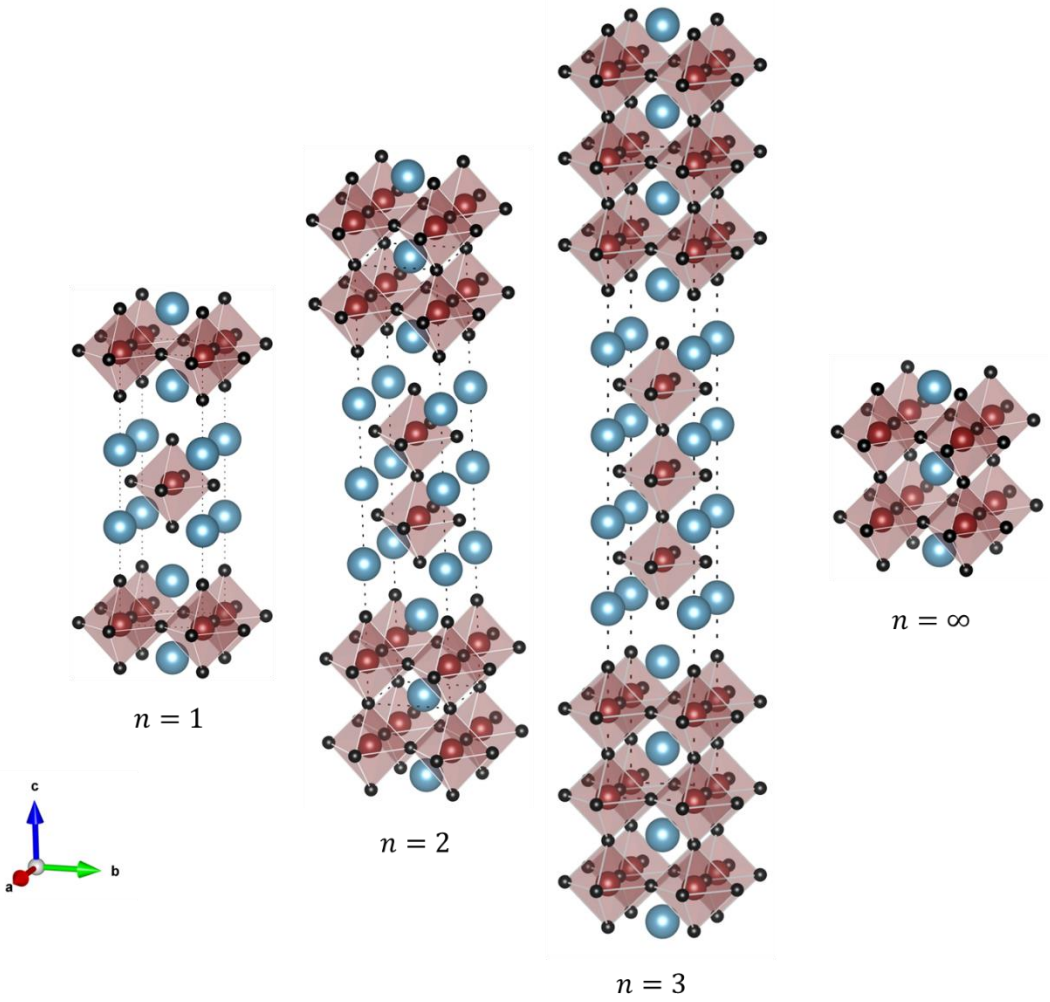

Figure 6: Schematic view of crystal structure of n=1, 2, and 3 Ruddlesden-Popper series members of manganites along with perovskite manganite (in other words, infinite number of isolated MnO_6 layers). Manganese, oxygen and ***A***-site cations are shown in red, black and blue color scheme, respectively.

In the next section, a brief review on double-layered manganite, $RE_{2-2x}AE_{1+2x}Mn_2O_7$, will be given followed by a short review on crystal, magnetic and electronic structures of single-layered manganites, $La_{1-x}Sr_{1+x}MnO_4$.

1.2.1. Double-layered Manganites: A Brief Review

The discovery of giant magnetoresistance has opened up a variety of spintronics applications by development of several devices functioning on the basis of magnetic tunnel junction multilayers *i.e.* ferromagnetic metal/insulator/ferromagnetic metal layers. Double-layered manganites are the materials owing such multi-layered stacks intrinsically. Considering

$La_{2-2x}Sr_{1+2x}Mn_2O_7$, every bilayer of MnO_2 is separated by an insulating (La, Sr)O barrier layer (Figure 6) [16]. The parental compound (x=0.0, $La_2SrMn_2O_7$, Mn^{3+} $3d^4$) is an insulator. Doping Sr up to ($0.3 \leq x \leq 0.45$), turns it into one of the most important and heavily studied colossal magnetoresistive materials.

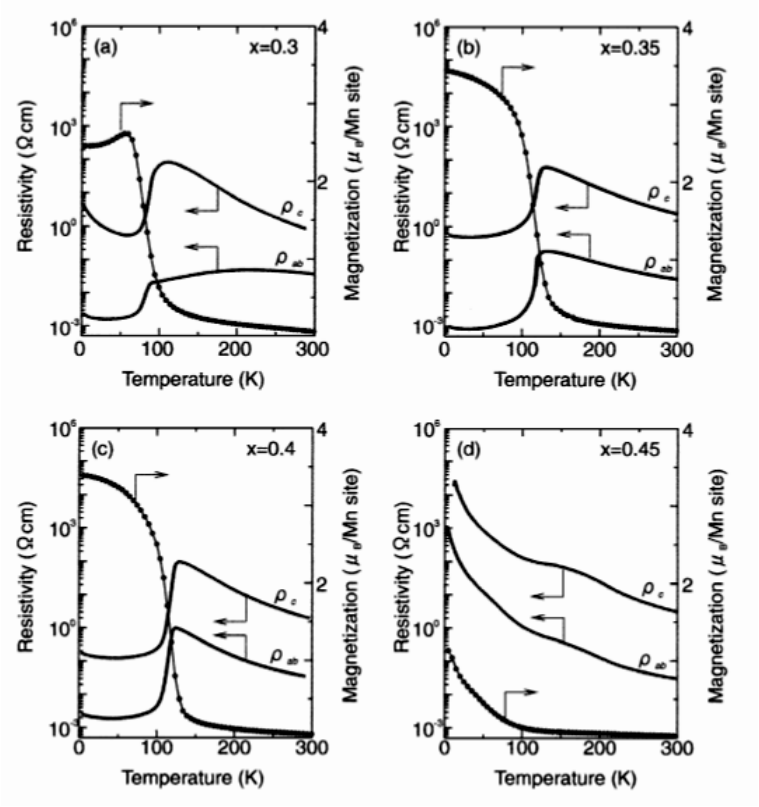

Figure 7: (left-hand side axis) Temperature dependence of in-plane (ρ_{ab}) and out-of-plane (ρ_c) resistivity; (right-hand side axis) Magnetization under applied magnetic field of 5 kOe parallel to in-plane direction for $La_{2-2x}Sr_{1+2x}Mn_2O_7$ ($0.3 \leq x \leq 0.45$) crystals [16].

Figure 7 compares magnetization curves (under applied magnetic field of 5 kOe) with in-plane (ρ_{ab}) and out-of-plane (ρ_c) resistivity curves as a function of temperature. The T_C of $La_{2-2x}Sr_{1+2x}Mn_2O_7$ ($0.3 \leq x \leq 0.4$) is around 100-130 K where the ferromagnetic order breaks eventually at the doping level of x=0.45. Due to the layered structure, the anisotropy in resistivity *i.e.* ρ_c/ρ_{ab} is about two orders of magnitude for the presented range of doping. A concomitant M-I transition occurs at the corresponding T_C at both crystal orientations. The metallic character at low temperatures almost disappears and the M-I transition becomes considerably weak at the doping level of x=0.45.

The out-of-plane resistivity of $La_{2-2x}Sr_{1+2x}Mn_2O_7$ (x=0.3, 0.4) compounds under different applied magnetic fields are shown in Figure 8. Upon increasing magnetic field up to 70 kOe, they show at the corresponding T_C, a negative magnetoresistance up to two orders of magnitude. The CMR effect occurs only for such narrow range of doping level ($0.3 \leq x \leq 0.4$), yet a rich magnetic phase diagram can be found within this range (Figure 9).

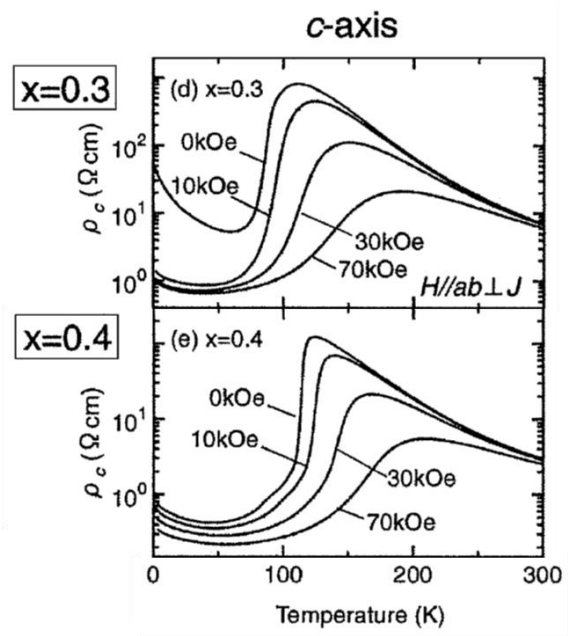

Figure 8: Temperature dependence out-of-plane (ρ_C) resistivity under several magnetic fields for the $La_{2-2x}Sr_{1+2x}Mn_2O_7$ (x=0.3, 0.4) crystals [16].

As it is shown, the spin configuration changes from out-of-plane to in-plane upon a slight change in doping level.

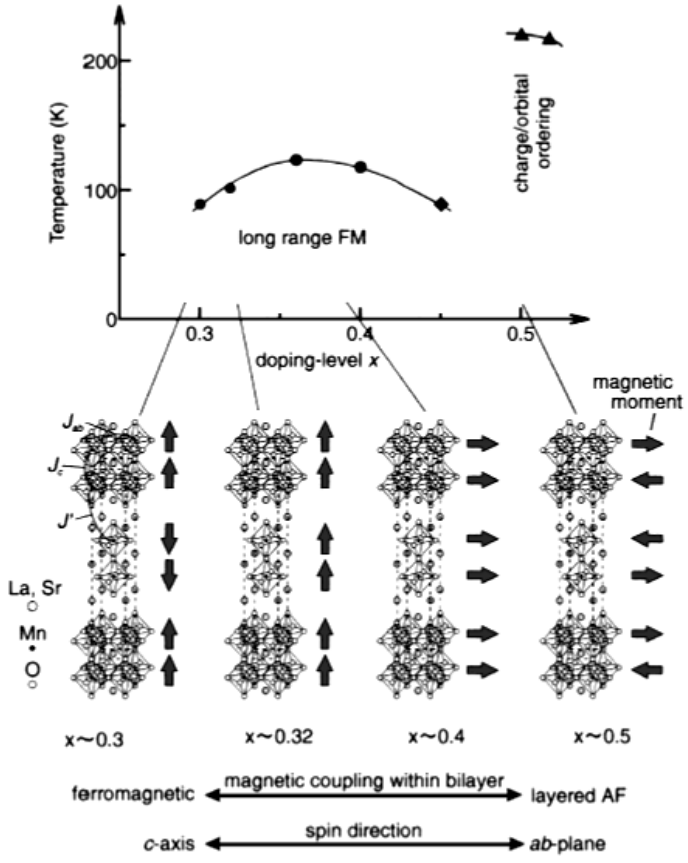

Figure 9: Ground state magnetic phase diagram of $La_{2-2x}Sr_{1+2x}Mn_2O_7$ ($0.3 \leq x \leq 0.5$) as a function of doping level [16].

At x=0.3, an antiferromagnetic order along the c axis occurs between each of MnO_2 bilayers. Increasing the doping level by only 0.02 transforms the spin order from antiferromagnetic to ferromagnetic. The ideal case for intrinsic magnetic tunnel junction device can be found at the doping level of x=0.4 where a ferromagnetic in-plane oriented spin order has been resolved by neutron diffraction [17].

Eventually, at doping level of x=0.5, the system shows two types of order, an A-type antiferromagnetic spin order and orbital order [18]. Exactly at the same doping level x=0.5, $La_{1-x}Sr_{1+x}MnO_4$ exhibits charge-orbital and spin order (see section 1.2.2). Thanks to the numerous investigations, there is a vast knowledge on the physics of double-layered manganites. For further discussions, Ref. [16-25] are highly recommended.

1.2.2. Single-layered Manganites: Crystal, Magnetic and Electronic Structures

The single-layered manganite (n=1), $La_{1-x}Sr_{1+x}MnO_4$ is an antiferromagnetic insulator where doping the compound with Sr does not change the macroscopic magnetic and transport ground states. The insulating behavior is believed to be due to isolation of MnO_6 octahedra based on the fact that the transport property is strongly anisotropic. In Figure 10a, the temperature dependence resistivity measurements reveal that the out-of-plane component is three orders of magnitude higher than the in-plane one at room temperature [26]. The magnetic behavior along in- and out-of-plane directions, however, does not show the drastic anisotropic picture (Figure 10b).

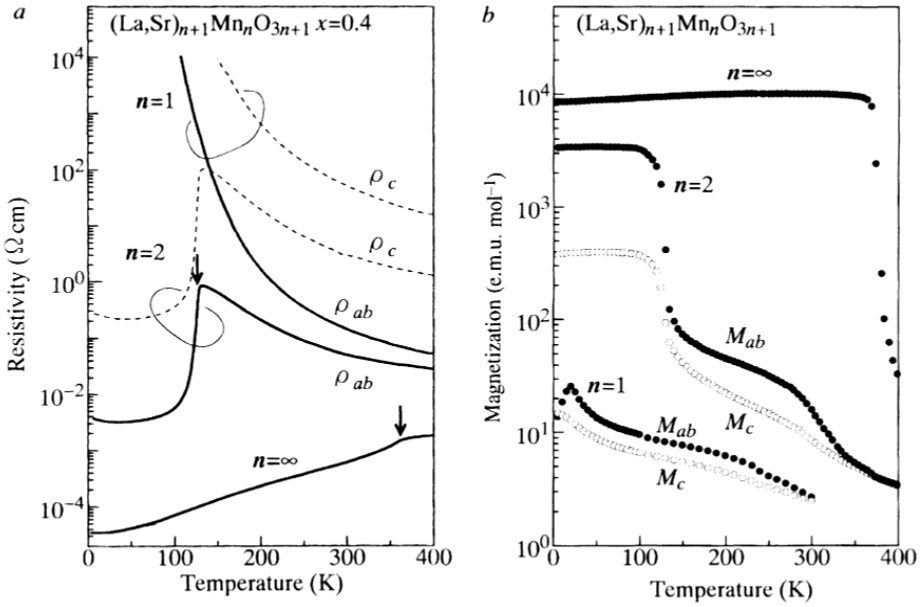

Figure 10: (a) Temperature dependence of resistivity and (b) magnetization for members of layered-perovskite manganites (n=1, 2 and ∞) with the hole-doping level of x=0.4. Solid and dashed lines (ρ_{ab} and ρ_c) represent in- and out-of-plane resistivity, respectively. Filled and open circles (M_{ab} and M_c) represent in- and out-of plane magnetization, respectively [26].

In the late eighties, Rao *et al.* reported a comparative study on magnetic and transport properties of few compounds with K_2NiF_4 structure including $La_{0.5}Sr_{1.5}MnO_4$, $LaSr_2Mn_2O_7$, $La_{1.5}Sr_{2.5}Mn_3O_{10}$, and also perovskite $La_{0.5}Sr_{0.5}MnO_3$. They demonstrated the dependence of resistivity on the type of network of MnO_6 octahedra. They showed as the number of isolated MnO_6 octahedra increases, the electrical transport enhances [27]. In other words, from an absolute 2D network (n=1) via a semi 3D network regime (n>3) to an absolute 3D network (n=∞), the electrical resistivity decreases drastically.

In 1995, Y. Moritomo *et al.* reported a dedicated study on the electrical resistivity and magnetic susceptibility of $La_{1-x}Sr_{1+x}MnO_4$ ($0.0 \leq x \leq 0.7$) single crystals [28]. In Figure 11, on the left hand side, the temperature dependent resistivity curves are shown. For $La_{1-x}Sr_{1+x}MnO_4$ (x=0.0), the resistivity curves demonstrate an insulating state within the measured temperature range, as it exceeds the measurement setup resolution at temperatures lower than 170 K. Doping Sr ($0.1 \leq x \leq 0.4$) decreases the resistivity remarkably where the room temperature values comparing to the parent compound (x=0.0) are three orders of magnitude eliminated. These four compounds, $0.1 \leq x \leq 0.4$, almost show a semiconductor-look resistivity curve. For doping levels ($x = 0.5$ and 0.6), a transition occurs at around 230 and 260 K. The transition can be seen for $La_{1-x}Sr_{1+x}MnO_4$ (x=0.5) in both in- and out-of-plane resistivity curves. In this report, Moritomo *et al.* addressed the transition as a charge-orbital[3] transition based on observation of sharp superlattice spots in the electron diffraction pattern below the transition temperature [28]. The temperature dependent magnetization curves (Figure 11, right hand side) show an evolution in magnetic order by increase in hole-doping level. The parent compound (x=0.0) shows an antiferromagnetic order with the Néel temperature of $T_N \sim 120$ K. The susceptibility measurements for in- and out-of-plane directions with applied magnetic field of 10 mT (Figure 11, inset of right hand side) for (x=0.0) show a characteristic antiferromagnetic order with the spins aligned along the c axis. Hole-doping affects the antiferromagnetic order and for the doping level of $0.2 \leq x \leq 0.6$, a Curie temperature between 60 and 110 K can be identified. Within this range of doping, a competition between ferromagnetic double-exchange interaction and antiferromagnetic super-exchange interaction causes the exhibition of spin-glass state.

[3] Charge and orbital orders are periodic orders of the charges and orbitals, respectively, which are not necessarily bound to the structural order. For the charge order, the localization of charges on the defined atomic sites prohibits the charge transport. For the manganites, a checkerboard pattern of Mn^{3+} and Mn^{4+} have been observed for the charge-ordered compounds. The orbital order, on the other hand, is a periodic alignment of a certain orbital, *e.g.* $d_{3z^2-r^2}$ or $d_{x^2-y^2}$ in certain crystal orientations.

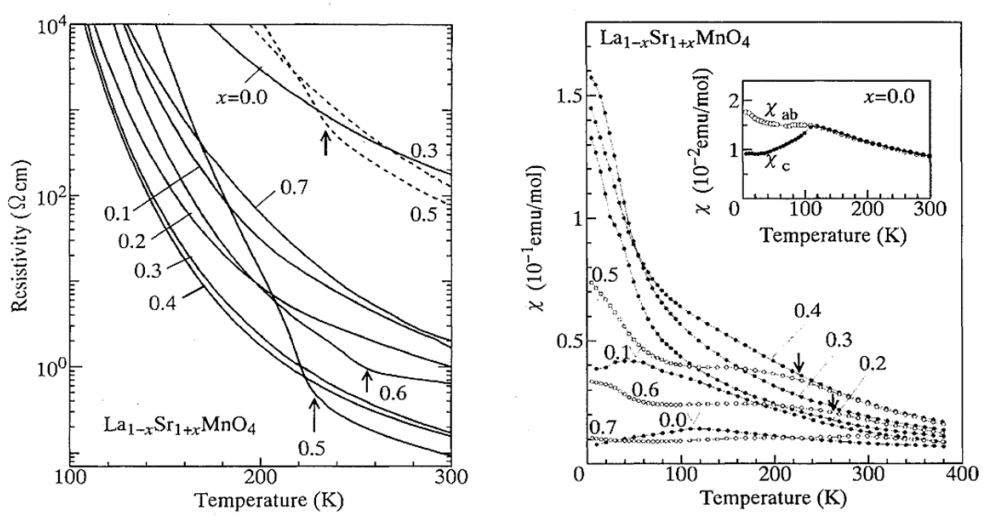

Figure 11: Temperature dependence (left) electrical resistivity, (right) magnetic susceptibility of $La_{1-x}Sr_{1+x}MnO_4$ ($0.0 \leq x \leq 0.7$) single crystals [28]; (left) Solid and broken curves stand for in- and out-of-plane components of resistivity, respectively; (right) Open and closed circles represent in-, and out-of-plane components of susceptibility, respectively. The susceptibility measurements were conducted in field cooled condition under the applied magnetic field of 1 T. The inset shows in- and out-of-plane susceptibility measurements field cooled under of applied magnetic field 10 mT.

Later in 1997, Moritomo *et al.* studied the suppression of charge-orbital transition in $La_{1-x}Sr_{1+x}MnO_4$ (x=0.5) by substitution of lanthanum with neodymium and samarium. In this way, the average ionic radius on the ***A***-site cation decreases and consequently a smaller in-plane Mn-O bond length will be expected (Figure 12).

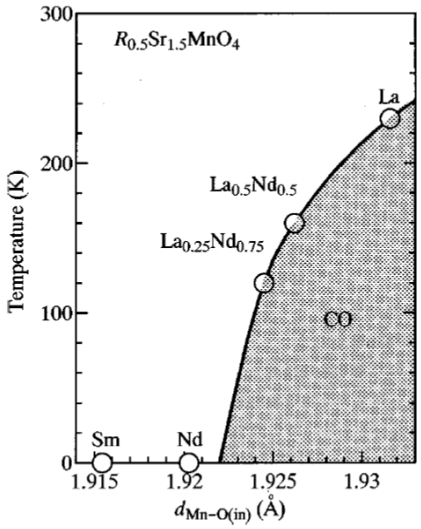

Figure 12: The charge-orbital ordering transition temperature versus the in-plane Mn-O bond length for $R_{0.5}Sr_{1.5}MnO_4$. The hatched area represents the charge-orbital order state [29].

Such in-plane architecture in MnO_6 octahedra encourages the out-of-plane Jahn-Teller distortion which itself affects the charge-orbital order state and decreases the transition temperatures as can be seen in Figure 12.

Eventually, when the Jahn-Teller distortion is big enough (for $Nd_{0.5}Sr_{1.5}MnO_4$ and $Sm_{0.5}Sr_{1.5}MnO_4$), the charge-orbital order state vanishes [29].

These two studies by Moritomo *et al.* [28, 29] suggest that for having and orbital ordered state in manganites, firstly the Mn^{3+}/Mn^{4+} ratio should be one and secondly, a structural-driven charge localization in the absence of Jahn-Teller distortion should occur.

Tokunaga *et al.* in 1999 reported the MR behavior of $La_{0.5}Sr_{1.5}MnO_4$ below charge-orbital order temperature down to 108 K using pulsed magnetic fields up to 40 T [30]. In Figure 13, it is shown that at low enough temperature of 108 K, a considerable negative magnetoresistance occurs and MR exceeds 10^4 with an applied magnetic field of 38 T.

Accordingly, they reported the emergence of a metamagnetic transition below the charge-orbital order temperature. They addressed the sudden change in resistivity to the field-induced collapse of charge ordering [30].

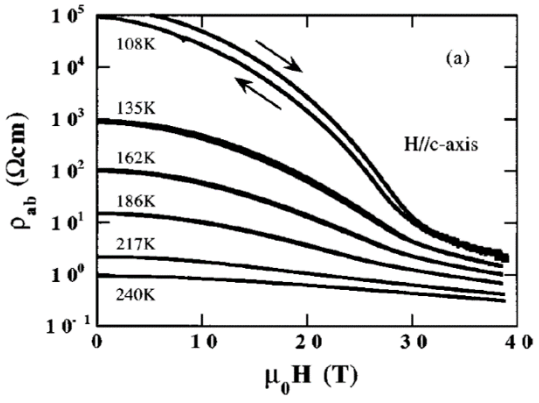

Figure 13: In-plane resistivity versus applied magnetic field along *c* axis of $La_{0.5}Sr_{1.5}MnO_4$ at different temperatures [30].

The Néel temperatures of $La_{1-x}Sr_{1+x}MnO_4$ (x=0.0, 0.25, 0.40 and 0.50) were measured by muon Spin Rotation (μSR) measurements reported by Baumann *et al.* in 2003 [31]. They reported a phase diagram of magnetic order transition temperature versus hole-doping concentration shown in Figure 14.

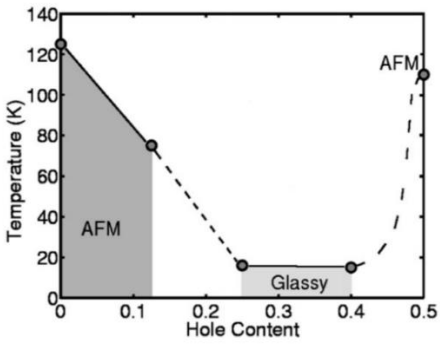

Figure 14: Phase diagram of magnetic order transition temperature of $La_{1-x}Sr_{1+x}MnO_4$ compounds versus hole doping concentration based on μSR measurements [31].

For the intermediate doping levels, a spin-glass state was suggested which agrees with the former reports (see for example Ref. [28]). The undoped and half-doped compounds show a long range antiferromagnetic order. However, as μSR suggests, the nature of these two states are completely different. Such difference in antiferromagnetic states is ascribed to the interplay of orbital and spin degrees of freedom. It is known that $LaSrMnO_4$ is a C-type antiferromagnet [32], while $La_{0.5}Sr_{1.5}MnO_4$ is a CE-type antiferromagnet (see section 1.4) [33]. The measurements of thermal expansion coefficient α along in- and out-of-plane axis for $La_{1-x}Sr_{1+x}MnO_4$ ($0.0 \leq x \leq 0.5$) single crystals were reported in 2005 by Klingeler *et al.* [34] and also Senff et al. [32] using a capacitance dilatometer. These results show anomalies in in- and out-of-plane α at Néel temperature of $La_{1-x}Sr_{1+x}MnO_4$ (x=0.0) (Figure 15). The anomalies coincide with decrease (increase) in a (c) lattice constant by decrease in temperature. Figure 15, clearly shows the occurrence of aforementioned anomalies for undoped and low-doped $La_{1-x}Sr_{1+x}MnO_4$ exactly at the Néel temperature which is determined by measurement of antiferromagnetic superstructure reflection (½, ½, 0) with neutron diffraction. On the other hand, for half-doped compound, no anomaly was observed suggesting an orbital order within the MnO_2 layers.

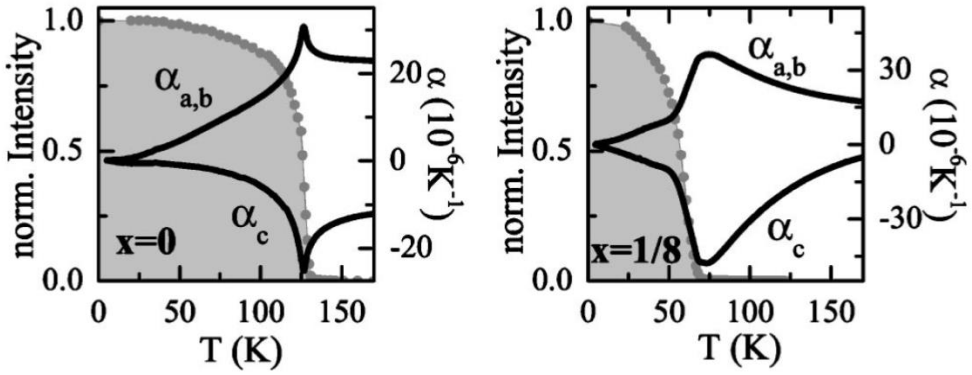

Figure 15: (right-hand side axis) In- and out-of-plane thermal expansion coefficient as a function of temperature for undoped and low-doped $La_{1-x}Sr_{1+x}MnO_4$ compounds (x=0.0, 0.125) measured by capacitance dilatometry; (left-hand side axis) Normalized intensity of antiferromagnetic superstructure reflection (½, ½, 0) measured by neutron diffraction [32].

Finally, it was shown that charge-orbital order state upon infrared photo-induction or neutron collision will be destructed [35-37].

1.3. Charge, Orbital and Spin Degrees of Freedom in Manganites

The charge-orbital order along with the spin order has been observed in multiple manganite systems. In this sense, simple perovskite manganites have been heavily studied. It is believed that the charge, orbital and spin degrees of freedom are correlated with the lattice of the crystal in which the average ionic radius and average oxidation state of the ***A***-site cations implies the

order states. For the perovskite manganites, the mean ionic radius of ***A***-site cations defines the level of distortion in perovskite crystal lattice. Moreover, the effective hopping of e_g electrons which is a function of Mn-O-Mn bond angle is dependent of the level of distortion. In fact, smaller average ionic radius of ***A***-site cations implies larger tilting of MnO_6 octahedra and hence, less effective hopping of e_g electrons or in another words, narrower effective one-electron bandwidth W of the e_g-band [38]. The pioneering work of Tokura *et al.* [39] on perovskite manganite systems with various rear earth and alkaline earth cations on the ***A***-site shows that the stability and strength of charge-orbital ordered phases are directly related to the crystal structure.

In Table I, the effect of combining different lanthanides (*i.e.* La, Pr, Nd, and Sm) with different alkaline earth metals (*i.e.* Ca and Sr) on the tolerance factor is shown. As the average ionic radius of the ***A***-site cations decreases, rhombohedral and orthorhombic structures are more stable than the cubic structure. As a result, the MnO_6 octahedra tilt, Mn-O-Mn bond angle deviates from 180° and therefore, the one-electron bandwidth W of e_g-electrons becomes narrow.

Table I: Average ionic radii of ***A***-site cations for some selected perovskite manganites. The ionic radii of La^{3+}, Pr^{3+}, Nd^{3+}, Sm^{3+}, Sr^{2+}, Ca^{2+}, Mn^{3+}, Mn^{4+}, and O^{2-} were used [40].

Compound	Average ***A***-site ionic radius	Tolerance factor
$La_{0.5}Sr_{0.5}MnO_3$	1.400	0.996193
$Pr_{0.5}Sr_{0.5}MnO_3$	1.365	0.983741
$Nd_{0.5}Sr_{0.5}MnO_3$	1.355	0.980183
$La_{0.5}Ca_{0.5}MnO_3$	1.340	0.974846
$Sm_{0.5}Sr_{0.5}MnO_3$	1.350	0.978404
$Pr_{0.5}Ca_{0.5}MnO_3$	1.315	0.965952
$Nd_{0.5}Ca_{0.5}MnO_3$	1.305	0.962394
$Sm_{0.5}Ca_{0.5}MnO_3$	1.290	0.957057

As it is shown in Figure 16, the compounds with tolerance factor ≥ 0.99 such as $La_{0.5}Sr_{0.5}MnO_3$ show a ferromagnetic order due to double-exchange interaction and a metallic state due to the hopping of e_g electrons. By decreasing the average ionic radius (*i.e.* narrowing W), the T_C of the corresponding compounds decreases and at enough low temperatures, a charge-orbital order state along with an antiferromagnetic spin order stabilize [23].

For $Pr_{0.5}Sr_{0.5}MnO_3$ and $Nd_{0.5}Sr_{0.5}MnO_3$ [41], a T_C at around 250 K follows by a T_{CO} at around 150 K. In charge-orbital order state, due to the localization of the e_g electrons, the

corresponding compounds show insulating state. By further narrowing the one-electron bandwidth from $Pr_{0.5}Ca_{0.5}MnO_3$ [42] and $Nd_{0.5}Ca_{0.5}MnO_3$ [43] to $Sm_{0.5}Ca_{0.5}MnO_3$ [44], the charge-orbital/antiferromagnetic orders govern further and therefore, the T_{CO} increases to around 250 K. The presented phase diagram clearly shows the correlation of distortion in MnO_6 octahedra with the magnetic and electronic order in perovskite manganites.

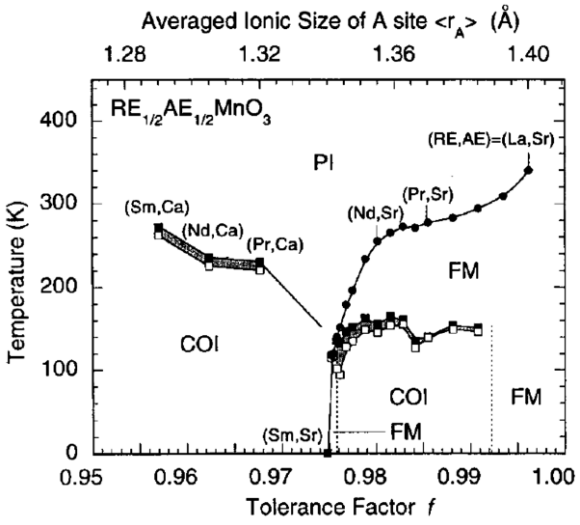

Figure 16: Curie temperature T_C (circles) and charge-orbital ordering temperature T_{CO} of various perovskite manganites as a function of average ionic radius of ***A***-site cations. The abbreviations FM, PI, and COI stand for ferromagnetic metal, paramagnetic insulator, and charge-orbital ordered insulator, respectively [23].

In general, by decreasing the average ionic radius, the double exchange ferromagnetic state becomes destabilized and competing super-exchange interaction on one hand side and Jahn-Teller electron-phonon coupling on the other side encourage an antiferromagnetic insulator state with the emergence of charge and orbital order. For detailed perspective on the charge-orbital transition in perovskite manganite, Ref [25, 45-48] are highly recommended.

1.4. Orbital Polarization in Manganites

The collective Jahn-Teller distortion in undoped parental manganite $LaMnO_3$ establishes an orbital ordered state with the transition temperature of T_O = 780 K much higher than the (A-type) antiferromagnetic order temperature at T_N = 140 K. The orbital order has been directly observed by resonance x-ray scattering showing a $d_{3z^2-r^2}$ orbital order along the *ab*-plane *i.e.* $d_{3x^2-r^2}$ and $d_{3y^2-r^2}$ orbitals[4] [49].

[4] In doubly degenerated *d* orbital, the e_g electron may occupy $d_{3z^2-r^2}$ and $d_{x^2-y^2}$ orbitals with a mixing angle, θ, where $|\theta\rangle = \cos\left(\frac{\theta}{2}\right)|3z^2-r^2\rangle + \sin\left(\frac{\theta}{2}\right)|x^2-y^2\rangle$.

The orbitals of Mn^{3+} $\left(t_{2g}^3 e_g^1\right)$ ions form the ordering pattern shown in Figure 17, where a ferromagnetic spin order in the *ab*-plane is compensated with the antiparallel spins in the next layer forming an A-type antiferromagnetic order. The orbital order repeats on each parallel *ab*-plane.

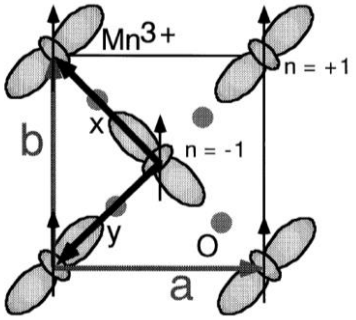

Figure 17: Schematic view of orbital and spin order in *ab*-plane of perovskite manganite, $LaMnO_3$ [49].

Hole-doping the $LaMnO_3$ with Sr up to (x=0.5) exhibits one of the richest phase diagrams showing a sequence of canted ferromagnetic-insulator, ferromagnetic-insulator and ferromagnetic-metal states [45, 50]. Through the insulator to metal transition, the orbital ordered state disappears as in ferromagnetic metal phase, the e_g are not prone to reside in a preferential orbital.

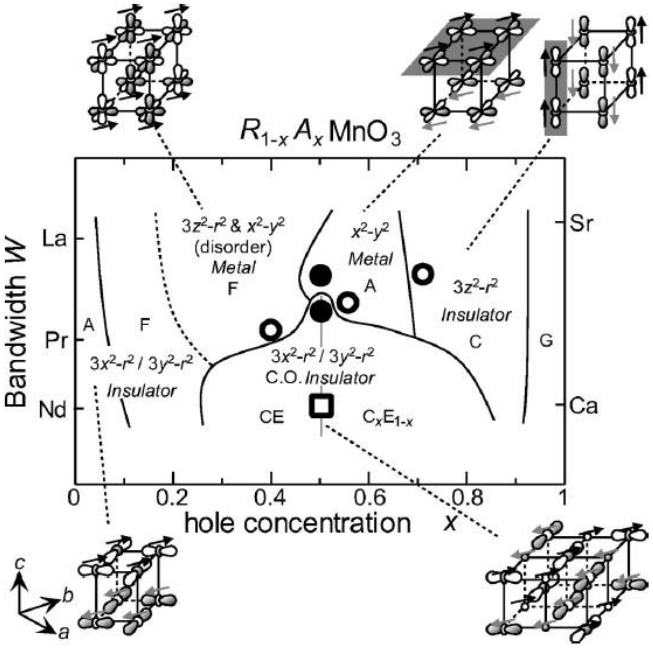

Figure 18: Spin, orbital and charge phase diagram as a function of doping level and one-electron bandwidth for perovskite manganites [51]. The abbreviations A, C, and G stand for A-, C-, and G-type antiferromagnetic spin order; F and CE for ferromagnetic and CE-type spin order and C.O. for charge-orbital order, respectively.

In Figure 18, the phase diagram of perovskite manganites as a function of doping level and one-electron bandwidth is shown. For $La_{1-x}Sr_xMnO_3$, further doping ($0.5 < x < 0.7$) stabilizes an

A-type antiferromagnetic metal state in which due to high concentration of Mn^{4+} ions, the e_g electrons gain enough energy to reside in $d_{x^2-y^2}$ orbital (Figure 18) and form a double-exchange mediated *ab*-plane ferromagnetic order [50, 52]. This A-type antiferromagnetic order is distinctively dissimilar to the one at low doping levels in terms of orbital polarization of Mn^{3+} ions. By using optical spectroscopy, at high doping levels for $Nd_{1-x}Sr_xMnO_3$ ($0.6 \leq x \leq 0.8$), a C-type antiferromagnetic insulating state was found where due to the lattice elongation in *c* direction, $d_{3z^2-r^2}$ orbital occupation is energetically favorable [51]. The sequence of A-AFM/FM/A-AFM/C-AFM shown in Figure 18 is also approved by mean-field theory calculations [53].

In the narrow bandwidth regime (bottom side on the diagram in Figure 18), the charge-orbital order state is stabilized. The spin order here is the CE-type antiferromagnetic depicted in Figure 19 showing a zigzag alignment of spins within the *ab*-plane in which the $d_{3x^2-r^2}$ and $d_{3y^2-r^2}$ orbitals of Mn^{3+} cations align diagonally with respect to the crystallographic axes.

Focusing on the half-doped manganites (*x*=0.5), the two extreme cases of wide and narrow one-electron bandwidth are interesting. For the wide *W* regime such as $La_{1-x}Sr_xMnO_3$ (*x*=0.5), there is no charge-orbital ordered state and only a ferromagnetic spin order. The manganites with narrow *W* like $Sm_{1-x}Ca_xMnO_3$ (*x*=0.5), however, show charge, orbital and spin orders.

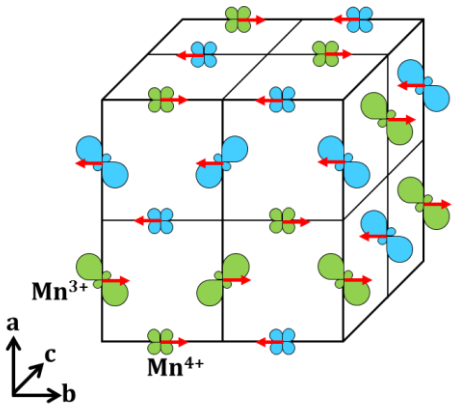

Figure 19: Schematic view of CE-type spin, checkerboard-pattern charge, and $d_{3x^2-r^2}/d_{3y^2-r^2}$ orbital order.

Based on the one-electron bandwidth, the perovskite manganites can be categorized as *type I* and *type II* [39]. For the *type I* manganites, with the relatively wide bandwidth such as $Nd_{1-x}Sr_xMnO_3$, the charge-orbital order occurs concomitantly with the CE-type antiferromagnetic spin order ($T_{CO} = T_N = 160$ K) [54]. For the relatively narrow bandwidth manganites like $Pr_{1-x}Ca_xMnO_3$ (*x*=0.5), first charge and orbital order appear simultaneously at $T_{CO} \cong 250$ K and then at lower temperatures, the CE-type antiferromagnetic spin order occurs [39].

The single-layered manganite $La_{1-x}Sr_{1+x}MnO_4$ (x=0.5) shows a *type II* evolution of orders with T_{CO} at around 220 K and T_N at around 110 K [33]. The origin of charge, orbital and spin order in $La_{1-x}Sr_{1+x}MnO_4$ (x=0.5) is different from narrow bandwidth perovskite manganites, since in former, isolated MnO_6 octahedra sandwiched between two (La, Sr)O layers form a 2D network of Mn-O-Mn bonds, whereas in latter, a considerable distortion in Mn-O-Mn bonds in 3D network of MnO_6 octahedra dictates charge localization and preferential orbital occupation. In this context, numerous investigations have been performed (see Ref. [33, 55-64]) shedding light on the complicated interplay of charge, orbital and spin degrees of freedom. In section 1.5, a detailed review on these investigations will be presented.

1.5. Direct Observation of Charge and Orbital Ordering

Neutron scattering measurements on $La_{1-x}Sr_{1+x}MnO_4$ (x=0.5) single crystals by Sternlieb *et al.* in 1996 revealed a charge-orbital ordered state below $T_{CO} \sim 217$ K with the charge ordered unit cell of $\sqrt{2}a \times \sqrt{2}a \times c$. Below the Néel temperature $T_N \sim 110$ K, a dimensionally similar magnetic unit cell of $\sqrt{2}a \times \sqrt{2}a \times c$ was reported [33]. These measurements at 9 K showed a crystal superstructure (see section 1.6) along $\mathbf{q}$ vectors of $\left(\frac{1}{2}, \frac{1}{2}, l\right)$ as well as magnetic scattering along $\mathbf{q} = \left(\frac{1}{4}, \frac{1}{4}, l\right)$ and $\mathbf{q} = \left(\frac{3}{4}, \frac{3}{4}, l\right)$ vectors resembling the aforementioned structural and magnetic unit cells (Figure 20).

In neutron scattering, the neutrons interact with atomic nuclei and magnetic dipoles of unpaired electrons. The intensity of the scattering conveys information about the electron distribution and spin orientation of a specific crystallographic position. Hence, neutron scattering is indifferent to the origin of electron distribution whether it comes from the oxidation state of the probed cation or the distortion in the crystal structure as an outcome of displacement of oxygen atoms around the subject cation. As a result, in the study reported by Sternlieb *et al.,* the direct observation of an alternating Mn^{3+}/Mn^{4+} pattern was not clear.

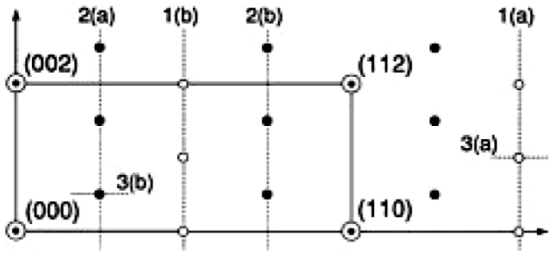

Figure 20: Schematic crystal, charge and spin unit cells of $La_{1-x}Sr_{1+x}MnO_4$ (x=0.5) at T = 9 K confirmed by neutron scattering measurements on $\mathbf{q} = (hhl)$ scattering plane where the nuclear (◉), magnetic (•) and additional superstructure (◦) peaks were observed [33].

In 1998, Murakami *et al.* reported a direct observation of charge and orbital ordering in $La_{1-x}Sr_{1+x}MnO_4$ (x=0.5) by Resonant X-ray Inelastic Scattering (RIXS) (originally in the paper, the method is called resonant x-ray diffraction) [55]. The resonant x-ray in RIXS allows us to choose the energy of incoming x-ray at the absorption edge of the probed element. Hence, RIXS is an element sensitive method. On the other hand, scattering in reciprocal space narrows the information embedded in the outcoming x-rays to the specific crystallographic positions. Furthermore, it is possible to use a linearly polarized x-ray (see section 5.1.1) to identify the orbital of the probed element. In summary, RIXS is a perfect tool to reveal the possible charge-orbital ordered states in correlated systems.

Back to the pioneering work by Murakami *et al.* [55], they set the energy of incoming x-ray to the K-edge of Mn and measured the superlattice peak at $\left(\frac{3}{2},\frac{3}{2},0\right)$ based on the suggested magnetic unit cell by Sternlieb *et al.* [33]. The energy of the absorption K-edge for Mn^{3+} and Mn^{4+} is slightly (~5 eV) different, thus the atomic scattering factor for these two valence states should be different. Based on these facts, the RIXS measurement at T = 29.6 K showed a charge separation and a preferential orbital occupation at Mn^{3+} and Mn^{4+} crystallographic positions. This result clearly disagrees with the possible charge disproportionation between Mn^{3+} and Mn^{4+} atomic sites. The proposed schematic charge, orbital and spin order in $La_{1-x}Sr_{1+x}MnO_4$ (x=0.5) below 110 K is shown in Figure 21.

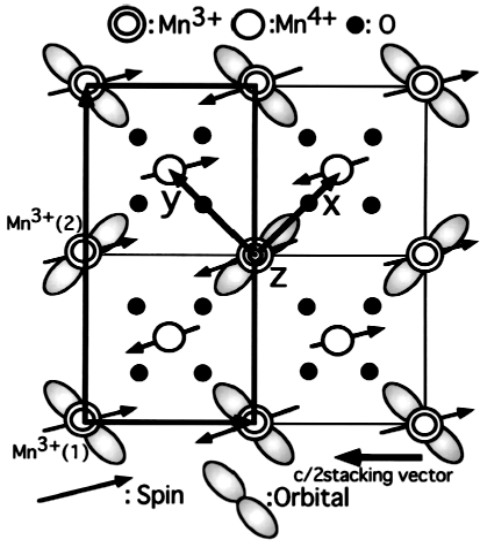

Figure 21: Schematic view of charge, orbital and spin order in $La_{1-x}Sr_{1+x}MnO_4$ (x=0.5) [55] based on RIXS and neutron scattering measurements.

In this study, the evolution of corresponding charge and orbital ordered reflections by temperature was shown. Their findings show that both charge order and orbital order occur simultaneously.

Ishikawa *et al.* in 1999 investigated the orbital anisotropy by measuring the optical birefringence on the single crystal sample of $La_{1-x}Sr_{1+x}MnO_4$ (x=0.5) [56]. This study, also confirmed the simultaneous occurrence of charge and orbital order. Furthermore, it was shown that the charge-orbital order becomes slightly suppressed below the Néel temperature suggesting the competence of charge-orbital order with spin order.

Since RIXS at the *K*-edge probes the ($1s \longrightarrow 4p$) transition, the question arises that how this edge can reveal the orbital ordering of the 3*d* cations like Mn. Murakami *et al.* [49, 55] addressed the absorption to the hybridization of 3*d*-4*p* bands. They stated that the *K*-edge reflects the anisotropy in 3*d* orbital indirectly from 3*d*-4*p* hybridization. Ishihara *et al.* used a nearest-neighbor model to explain the electron-electron interaction for the aforementioned hybridization approving the correctness of using *K*-edge for observation of orbital order [65]. In their calculation, they considered an atomistic "cluster model" in the perturbed condition of scattering measurement. However, others [66-68] did not agree with this model based on the broadness of 4*p* band and weak *d*-*p* Coulomb interaction. Instead, a band structure model revealed the dominate influence of Jahn-Teller distortion due to the oxygen atoms displacement *i.e.* Mn 4*p*-O 2*p* hybridization [66-68]. Therefore, in order to investigate the orbital order, it is rational to perform RIXS at *L*-edge of Mn which probes directly the electronic configuration of *d*-band (unlike the indirect nature of *K*-edge).

In 2003, Wilkins *et al.* performed x-ray scattering at *L*-edge of Mn and questioned the origin of orbital ordering whether it is a consequence of spin order below Néel temperature (magnetic origin) or a result of cooperative Jahn-Teller distortion below T_{CO} (structural origin) [69]. They reported a similar scenario for the charge-orbital order in agreement with previous reports. Compering the XAS scan at fixed vector $\mathbf{q} = \left(\frac{1}{4}, \frac{1}{4}, 0\right)$, the orbital order unit cell, with the simulated scan performed by Castleton & Altarelli [70], they ascribed the origin of orbital order to cooperative Jahn-Teller distortion below T_{CO} [69]. A similar study by Dhessi *et al.*, however, accounted an accompanying Jahn-Teller distortion with spin correlation as the origin for orbital order in $La_{1-x}Sr_{1+x}MnO_4$ (x=0.5) below T_{CO} [71]. Both energy scan measurements at fixed orbital order reflection are shown in Figure 22. Both spectra share more or less similar features at both L_2- and L_3-edges. The difference in these two studies which ascribes the origin of orbital order to different origins is the method to simulate the measured spectra.

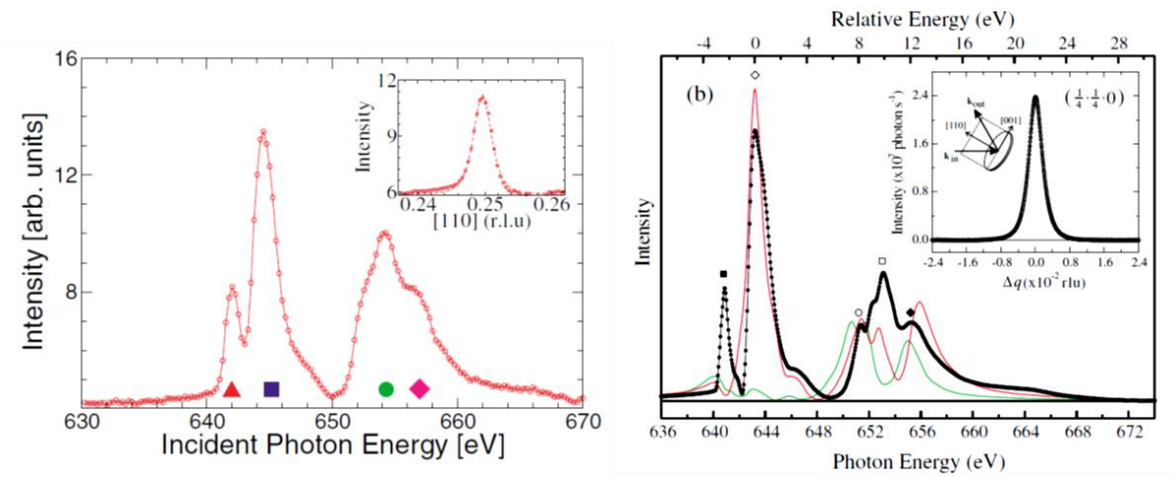

Figure 22: (left) Energy scan at fixed wave vector $\mathbf{q} = \left(\frac{1}{4}, \frac{1}{4}, 0\right)$, the orbital order reflection, at 140 K of $La_{1-x}Sr_{1+x}MnO_4$ (x=0.5). The main features are marked with colored signs [69]; (right) same energy scan at the same wave vector at 134 K. (left) The calculated spectra in D_2h symmetry for large (red line) and small (green line) Jahn-Teller distortion are shown [71].

The anisotropy of orbitals can be studied accurately by using linearly polarized x-ray to probe the absorption edge of the target element. By this method, the number of electrons in the valence shell of the element can be identified either directly (X-ray Emission Spectroscopy) or indirectly (X-ray Absorption Spectroscopy). Since this method is what is used in the current work, it will be described separately in section 5.1, to clarify the orbital occupation of Mn in thin film samples of $La_{1-x}Sr_{1+x}MnO_4$ (x=0.0, 0.5).

1.6. Electronic and Magnetic phase diagram of Single-layered Manganite: Commensurate *vs.* Incommensurate superstructure

The structural homologue of $La_{1-x}Sr_{1+x}MnO_4$ are the cuprate $La_{2-x}Sr_xCuO_4$ and the nickelate $La_{2-x}Sr_xNiO_4$. The parent nickelate (x=0.0) is an antiferromagnetic insulator similar to $La_{1-x}Sr_{1+x}MnO_4$ (x=0.0). By doping Sr up to ($x \approx 1$), it becomes metallic [72]. Neutron scattering on insulating $La_{2-x}Sr_xNiO_{4+y}$ (x=0.2) shows the presence of superlattice reflections around the (π, π) point which were ascribed to the two-dimensional (2D) incommensurate[5] magnetic fluctuations in the NiO_2 planes. In particular, four diffuse incommensurate peaks located at $\left(1 \pm \delta, 0, \frac{1}{2}\right)$ and $\left(1, \pm\delta, \frac{1}{2}\right)$ in reciprocal space were seen [72]. In Figure 23, the spatial correlation of spins and holes (charges) in a NiO_2 plane is illustrated. The arrangement of antiferromagnetic stripes in this compound is intriguing. In this compound, spin and hole order concomitantly occur at 100 K [73].

Figure 23: A schematic view of NiO_2 plane in $La_{2-x}Sr_xNiO_4$ (x=0.25) showing antiferromagnetic "stripes". In this figure only the Ni atoms are drawn and oxygen atoms are omitted for simplicity [74]. The white circles with spin orientation represent the Ni atoms while the black circles resemble the holes.

[5] In diffraction/scattering, appearance of a set of weak spots between the stronger spots is addressed to reflections of a superstructure. The superstructure reflections, in fact, represent a modulation of a substructure. If the superstructure reflections locate at a simple fraction of reciprocal lattice's vector e.g. (½ 0 0), the modulation is called commensurate superstructure. If the superstructure reflection do not fall into a simple fraction of reciprocal space vector, e.g. (0.5241 0 0), the modulation is called incommensurate superstructure. Occurrence of such superstructures can be considered as partial movement of the atoms in crystal unit that is slightly different than the crystallographic positions. Accordingly, the new structure can be regarded as a distorted one. Such concept is also true by looking at the interface between a thin film and the substrate. If the film is epitaxial, the interface in commensurate and if not, incommensurate. Furthermore, if the order parameter is the magnetic order of the system, then through a phase transition, the new magnetic structure may not follow the crystal order, thus be incommensurate. A spatially modulated magnetic superstructure is a case of magnetic frustration. Successful ANNNI model (axial next-nearest-neighbor Ising model) has been widely used to explain the effect of commensurability on the magnetic structure.

Such stripe-like phase separation with an array of holes in the domain walls between antiferromagnetic patches of magnetic atoms has been observed for the analogous single-layered cuprate materials as well. Incommensurate magnetic reflections were observed for $La_{2-x}Sr_xCuO_4$ using inelastic neutron scattering indicating the presence of similar spin and charge ordered structure [75]. The spin-stripe order in $La_{2-x}Sr_xCuO_4$ ($0.05 < x < 0.13$) is present but weak. Within this region, the material shows a superconductive state. Despite the fact that the spin and charge incommensurate orders vanish above $x > 0.13$, the superconducting state remains up to doping levels of $x < 0.25$ [76]. The best case study of stripe ordered cuprate is perhaps $La_{2-x}Ba_xCuO_4$ (x=1/8) showing a two dimensional superconducting fluctuation and unambiguously resembles the spin and charge order structure [77]. For single-layered nickelates and cuprates, the electronic configuration is Ni^{2+} $d^8\left(t_{2g}^6 e_g^2\right)$, Ni^{3+} $d^7\left(t_{2g}^6 e_g^1\right)$ and Cu^{2+} $d^9\left(t_{2g}^6 e_g^3\right)$, Cu^{3+} $d^8\left(t_{2g}^6 e_g^2\right)$, respectively, in which the t_{2g} state is full and the e_g electrons reside in either $d_{3z^2-r^2}$ or $d_{x^2-y^2}$ orbitals.

As it is discussed in section 1.1, for manganese cations in doped $La_{1-x}Sr_{1+x}MnO_4$, Mn^{3+} d^4 $\left(t_{2g}^3 e_g^1\right)$, Mn^{4+} d^3 $\left(t_{2g}^3 e_g^0\right)$, the $3d$ electrons occupy both t_{2g} and e_g states adding additional order "orbital order" along with the charge and spin order. In fact the incommensurate superstructure has been reported for low hole-doping regime of single-layered manganite as well, similar to the analogous nickelates and cuprates.

Larochelle *et al.* performed a marathon of x-ray and neutron scattering on 18 doping levels of $La_{1-x}Sr_{1+x}MnO_4$ in the range of ($0.0 \leq x < 0.7$) to reveal the crystal and magnetic structures [35, 78]. For x=0.0, they reported a G-type antiferromagnetic order (disagrees with generally approved C-type order) with the Néel temperature of T_N = 128.4 K. Upon doping up to x=0.1, the spin order does not change, however, the Néel temperature decreases to T_N = 61.0 K.

By analyzing the neutron scattering data, they reported a transition from long-range to a short-range spin order by considering the magnetic correlation length of parallel spins. It has been found that by doping up to x=0.1, the magnetic correlation length decreases and for the compounds with x=0.125 and 0.15, the long-range order becomes destructed. This is where the magnetization measurements [28] and μSR [31] show a spin-glass state in which the magnitude of ferromagnetic coupling (J_F) becomes comparable to antiferromagnetic coupling (J_{AF}). Moreover, TEM and electron diffraction revealed a tetragonal structure for doping levels below x=0.1, while in the region of ($0.1 \leq x \leq 0.2$), the room temperature tetragonal structure transforms to an orthorhombic one at lower temperatures. Within the orthorhombic structure, the Mn^{3+} orbitals are either in $d_{3x^2-r^2}$ or in $d_{3y^2-r^2}$ configuration [79]. This is the state of

orbital order without charge order where the so called ferrodistortive[6] patches (Figure 24) form. Formation of the ferrodistortive patches is a response of the material to the orthorhombic distortion [79].

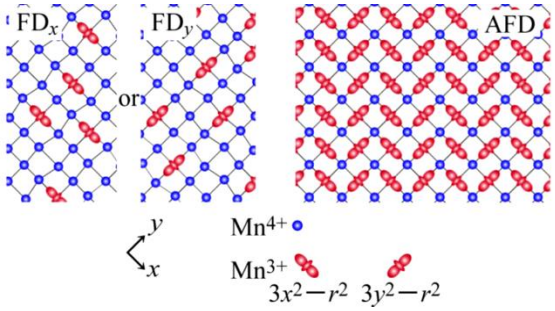

Figure 24: A representation of ferrodistortive (FD) and antiferrodistortive (AFD) states [79]. The (anti)ferrodistortive state is defined based on (anti)ferro-alignment of $d_{3x^2-r^2}$ or $d_{3y^2-r^2}$ orbitals of Mn^{3+} cations.

In the intermediate doping region of $(0.15 < x < 0.45)$, the magnetic correlation length is very small indicating a short-range-ordered structure. Furthermore, the superstructure peaks along with the charge-orbital order reflections were identified. This is in accordance with the TEM results in which at doping region of $(0.2 < x < 0.5)$, an incommensurate charge-orbital state with a tetragonal structure was observed [79].

For x=0.5 compound, the crystal structure below T_{CO} undergoes a structure transition from tetragonal to orthorhombic in agreement with electron diffraction [28] and Raman scattering [36] (disagrees with TEM investigations by Norimatsu *et al.* [79]). As the temperature decreases, orthorhombicity develops until the reported T_N and then stays constant.

In accordance to the charge-orbital order state, a commensurate superlattice vector modulation is observed for doping level of x=0.5 (revealing a CE-type spin order). This modulation vector stays unchanged for doping levels of $(0.45 \leq x \leq 0.50)$. The explanation of same charge order state for lower hand-side of commensurate structure was given as separation of material into a charge-orbital ordered regions and disordered regions where the disordering strength is not sufficient enough to transform the structure into an incommensurate state. A Néel order state for this range of doping level with a change in order parameter at T_N = 115 K has been observed [35]. Another study by Arao *et al.* using TEM shows CE-type spin order along with charge-orbital order state for $La_{1-x}Sr_{1+x}MnO_4$ in doping levels of

[6] At low doping level regime, the e_g electrons of Mn^{3+} cations resides either in $d_{3x^2-r^2}$ or $d_{3y^2-r^2}$ orbitals. Upon doping up to x < 0.5, a competition between ferrodistortive and antiferrodistortive states occurs (due to the interaction between the neighboring Jahn-Teller distorted clusters [**80**] K. H. Ahn, T. Lookman, and A. R. Bishop "Strain-induced metal-insulator phase coexistence in perovskite manganites" Nature **428**, 401 (2004). Finally at x=0.5, the structure stabilizes the antiferrodistortive states where charge and orbital order concomitantly form.

$(0.49 \leq x \leq 0.53)$ based on observation of both transverse and longitudinal modulation below the Néel temperature [81].

For the over-doped region *i.e.* $x < 0.5$, the long-range-order disappears and incommensurability develops upon increasing the doping level. However, due to lower crystal quality of these samples, the observed modulations could also be ascribed to non-stoichiometric oxygen content. In another neutron diffraction study by Ulbrich *et al.* on $La_{1-x}Sr_{1+x}MnO_4$ (x=0.58), it revealed that Mn^{3+} cations are in an incommensurate state, while a commensurate pattern for Mn^{4+} cation is established [82].

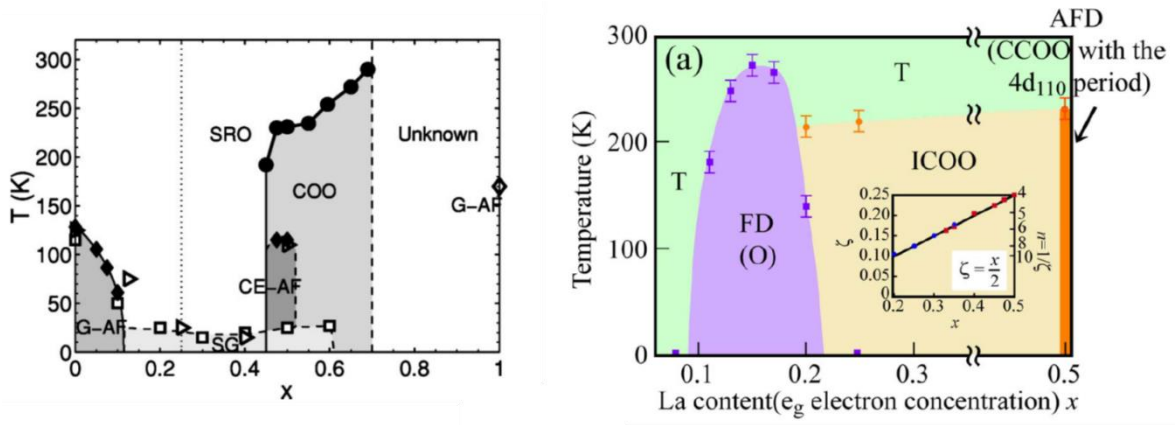

Figure 25: Magnetic and structural phase diagram of $La_{1-x}Sr_{1+x}MnO_4$ as a function of doping level and temperature (left) based on x-ray and neutron scattering [35] and (right) based on transmission electron microscopy [79]. G-AF, CE-AF, COO, SG and SRO on the left diagram represent G-type antiferromagnet, CE-type antiferromagnet, charge-orbital order, spin-glass and short-range-order, respectively. T, O, FD, AFD, ICOO and CCOO on the right diagram represent tetragonal, orthorhombic, ferrodistortive, antiferrodistortive, incommensurate charge-orbital order and commensurate charge-orbital order, respectively.

To summarize, in Figure 25 the two phase diagrams of $La_{1-x}Sr_{1+x}MnO_4$ as a function of hole-doping level based on x-ray and neutron scattering [35] and transmission electron microscopy [79] are shown. In terms of magnetic order, a G(C)-type antiferromagnet ($T_N \sim 125$) transforms to a spin-glass state and eventually at the half-doping level, again a long-range-order state with CE-type antiferromagnet configuration ($T_N \sim 110$) becomes established. Upon further slight doping, the long-range-order disappears.

A recent study based on high-resolution XRD and RIXS at *K*-edge of Mn by Herrero-Martín *et al.* suggests a tetragonal to orthorhombic phase transition for $La_{1-x}Sr_{1+x}MnO_4$ (x=0.5) where displacement of oxygen atoms evolves a distinctive checkerboard pattern for Mn^{3+} and Mn^{4+} sites. However, the chemical shift of these two inequivalent Mn sites is too small to ascribe them to Mn^{3+} and Mn^{4+}. Instead, Herrero-Martín *et al.* proposed a charge disproportionation model with charge difference of 0.15 electrons between the two inequivalent sites [83, 84]. A similar charge disproportionation state for over-doped manganite $La_{1-x}Sr_{1+x}MnO_4$ (x=0.6) has been proposed by García *et al.* based on RIXS measurements at Mn *K*-edge [85].

1.7. Preferential orbital occupation in manganite thin films induced by strain

It has been shown that induced strain in thin films of perovskite manganite affects the electrical and magnetic properties. For example, compressive strain on $La_{1-x}Ca_xMnO_3$ (x=1/3) turns the metallic bulk material (M-I transition at around 250 K) to an insulator and decreases the total magnetic moment to half of its bulk value [86]. The tensile strain also affects the properties and evolves anisotropic electric transport properties [87]. Below the relaxation thickness[7], the M-I transition *i.e.* orbital order transition temperature shifts to lower values which has been ascribed to the change in orbital occupancy of e_g electrons of Mn cations [86-88].

Konishi *et al.* in 1999 reported a pioneering work on growth of 40 nm fully strained thin films of $La_{1-x}Sr_xMnO_3$ (x=0.3, 0.4 and 0.5) on $SrTiO_3$ (STO, a=3.905Å), $(LaAlO_3)_{0.3}$-$(SrAl_{0.5}Ta_{0.5}O_3)_{0.7}$ (LSAT, a=3.870Å), and $LaAlO_3$ (LAO, a=3.792Å) single crystal substrates [89]. They showed by applying different states of strain using different substrates, it is possible to change the c/a ratio of the film from 1.06 to 0.98 which is equivalent to application of +11 to -5 GPa uniaxial pressure, respectively. More importantly, they should a strong correlation between magnetic/electronic structures and distorted crystal lattice. In bottom panel of Figure 26 (a), the temperature dependence resistivity curves of $Nd_{1-x}Sr_xMnO_3$ single crystals with doping levels of ($0.45 < x < 0.67$) are shown. A slight increase in doping level changes the spin order from ferromagnetic to A-type antiferromagnetic and finally to C-type antiferromagnetic. The spin order structure is shown schematically in the upper panel of Figure 26 revealed by neutron scattering measurements [41]. Konishi *et al.* showed a similar evolution of temperature dependence resistivity curves for $La_{1-x}Sr_xMnO_3$ not by altering the doping level, but with application of strain. Here, $La_{1-x}Sr_xMnO_3$ (x=0.5) films on STO, LSAT and LAO have c/a ratio of 0.97, 0.99 and 1.04, respectively (bottom panel, Figure 26b). The temperature dependence resistivity curves (not shown here, Figure 2 of Ref. [89]) are quite similar to what have been observed for $Nd_{1-x}Sr_xMnO_3$ single crystals with similar c/a ratios. The intriguing result is that the $La_{1-x}Sr_xMnO_3$ films with roughly similar c/a ratio to $Nd_{1-x}Sr_xMnO_3$ single crystals show similar resistivity curves which made the authors able to ascribe the spin order of these film to the ones had been obtained by neutron diffraction on $Nd_{1-x}Sr_xMnO_3$ single crystals.

Accordingly, when lattice constants of the films fall into the regions showed in Figure 26b, with respect to c/a ratio and doping level, the spin order upon a change in preferential orbital occupation would be defined as either A- or C-type antiferromagnet or ferromagnet suggesting

[7] There are two thresholds for film thickness namely relaxation and critical thicknesses. On the thick side, the relaxation of film will reflect the bulk properties of the grown material, here we call it relaxation thickness. On the very thin side *i.e.* the critical thickness, a few unit cells, a solid solution of sub-compounds yield to anomalous properties.

a strong correlation between spin and lattice structures. The aforementioned phase diagram was confirmed by theoretical calculation with slight shift in phase boundaries [90].

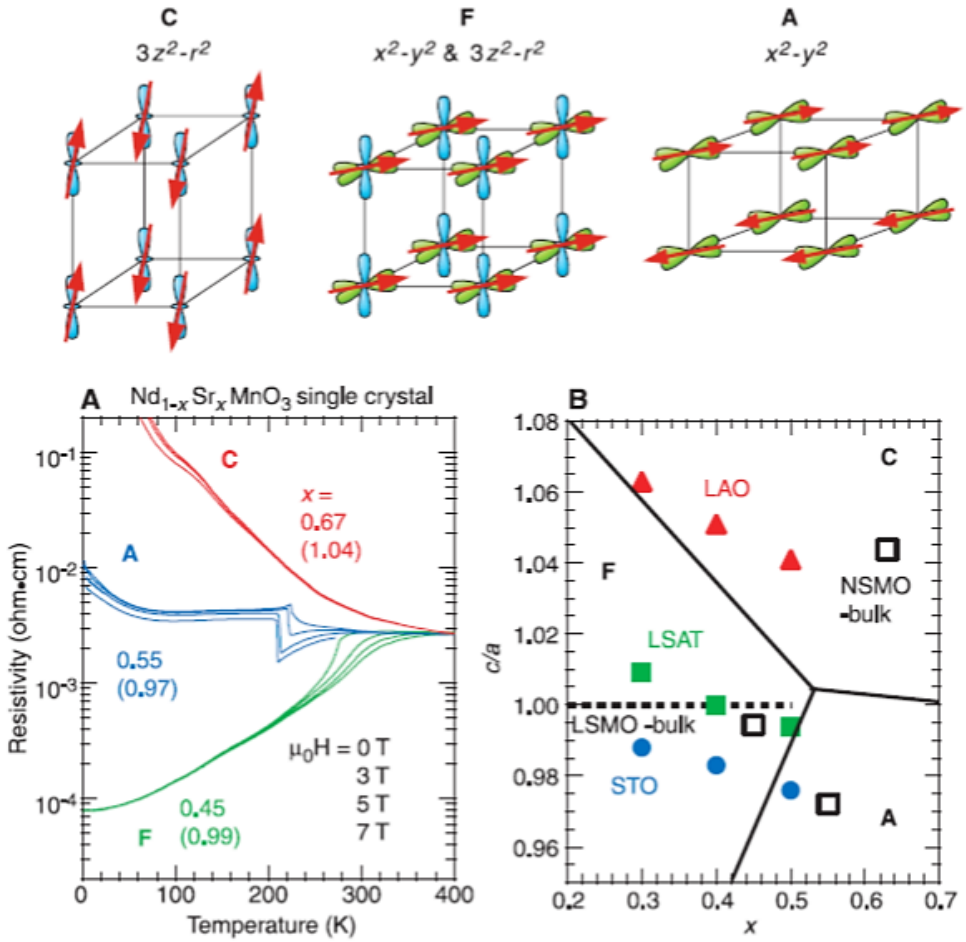

Figure 26: (Top panel) schematic representation of C-type (C) and A-type (A) antiferromagnetic and ferromagnet (F) spin order. (Bottom panel, a) Temperature dependence resistivity curves under different applied magnetic fields for single crystal of $Nd_{1-x}Sr_xMnO_3$ with various doping levels (x=0.45, 0.55 and 0.67) showing distinctive spin orders revealed by neutron scattering. The numbers in parentheses below the doping levels resemble the c/a ratio of corresponding single crystals. (Bottom panel, b) Phase diagram of $La_{1-x}Sr_xMnO_3$ thin films grown on STO, LSAT and LAO substrates as a function of doping level and c/a ratio. LSMO-bulk and NSMO-bulk stand for single crystals of $La_{1-x}Sr_xMnO_3$ and $Nd_{1-x}Sr_xMnO_3$, respectively [39, 89].

The alteration of spin order from A-type to C-type (Figure 26, top panel) as a response to increase in c/a ratio could be the basis of future orbitronics devices (analogous to spintronics). In such devices, the electric and magnetic properties could be engineered through the change in preferential orbital occupation. For instance in $La_{1-x}Sr_xMnO_3$ (x=0.5) films, the in-plane character of electrical transport can be switch to an out-of-plane one by shifting from a tensile strain with a compressive one. This can be achieved for instance by having a piezoelectric substrate where the strain is stimulated by applying electric potential.

2. Fabrication of Thin Films Using Pulsed Laser Deposition

This chapter presents general aspects of pulsed laser deposition (PLD), the technical capabilities of the costume designed PLD system which has been used for the presented study, and the experimental details and deposition conditions of thin film growth.

2.1. Pulse Laser Deposition

This section is a collective summary of diverse chapters of Ref [91, 92].

Pulsed laser deposition (PLD) technique has been used widely for producing high quality, single crystalline thin films and heterostructures. Despite the relative simplicity of the process, a stoichiometric transfer of the target material to the substrate which is located several centimeters away can be achieved. An accurate control over entities like temperature, pressure and kinetics of the process makes PLD a powerful technique for engineering the materials. Moreover, PLD is a suitable and capable technique to fabricate heterostructures involving multiple layers. Thin film deposition in PLD is a three-step process consisting of ablation of target material, plume propagation and thin film deposition.

- Ablation of target material

  By bombarding a condensed phase with ions, electrons or photons, an emission of particles forms. This phenomenon is known as ablation. In PLD, pulsed photons, *i.e.* laser pulses (often from an excimer laser[8]) interact with the condensed phase. The interactions are categorized into thermal and non-thermal regimes. In thermal regime, the laser energy per area (J/cm^2), known as laser fluence, is less than the binding energies of the atoms of the target material. Therefore, the absorbed laser energy leads to vaporization of the target material. If the pulse duration is longer than vaporization process, a thermodynamical equilibrium between solid and vapor phases establishes. Otherwise, the vaporization process will be non-equilibrium [92]. The laser fluence which divides the thermal and non-thermal regimes is called ablation threshold. In non-thermal regime, where the laser fluence is greater than the binding energy of the target material, *i.e.* greater than ablation threshold, the interaction results in emission of the material [91]. Normally, laser pulses produce defects on the surface of the target. These defects act as a driving force for energetic expulsion of the atoms. If the laser energy is high enough, instead of atom expulsion, an ejection of electrons will occur

[8] The excimer laser, a short term of excited dimer laser, is an ultraviolet laser which has been used vastly in PLD process. The excimer laser is a pulsed laser where each pulse is an outcome of reaction of a noble gas and a halogen. Depending on the gases, the wavelength of laser is defined.

(ionization process) which itself produces a strong electric field and consequently pulls ions out of the target.

- Plume propagation

  The ejected atoms and/or ions form a plume. The plume is a plasma-state containing free electrons, ions, atoms or even molecules depending on laser fluence, pulse duration and spot size of the laser beam. The full ionization process of the ablated species continues in the vicinity of the surface of the target. If the density of the ablated species in the plume is low, the species-species interactions will be negligible and the propagation regime will be free flight [91]. On the other hand, in a high density plume, the collision of ablated particles form a thermally homogenous cloud. The thickness of the cloud is about 50 μm and is known as Knudsen layer. For the sake of lowering the total energy level of unstable plasma state, the plume expands and the species with supersonic speed eject towards the single crystal substrate placed on top of the plume (Figure 27).

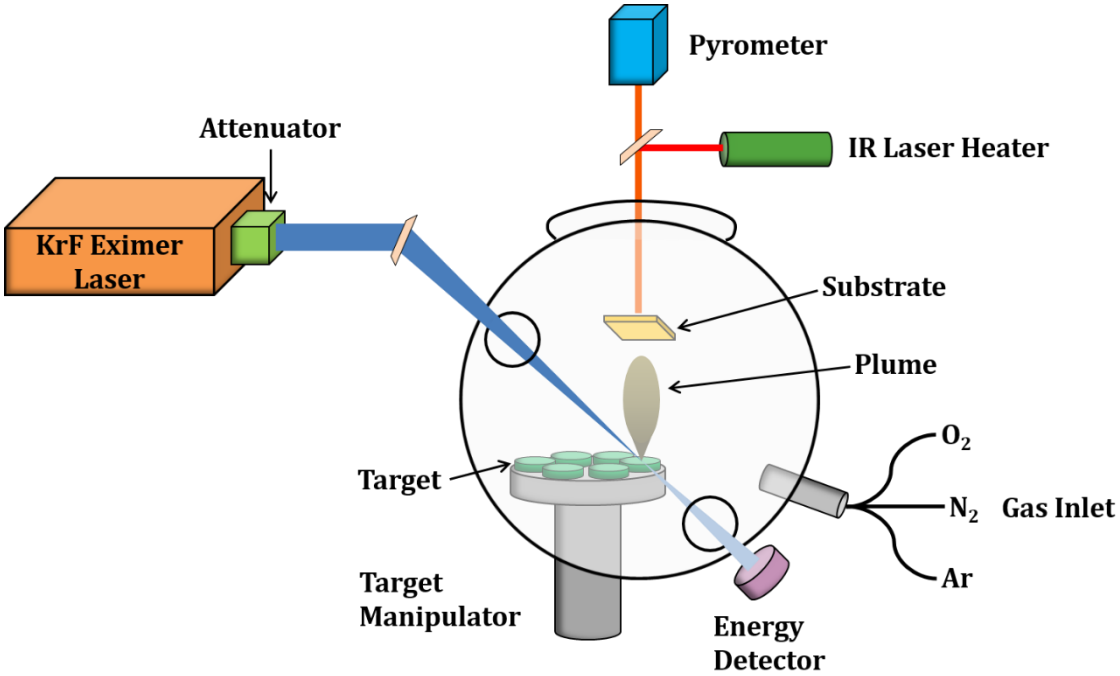

Figure 27: Scheme of pulsed laser deposition system.

In PLD, process gases such as argon, oxygen or nitrogen are used accomplishing two goals. First, it moderates the speed of highly energetic ablated species. Therefore, the number of collision events between the ablated species and the substrate will be minimized, so will be the formation of defects on the substrate. Second, the process gas acts as a reactant. The pressure and the flow rate of the process gas affect the composition and crystal structure of the thin film, remarkably.

The target-substrate distance has an important role in controlling the kinetic of the process. As a general rule, the distance should be chosen in a way that the tip of the plume does not touch the substrate. If the substrate is placed in the plume, due to inhomogeneous distribution of the ablated species, a chemically non-uniform film will be grown.

- Film deposition

  As the final step, the ablated species reach the surface of the substrate where the film condensation occurs. In order to grow high quality crystalline thin films, the temperature of the substrate should be high enough (more than 400 °C) to provide enough energy for movement of the incoming species to the substrate. The film condensation is classified into different categories which is the scope of the next section.

2.1.1. Condensation and Growth

The degree of substrate surface wetting with the incoming ablated species can be formulated using Young equation:

$$\Gamma_S = \Gamma_I + \Gamma_F \cos\theta \qquad (4)$$

where Γ_S, Γ_F, *and* Γ_I are free surface energies of the substrate, the film and the interface between them, respectively. A schematic view of substrate surface wetting with a particle is demonstrated in Figure 28 where θ is the contact angle.

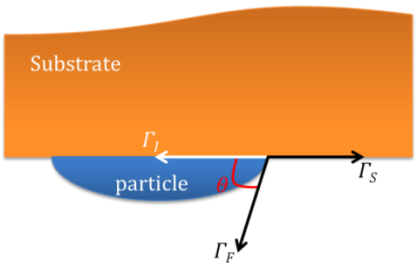

Figure 28: A schematic presentation of wetting the surface of the substrate by incoming ablated particle.

Since the particles could be considered as spheres, thus the equation (4) reduces to $\Gamma_S = \Gamma_I + \Gamma_F$. If the total surface energy $(\Gamma_I + \Gamma_F)$ is lower than the surface energy of the substrate (Γ_S), growth will be in layer-by-layer mode known as Frank-van der Merwe mode. On the other hand, if the surface energy of the substrate is lower than the total surface energy, the wetting will be limited and as a result, the island growth occurs (Volmer-Weber mode).

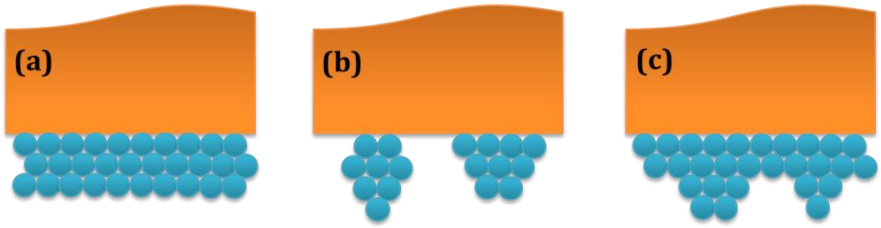

Figure 29: Thin film growth modes, (a) layer-by-layer growth, Frank-van der Merwe mode; (b) island growth, Volmer-Weber mode; (c) Stranski-Krastanov mode.

The other possibility of film condensation is that the growth starts in layer-by-layer mode and then changes to island growth mode. This mode is known as Stranski-Krastanov and it may happen when the lattice mismatch between substrate and film increases with the thickness.

2.2. PLD500 custom-designed

The PLD system used in this study was a custom-designed system shown in Figure 30 consisting of an ultra-high-vacuum chamber where the PLD process takes place.

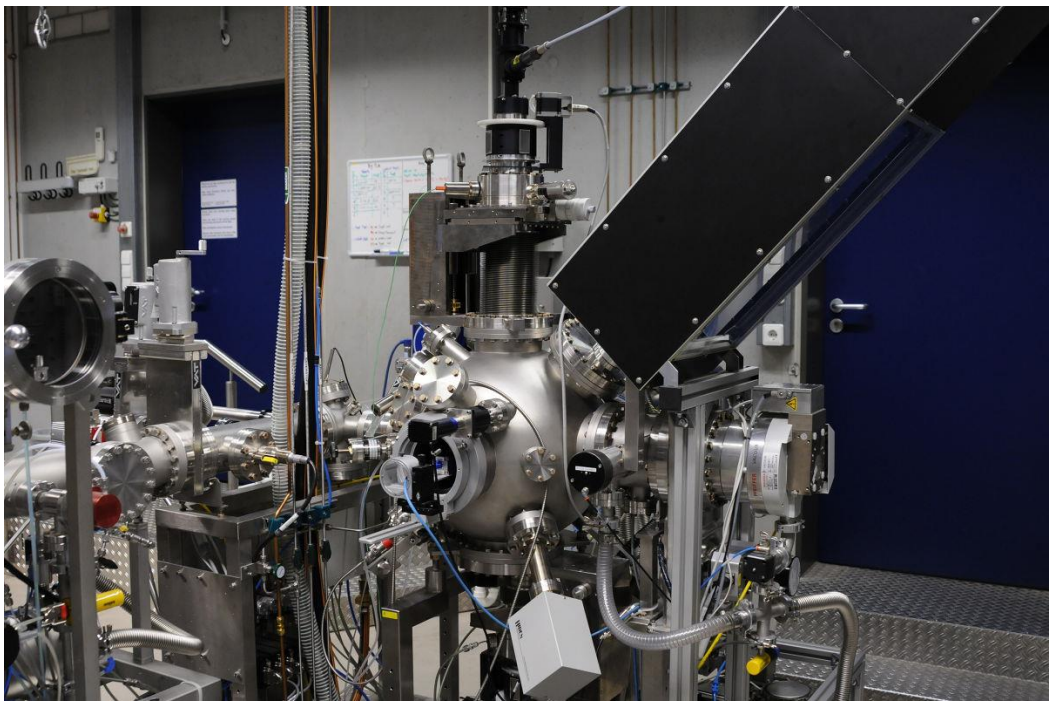

Figure 30: PLD500 custom-designed system

The laser pulses resulting from a KrF excimer laser pass through lenses and apertures. The squared-shaped laser beam is guided through a quartz window into the PLD chamber using a UV mirror. Right before the quartz window, a lens focuses the beam to a spot on the target with the size ranging from 1-5 mm^2.

The PLD500-custom designed system is utilized with a target (substrate) manipulator in which the target (substrate) can be moved horizontally and vertically. The target-manipulator is supplemented with six positions for six different targets. Each target individually can be rotated and horizontally swept in order to use the whole surface of the target during ablation. The target-substrate distance can be changed from 10-100 mm by vertical movement of substrate-manipulator.

Using an IR-laser, temperatures up to 1200 °C on the substrate can be achieved. This is attained by emitting directly the back side of the substrate or by means of using an intermediate metal plate.

Argon, nitrogen and oxygen are the process gases in PLD500-custom designed system which are conveyed into the chamber through individual mass flow controllers. By means of these mass flow controllers, one can adjust the flow of the gases from 1-100 standard cm^3/min (sccm). The base pressure of chamber is in the range of 5×10^{-8} Torr acquired by turbo molecular pump. The pressure during deposition can be changed from vacuum (base pressure) to ambient pressure thanks to the throttle gate valve with nominally 1000 defined steps.

The PLD500-custom designed system is utilized with a load-lock chamber, a storage chamber for loading the targets and the substrates separated from the PLD chamber by a gate valve. Using a magnetic arm, the loaded targets and substrates can be transferred to the PLD chamber. A residual gas analyzer is integrated in the chamber in order to probe the actual gas content of the chamber.

Reflection high-energy electron diffraction system is supplemented in order to monitor the growth mode of the thin film during deposition.

2.3. $La_{1-x}Sr_{1+x}MnO_4$ (x=0.0, 0.5) Target Preparation

As starting compounds, La_2O_3, $SrCO_3$ and Mn_2O_3 or MnO_2 were weighed, mixed and grinded in an agate mortar. For PLD target, the final product mass should be in the range of 4-5 grams. Since La_2O_3 and $SrCO_3$ are hygroscopic compounds, they have to be pre-baked. Therefore, La_2O_3 and $SrCO_3$ were baked at 1273 and 573 K for 12 and 5 hours, respectively. The mixed powder was calcined at 1633 K for 36 hours under argon atmosphere. During the calcination process, the following reactions (depends on the used manganese oxide) are expected to occur:

$$La_2O_3 + 2\ SrCO_3 + Mn_2O_3 \rightarrow 2\ LaSrMnO_4 + 2\ CO_2 \qquad (5)$$

$$La_2O_3 + 6\ SrCO_3 + 4\ MnO_2 \rightarrow 4\ La_{0.5}Sr_{1.5}MnO_4 + 6\ CO_2 + ½\ O_2 \qquad (6)$$

The calcination temperature is chosen based on the binary phase diagram of Sr-Mn-O system[9]. In this calculated SrO-MnO_x phase diagram, the single-layered and double-layered manganite *i.e.* Sr_2MnO_4 and $Sr_3Mn_2O_7$ are close in terms of Sr/Mn elemental ratio. Sr_2MnO_4 forms at above 1623 K, while $Sr_3Mn_2O_7$ formation temperature is calculated to be at above 1873 K.

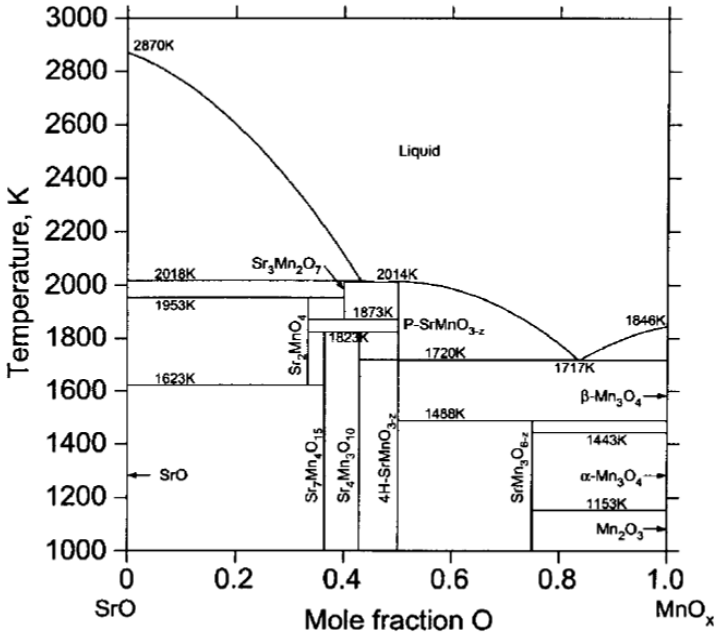

Figure 31: Calculated SrO-MnO_x phase diagram in air [94]. MnO_x represents all the possible oxidation states of Mn upon increase of temperature in air (look at the right-hand side axis).

The first trials of calcination under argon atmosphere in a non-tightly-closed system *i.e.* muffle furnace always led to formation of multiple phases including the simple perovskite manganite, double-layered manganite and remnant La_2O_3.

Table II: Possible oxidation state of Mn in single-layered, double-layered and perovskite manganite with the general formula of $La_{1-x}Sr_{1+x}MnO_4$, $La_{2-2x}Sr_{1+2x}Mn_2O_7$ and $La_{1-x}Sr_xMnO_3$, respectively.

Sr/La	$n = \infty$	$n = 2$	$n = 1$
1.0	$Mn^{3.5+}$	$Mn^{3.25+}$	Mn^{3+}
3.0	$Mn^{3.75+}$	$Mn^{3.625+}$	$Mn^{3.5+}$

A simple calculation of Mn oxidation state for perovskite and layered manganite shows that upon reducing the perovskite manganite, first a double-layered and then a single-layered manganite phase stabilizes (Table II).

[9] Thermodynamically, the only possible compound in La-Mn-O system is the perovskite $LaMnO_3$ which is stable above 1400 K [**93**] A. N. Grundy, M. Chen, B. Hallstedt, and L. J. Gauckler "Assessment of the La-Mn-O system" J Phase Equilib Diff **26**, 131 (2005).

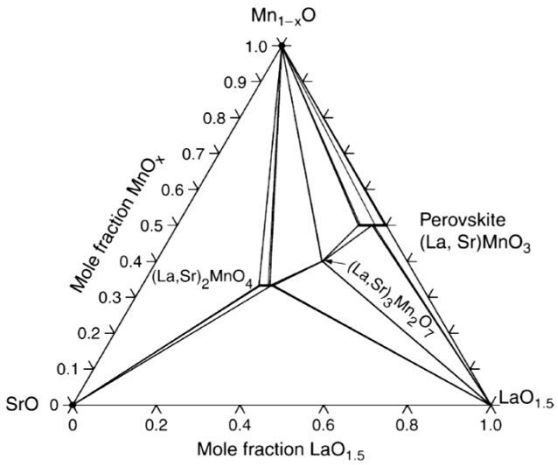

Figure 32: Isothermal ternary phase diagram of La-Sr-Mn-O system at 1073 K and $\log P_{O_2} = 10^{-18}\ bar$ [95].

Moreover, the isothermal ternary phase diagram of La-Sr-Mn-O system at 1073 K and $\log P_{O_2} = 10^{-18}\ bar$ (Figure 32) shows that both layered manganites in comparison to the perovskite manganite are stabilized (large area appointed to the two layered manganites). This reveals the necessity of having a reducing atmosphere during calcination in order to achieve the single-layered manganite.

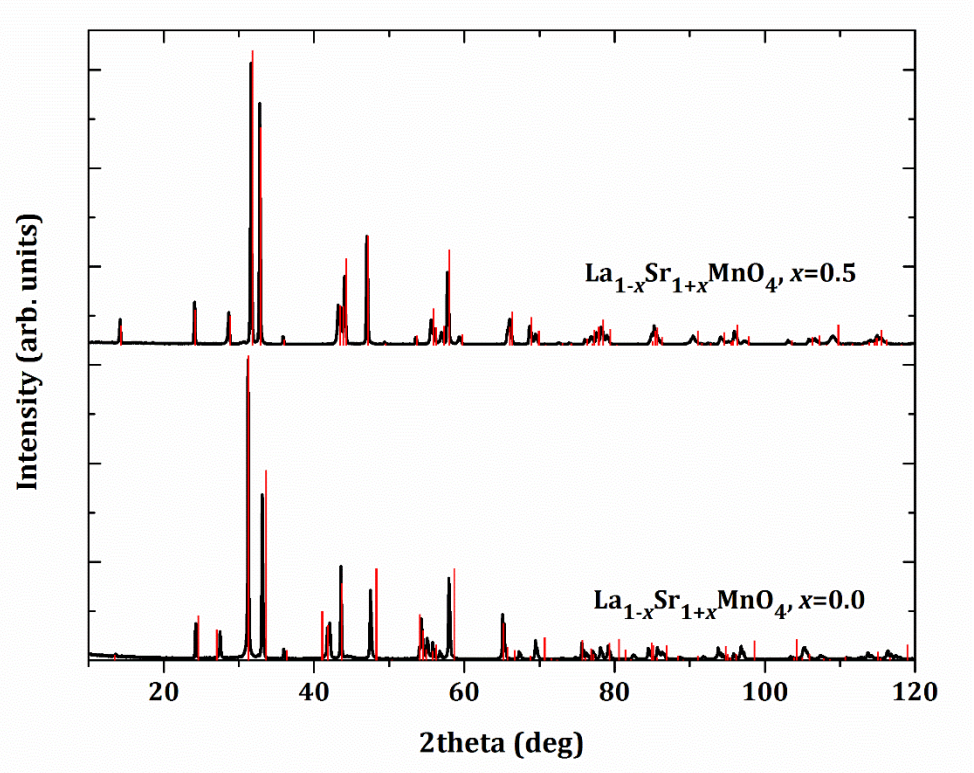

Figure 33: X-ray diffraction pattern of sintered $La_{1-x}Sr_{1+x}MnO_4$ (x=0.0, 0.5) targets.

Thus, the calcination process held in a vacuum furnace to obtain a closed atmosphere in order to provide a low partial pressure of oxygen (the oxygen will be provided from the starting

oxides diluted with heavy flow of argon *i.e.* 0.5 l/min). In this way, by pushing extra oxygen atoms out of the furnace using argon flow, a reducing atmosphere was obtained.
The calcination process repeated three times and followed by pressing the calcined powder into a disc using uniaxial press and sintered at 1773 K for 12 hours under argon atmosphere.
The x-ray diffraction pattern of the sintered targets are shown in Figure 33. All the reflections were indexed corresponding to single-layered manganite. For $La_{1-x}Sr_{1+x}MnO_4$ (x=0.0), a drift can be seen throughout the whole range leading to an inharmonic peak shift. This could be due to a slight deviation from x=0.0 doping level.

2.4. Thin Film Growth Conditions

The epitaxial $La_{1-x}Sr_{1+x}MnO_4$ thin films were deposited on (1 0 1) $NdGaO_3$ (NGO, pseudocubic lattice constants a=b=3.86 Å) and (0 0 1) $LaSrAlO_4$ (LSAO, a=b=3.756 Å) single crystal substrates (CrysTech GmbH). The single-oriented one-side-polished single crystal substrates where cleaned by acetone and isopropanol, later annealed in the chamber at 350 °C under oxygen pressure of 300 mTorr for half an hour. In this way, a clean surface of substrate can be obtained. A 248nm wavelength KrF excimer laser with a fluence of 0.6-1.8 J/cm^2 and repetition rate of 2-10 Hz ablated the target placed in the ultra-high vacuum PLD chamber. The temperature of the substrates was chosen between 650 and 900°C in an argon atmosphere of 50-350 mTorr and a flow rate of 10 sccm. The target-substrate distance was fixed at 40 mm. The deposition was conducted using a laser spot of 3.0 mm^2 for 5000 pulses which gives a film thickness of 10-12 nm. After deposition, the films were cooled down immediately to ambient temperature with a rate of 5-25°C/min.

3. Crystal Structure Analysis by X-ray Diffraction and X-ray Reflectometry

This chapter will start with describing briefly the fundamental aspects of X-Ray Diffraction (XRD) and X-Ray Reflectometry (XRR) and the characterization methods for thin films using XRD (Ref. [96-100]). Following, the experimental details of XRD and XRR measurements will be presented. Furthermore, it follows with XRD and XRR characterizations in order to study the effect of deposition pressure and temperature on crystal structure of the films. Finally, XRD and XRR characterizations of $La_{1-x}Sr_{1+x}MnO_4$ (x=0.0, 0.5) films on different substrates with different strain states will be presented.

3.1. Principles of X-ray Diffraction

X-rays are electromagnetic waves with the wavelengths in the range of angstroms. In quantum mechanical point of view, such wave is quantized by photons with certain energies and momentum. One of the interactions of the photons with matter is scattering. In a coherent scattering, the energy, and thus, the wavelength of incident beam before and after the interaction is conserved. Such scattering is, thus, *elastic* known as Thompson scattering. When the wavelength of scattered beam is different from the incident beam, the scattering is *inelastic*, incoherent and known as Compton scattering. Diffraction is an elastic scattering where the Bragg condition is satisfied. Each atom in the crystal scatters the x-rays elastically. The Bragg condition is satisfied when the scattered x-ray waves from planar arrays of the atoms, *i.e.* crystal planes, interfere constructively. The path difference of scattered x-rays in this sense is defined by the distance between the crystal planes. The Bragg's law describes the condition of such constructive interference as $n\lambda = 2d\sin\theta$ where λ, d, and θ are x-ray wavelength, interplanar crystal distance and scatter angle, respectively. The interplanar crystal distance in Bragg's law does not count the spacing between the atoms in the crystal, but the one in reciprocal lattice.

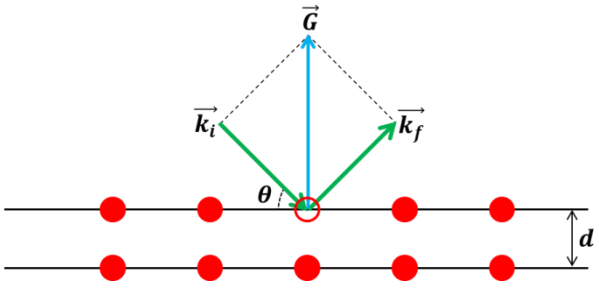

Figure 34: Schematic view of crystal planes shows an elastically scattered x-ray which satisfies Bragg condition.

In reciprocal lattice, each crystal plane is represented by a vector whose direction the normal of the plane and its length is the inverse of interplanar crystal distance. In other words,

reciprocal lattice translates and simplifies the 3D crystal space to a 2D vector space. Therefore, diffraction can be formulated as $\overrightarrow{k_f} - \overrightarrow{k_i} = \vec{G}$ (Laue equation) where $\vec{G}$ is the reciprocal lattice vector and $\overrightarrow{k_f}$ and $\overrightarrow{k_i}$ are the wave vectors of diffracted and incident x-rays, respectively (Figure 34). The scattered angle is defined by the lattice *d* spacing, while the intensity of diffracted x-ray depends on many factors. Two most important factors are *atomic form factor* and *structure factor*. Atomic form factor expresses the dependence of diffracted x-ray on electron density distribution of the atoms. Here, the scattering of an atom depends on the shape of the electron density function, and thus, atomic form factor sums such dependence over the whole structure. The Bragg and Laue equations have been derived for a single atom in the unit cell, the building block of the crystal. The intensity of the diffracted x-rays scales with the total charge distribution of multiple atoms constructing the unit cell. On the other hand, the structure factor expresses the dependence of diffracted x-ray intensity on the position of the atoms in the unit cell, *i.e.* Miller indices.

The discussion above is based on an assumption that the incident x-ray beam is being scattered by the atoms only once. In reality due to presence of several defects in the crystal structure, such assumption is correct. The theory which describes the diffraction upon single scatter event is called kinematical theory of diffraction. On the contrary, when the crystal is free of any defect, the incident x-rays transmit through the crystal and become scattered several times. This is known as multiple scattering where the kinematical theory of diffraction is violated. The theory which considers multiple scattering of the incident x-ray (Figure 35) and regards the interference of incident and diffracted x-rays in the crystal is called dynamical theory of diffraction.

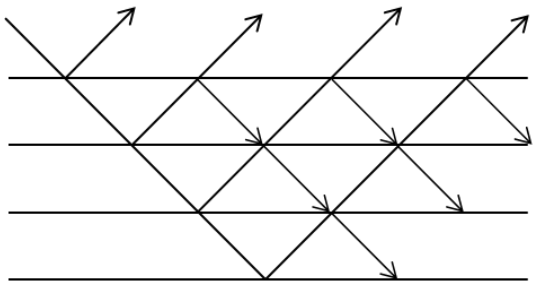

Figure 35: multiple reflections of incident x-ray which satisfy the Bragg condition for constructive interferences of a set of lattice planes.

The kinematical theory considers all the primary beams at all layers identical. Each time the primary beam passes a layer, it experiences a phase shift by which the position of reflected beam deviates from original Bragg reflection. In reality, the primary beams at all layers are not identical and the absorption of the photons by layers reduces the intensity of the beam.

In order to observe these deviated reflections (Laue fringes), there should be number of layers which reflect the beam in an exact similar geometrical way. This is the main reason why the Laue fringes cannot be detected in bulk materials with usual defects. Whereas, in layer-by-layer grown thin films, the condition for constructive multiple scatterings is obtained and as a result, the Laue fringes are detectable.

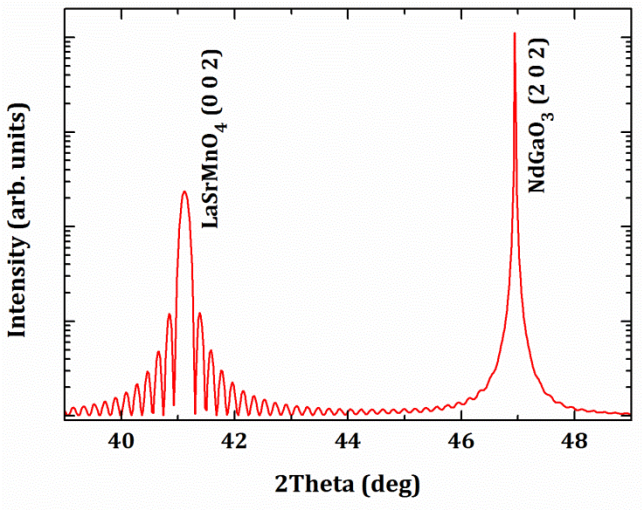

Figure 36: Simulated x-ray diffraction pattern of a perfect crystalline $LaSrMnO_4$ thin film on $NdGaO_3$ substrate. The in-plane strain is ignored.

Figure 36 shows a simulation of XRD pattern of $LaSrMnO_4$ thin film on $NdGaO_3$ substrate where the perfect crystalline layers of the film fulfill the multiple scattering criteria of the incident x-ray beam in the crystal and consequently, the Laue fringes appear on both side of the main reflection of the film.

3.1.1. Epitaxy

When the in-plane crystal parameters of the film follows the ones of the substrate, there is an epitaxy between film and substrate. The epitaxial grown thin films exhibit high degree of crystal perfection.

In this sense, due to the difference in lattice constants of the substrate and the film, a lattice mismatch $(\Delta a = a_s - a_f)$ occurs where a_s and a_f are in-plane lattice constants of the substrate and the film, respectively. The in-plane strain is defined as $\varepsilon = \frac{\Delta a}{a_s}$ where a positive (negative) sign reflects an in-plane tensile (compressive) strain. For the sake of conservation of unit cell volume, there will be also a(n) suppression (elongation) in out-of-plane lattice constant (Figure 37).

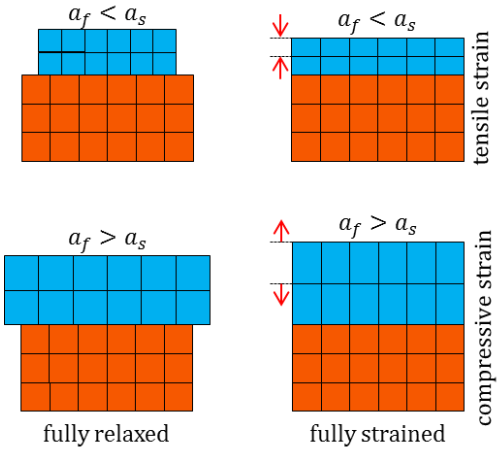

Figure 37: Schematic view of strain generation.

The conservation of unit cell volume follows Poisson's ratio (ν) which can be defined in first approximation by the ratio of the in-plane strain divided by the out-of-plane strain $\left(\nu = \frac{\varepsilon_a}{\varepsilon_c}\right)$ where ε_a and ε_c stand for in- and out-of-plane strains, respectively.

3.1.2. Rocking Curve Measurement

In XRD, the geometrical position of x-ray source and detector should be fixed to the periphery of the hemisphere of the measurement frame (Figure 38) in order to avoid the dependence of reflections intensity to the sample-detector distance. In $\theta/2\theta$ measurement, the out-of-plane reflection vector (Q_z), the normal to the surface of the sample, is measured. Therefore, the detector angle should be always twice as the x-ray source angle. When there is a deviation between the reflection vector (G) and the normal vector (Figure 38), the reflection vector contains both in- and out-of-plane (Q_x and Q_z) components. The origin of such deviation in thin films can be described as follows.

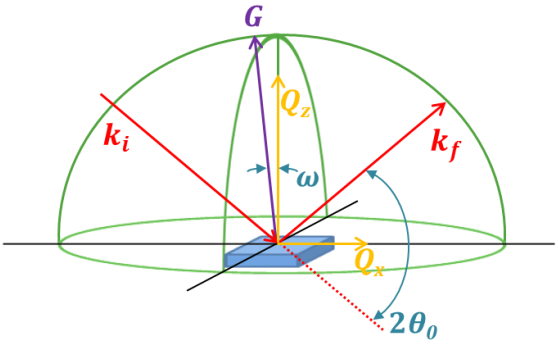

Figure 38: Visualization of XRD hemisphere geometry showing the in- (Q_x) and out-of-plane (Q_z) vector components.

In thin film growth with a preferential crystal orientation, the so called textured structure forms. Such preferred orientation is favorable in order to minimize the energy of the system with minimum lattice mismatch.

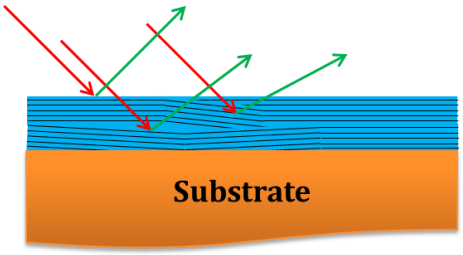

Figure 39: Schematic view of single oriented thin film forming domains with slight rotation with respect to the preferred texture structure.

The epitaxial thin films usually exhibit a slight deviation from the single oriented texture structure originating from minutely distorted domains (Figure 39). The measurement which reveals such deviations in highly textured films is rocking curve measurement as it measures the deviation of the reflection vector from the normal (Figure 38).

The rocking curve measurement is about having the detector fixed at the Bragg reflection angle ($2\theta_0$) and tilting the sample in the vicinity of the Bragg angle (θ_0). In other words, what will be measured is the deviation from Bragg angle (θ_0) which can be written as ($\omega = \theta - \theta_0$). In this study, instead of tilting the sample, the x-ray source ($\overrightarrow{k_i}$) scanned the sample (ω scan) while the detector position ($\overrightarrow{k_f}$) was fixed.

3.1.3. Reciprocal Space Mapping

As it is discussed in section 3.1.1, epitaxy results in generation of in-plane tensile or compressive strains due to crystal lattice mismatch between the film and the substrate. In this context, the substrate-film epitaxial relation can be probed by performing a reciprocal space mapping (RSM).

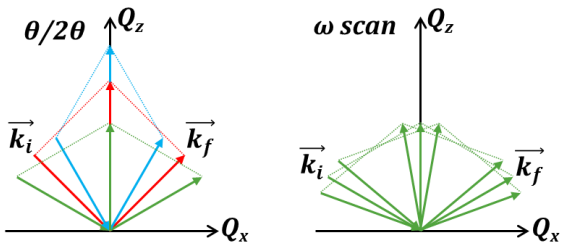

Figure 40: Representation of $\theta/2\theta$ (right-hand side) and ω (left-hand side) scan.

For RSM measurement, a set a $\theta/2\theta$ scans at various ω angles or a set of ω scans at various θ angles will result in a 2D map consisting of the distribution of in- and out-of-plane reflections

of the film and substrate where $\theta/2\theta$ and ω scans register out-of-plane (Q_z) and in-plane (Q_x) counterparts, respectively (Figure 40). In other words, using RSM, one can investigate directly and simultaneously the lattice constants of the film and the substrate.

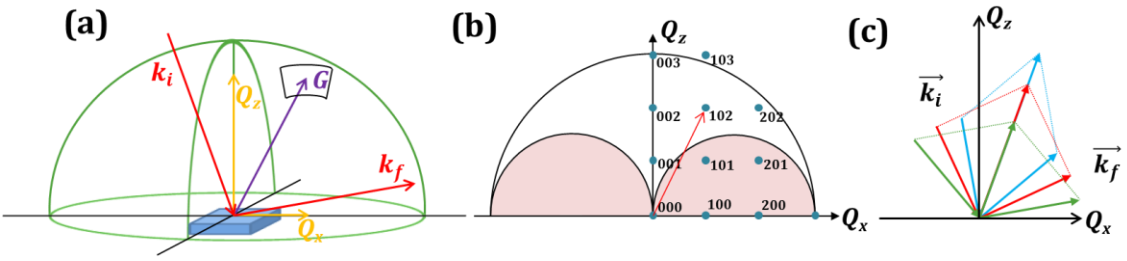

Figure 41: Representation of asymmetric reciprocal space mapping. (a) Schematic view of measurement frame; (b) Visualization of reciprocal space shows the Miller indices where the pink color filled areas are the forbidden zones of measurement. (c) Combination of $\theta/2\theta$ and ω scans.

In order to measure the asymmetric reflection (*e.g.* (102) reflection in Figure 41b), the source and detector must be rotated to fulfill the Laue condition for desired reflection (Figure 41a). The Q space representation can be combined easily with reciprocal space visualization if the sample crystal orientation is known. This means that combining the reciprocal spaces of the film and the substrate gives clearly the range of $\theta/2\theta$ and ω scans (Figure 41c).

3.2. Principles of X-ray Reflectometry

According to Snell's law of refraction, the sine of incoming and outgoing wave passing through a boundary between two different media is proportional to refractive indices of the media. Here, the incoming (refracted) angle θ (θ_R) is the angle between incoming (refracted) x-ray and surface of the sample. Thus, the Snell's law for a passing x-ray through the boundary between sample and air can be written as $\frac{1}{n} = \frac{\cos\theta}{\cos\theta_R}$ where n is the refractive index of the sample (Figure 42).

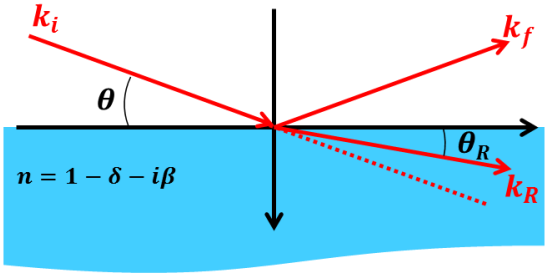

Figure 42: Representation of Snell's law for x-ray incident beam passing through the sample.

The refractive index of the sample is a function of electron density (δ) and absorption (β) of the sample.

For the angles smaller than so called critical angle (θ_c), the beam does not penetrate into the substance and a pure reflection occurs. In Figure 43, the simulations of $La_{1-x}Sr_{1+x}MnO_4$ thin films on $NdGaO_3$ substrate are presented. A typical XRR curve consists of a plateau at the $\theta < \theta_c$ and a steep part with decreasing intensity which evolves the both reflection and refraction phenomena. The θ_c on these curves could be evaluated by considering the first derivations in the vicinity of transition point from the flat plateau and the steep part. Applying approximation of cosines as $1 - \frac{\theta^2}{2}$ for small θ angles in the Snell's law, the critical angle can be written as a function of electron density and absorption of the sample.

$$\theta_c = \sqrt{2\delta - 2i\beta} \qquad (7)$$

Neglecting the absorption of x-ray by the film, the equation (7) relates the critical reflection angle to electron density and indirectly to the actual density of the sample.

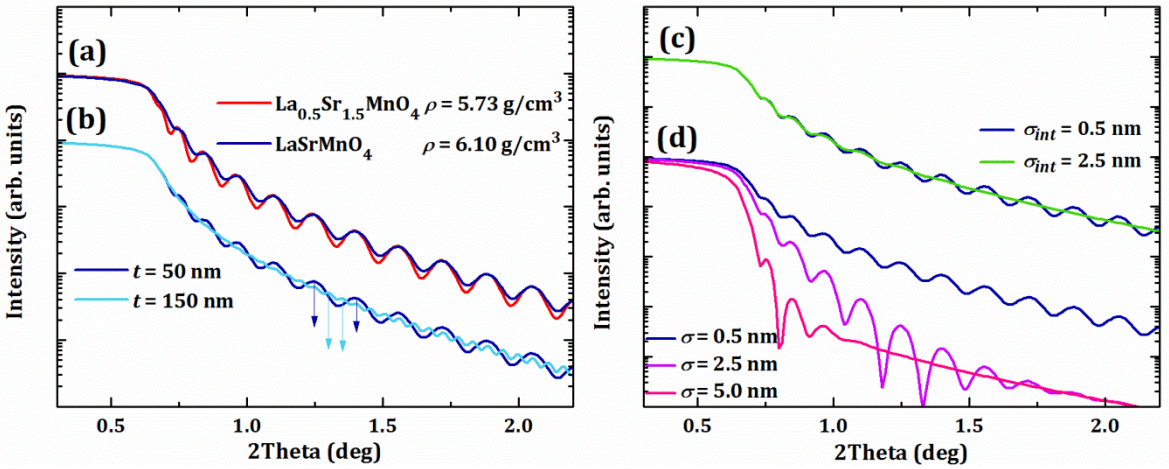

Figure 43: Simulation of XRR curves of $La_{1-x}Sr_{1+x}MnO_4$ (x=0.0, 0.5) thin films on $NdGaO_3$ substrate. (a) 50 nm $La_{1-x}Sr_{1+x}MnO_4$ (x=0.0, 0.5) films; (b) 50 and 150 nm $La_{1-x}Sr_{1+x}MnO_4$ (x=0.0) films; (c) 50 nm $La_{1-x}Sr_{1+x}MnO_4$ (x=0.0) films with different interface roughness (σ_{int}); (d) 50 nm $La_{1-x}Sr_{1+x}MnO_4$ (x=0.0) films with different surface roughness (σ). The arrows in (b) point the position of two consecutive oscillations.

As it is shown in Figure 43a, the θ_c of XRR curves of 50 nm $La_{1-x}Sr_{1+x}MnO_4$ (x=0.0, 0.5) films on $NdGaO_3$ substrate changes slightly by doping Sr to the structure showing the difference in their densities (5.73 and 6.1 g/cm^3 for (x=0.5) and (x=0.0), respectively). Therefore, knowing the density of the substrate, one can effectively evaluate the density of the film by fitting the corresponding measured XRR curve.

The most important feature in XRR curves is the occurrence of intensity oscillation which is known as Kiessig fringes. The Kiessig fringes appear due to the difference in electron density of film and substrate, so the phase shift in reflected/refracted x-rays. The maximum (minimum) intensity of the fringes will occur when a constructive (destructive) interference of outgoing x-ray forms. As a result the difference in angles of two consecutive maxima of the

fringes reveals the film thickness. The number of fringes increases with increase in the film thickness as it is demonstrated in Figure 43b.

The rough interface between film and substrate eliminates the amplitude of the fringes (Figure 43c), while increase in roughness of the film surface affects the XRR curve drastically (Figure 43d).

3.3. X-ray Diffraction and X-ray Reflectometry Measurements Setup

The crystal structure of epitaxial thin films in most of the cases is deviated from perfect crystals. Investigation on such crystal structures should be conducted using high resolution XRD and XRR. To fulfill this condition, the x-ray beam has to be monochromated. In this study, the XRD and XRR measurements were performed using a Rigaku SmartLab four- circle diffractometer with a Cu $K\alpha_1$ x-ray source (λ=1.54056 Å). A schematic view of the diffractometer is shown in Figure 44.

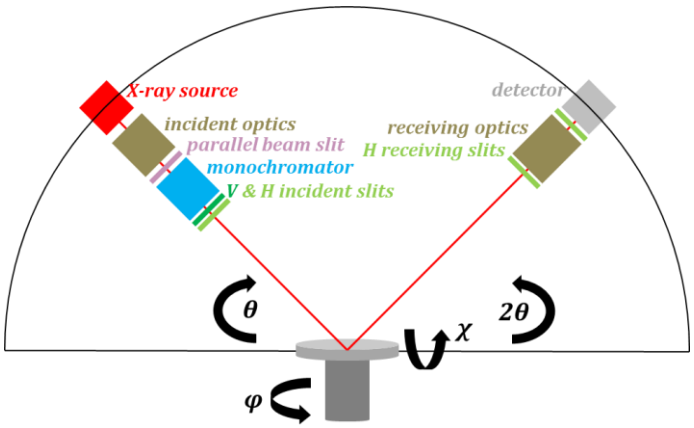

Figure 44: Schematic view of Rigaku SmartLab four- circle diffractometer. Regarding incident and receiving slits, *V* and *H* denotes vertical and horizontal, respectively.

In this setup, the beam is monochromatized using a 2-bounce Ge-monochromator. Despite of monochromated beam, the angular diversity of the beam has to be narrowed using firstly by parallel beam slit to change the divergent x-rays known as Bragg-Brentano mode to the parallel beam mode and secondly a set of proper incident and receiving slits (Figure 44). Since in this study, the thin films were deposited on 5 × 5 mm single crystal substrates, a horizontal 1 mm and a vertical 2 mm incident slit cut the beam to a 2 × 1 mm x-ray spot. On the detector side, the reflected beam was narrowed twice using two horizontal 0.5 mm slits. The samples were aligned prior to the actual measurement to the most intense peak of the single oriented substrate with respect to height and the normal of the surface.

For RSM measurement, the samples were aligned not only to the out-of-plane direction but also to the in-plane direction by means of performing the φ scan (Figure 44).

The slit selection for XRR measurement was different since the in-plane beam divergence should not exceed 0.05°. Thus, the vertical incident slit kept as 2 mm, but the horizontal one was narrowed to 0.1°. On the detector side, the receiving slits were selected as 0.2 and 0.4°, consequently.

3.4. The Effect of Growth on Crystal Structure of $La_{1-x}Sr_{1+x}MnO_4$ Thin Films

One of the biggest obstacles for thin film deposition of single-layered manganite $La_{1-x}Sr_{1+x}MnO_4$ phase is formation of competing double-layered manganite $La_{2-2x}Sr_{1+2x}Mn_2O_7$ compound (see section 2.3).

Table III: Crystal parameters of $La_{1-x}Sr_{1+x}MnO_4$ series. All compounds crystallize in tetragonal *I*4/*mmm* structure.

Compound	Space group	"*a*" lattice constant (Å)	"*c*" lattice constant (Å)	Unit cell volume (Å^3)	Density (g/cm^3)
x=1.0	139	3.802	12.519	180.98	5.398 [101]
x=0.6	139	3.857	12.405	184.54	5.663 [32]
x=0.5	139	3.861	12.426	185.24	5.734 [102]
x=0.25	139	3.84	12.651	186.55	5.922 [32]
x=0.0	139	3.786	13.163	188.68	6.081 [32]

Table IV: Crystal parameters of $La_{2-2x}Sr_{1+2x}Mn_2O_7$ series. All compounds crystallize in tetragonal *I*4/*mmm* structure.

Compound	Space group	"*a*" lattice constant (Å)	"*c*" lattice constant (Å)	Unit cell Volume (Å^3)	Density (g/cm^3)
x=1.0	139	3.8	20.096	290.186	5.548 [103]
x=0.5	139	3.875	20.032	300.793	5.919 [18]
x=0.45	139	3.873	20.056	300.843	5.974 [18]
x=0.4	139	3.868	20.105	300.799	6.031 [104]
x=0.35	139	3.865	20.177	301.409	6.075 [18]
x=0.3	139	3.872	20.258	303.716	6.086 [105]
x=0.0	139	3.868	20.205	302.296	6.452 [106]

Both phases crystallize in tetragonal structure (space group 139, *I*4/*mmm*) at room temperature in the whole range of doping levels. Moreover, in-plane lattice constant of both series changes very minutely as it is listed in Table III and Table IV. As a consequence, if thermodynamic conditions (pressure and temperature) satisfy formation of both compounds, there will be a high chance to grow a thin film consisting of both phases. In SrO-MnO system (Figure 31), between 1873 and 1953 K, for example both Sr_2MnO_4 and $Sr_3Mn_2O_7$ phases are

thermodynamically stable. Yet due to similar in-plane lattice constants, both phases could form single oriented for instance in (0 0 *l*) orientation.

As it is demonstrated in Figure 45a, along with reflections of single oriented $La_{1-x}Sr_{1+x}MnO_4$ (x=0.0) phase, there are (0 0 *l*) reflections of $La_{2-2x}Sr_{1+2x}Mn_2O_7$ phase as well. The in-plane lattice constant of almost all members of double-layered manganite is in the range of 3.86-3.87 Å which leads to a small lattice mismatch with NGO. However, the measured *c* lattice of $La_{2-2x}Sr_{1+2x}Mn_2O_7$ phase is bigger than any of double-layered manganite series. That is why based on the observed reflection, it is hard to judge about the doping level of $La_{2-2x}Sr_{1+2x}Mn_2O_7$ phase. By adjusting deposition conditions such as temperature and pressure, consistence of $La_{2-2x}Sr_{1+2x}Mn_2O_7$ phase could be effectively reduced as it is presented in Figure 45b. For this single phase film, the Laue fringes around (0 0 *l*) reflections of $La_{1-x}Sr_{1+x}MnO_4$ show that crystal quality is improved as well.

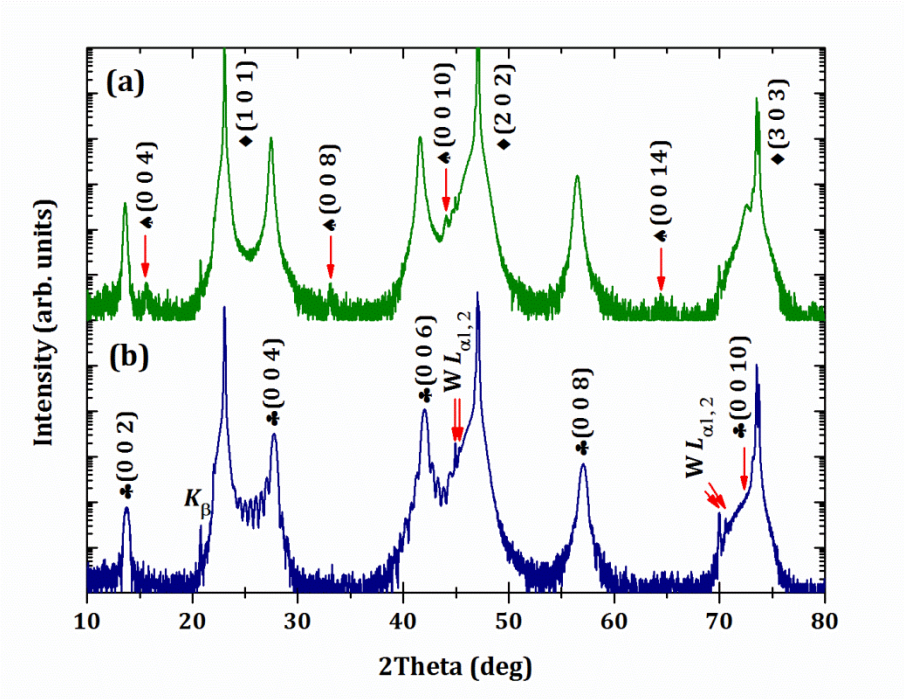

Figure 45: X-ray diffraction pattern of epitaxial (0 0 *l*) $La_{1-x}Sr_{1+x}MnO_4$ (x=0.0) thin film deposited on (1 0 1) NGO substrate (a) with $La_{2-2x}Sr_{1+2x}Mn_2O_7$ phase; (b) free of secondary phase. Reflections assigned with ♦, ♠ and ♣ correspond to NGO substrate, $La_{2-2x}Sr_{1+2x}Mn_2O_7$ and $La_{1-x}Sr_{1+x}MnO_4$ (x=0.0) phases, respectively. Intensity is in the logarithmic scale. For these measurements, the x-ray monochromator was not used, thus, *K*β and W *L*α$_1$ and *L*α$_2$ peaks can be seen.

In order to eliminate the content of the secondary phase (double-layered manganite) in the films, the deposition temperature and pressure were changed systematically. The other criterion to find the best deposition parameter was to have the closest *c* lattice to the single crystal of $La_{1-x}Sr_{1+x}MnO_4$ (x=0.0). Since the in-plane lattice constant of NGO is bigger than $La_{1-x}Sr_{1+x}MnO_4$ (x=0.0) film by about 0.07 Å, a remarkable in-plane strain of 1.9% will be

generated. Accordingly, a suppression in the *c* lattice of epitaxially strained film occurs. Hence, studying the effect of deposition parameters on the *c* lattice of strained films is not relevant. To overcome this problem, the film were grown relatively thick (more than 150 nm) where he in-plane lattice parameter of the film so called relaxes to the bulk values. Over 60 samples with a relative thickness of 150 nm were deposited on NGO substrate where the deposition temperature and pressure were changed in range of 770-870 ˚C and 150-330 mTorr, respectively.

Figure 46a shows the intensity ratio of (0 0 6) $La_{1-x}Sr_{1+x}MnO_4$ (x=0.0) to (0 0 10) $La_{2-2x}Sr_{1+2x}Mn_2O_7$ as a function of deposition temperature and pressure. The highest ratio is achieved in the deposition window of 820-840 ˚C and 150-220 mTorr. For the film with highest ratio, the intensity of (0 0 10) reflection of $La_{2-2x}Sr_{1+2x}Mn_2O_7$ phase was in the range of background noise.

Furthermore, as it is shown in Figure 46b, at higher temperatures and lower pressures, the *c* lattice constant increases and at maximum reaches the value of 13.06 Å, still smaller than the one of the single crystal (see Table III). With a good approximation, *c* lattice constant represents the unit cell volume and indirectly the oxygen content.

The two blue and red regions in Figure 46b (small and big *c* lattice constants) fall on the diagonal of the plot representing a classical thermodynamical dependence of oxygen content to the temperature and pressure.

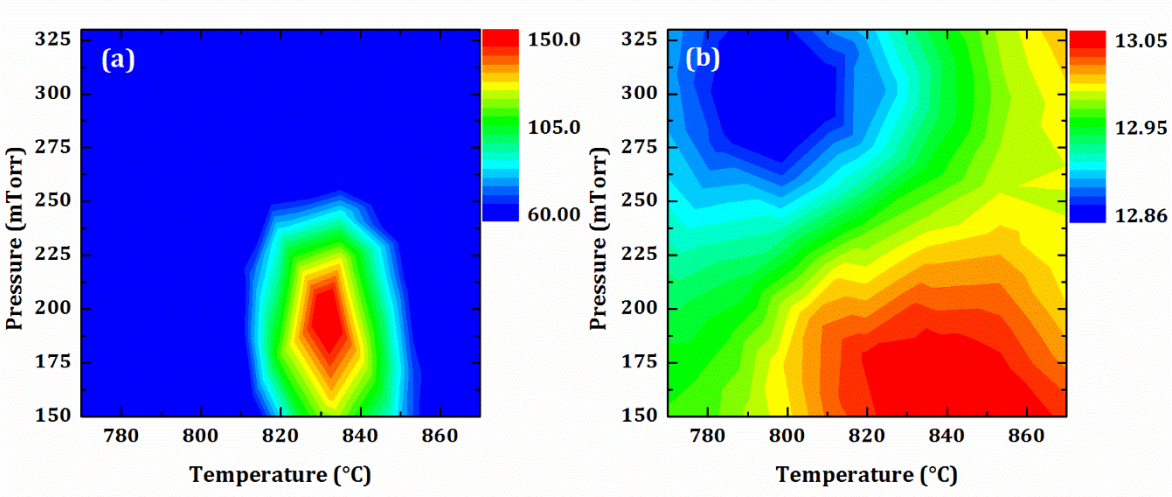

Figure 46: (a) Intensity ratio of (0 0 6) $La_{1-x}Sr_{1+x}MnO_4$ (x=0.0) to (0 0 10) $La_{2-2x}Sr_{1+2x}Mn_2O_7$ "the most intense reflection of each phases" as a function of deposition temperature and pressure; (b) Out-of-plane lattice constant (Å) as a function of deposition temperature and pressure.

It can be stated that at higher pressure of argon (lower partial pressure of oxygen) and lower temperatures, the thin films become oxygen deficient and therefore the unit cell volume is

shrunk. Following the temperature scan, at 870 ˚C (various pressures), a minute difference in *c* lattice constant can be observed revealing a temperature dominated region.

Comparing Figure 46a and b, one notices that within the deposition window of 820-840 ˚C and 150-220 mTorr where lowest amount of double-layered manganite phase had been detected, the closest *c* lattice constant to the bulk value is achieved as well. This means that when the deposition conditions are thermodynamically in favor of formation of $La_{1-x}Sr_{1+x}MnO_4$ (x=0.0) phase, the content of $La_{2-2x}Sr_{1+2x}Mn_2O_7$ phase reduces drastically, and at the same time perhaps due to having a stoichiometric oxygen content, the *c* lattice of $La_{1-x}Sr_{1+x}MnO_4$ (x=0.0) approaches to the values of the single crystal.

At the next step, the defined deposition window was used to grow thin film with less than 30 nm thickness and a fine tuning of the deposition parameters was performed. In Figure 47a-c, XRD patterns of films deposited at 200 mTorr and 800-850˚C are shown. Note that all three films show Laue oscillations and as temperature increases, fringes become more visible indicating better crystal quality. Rocking curve measurements on (0 0 6) reflection of $La_{1-x}Sr_{1+x}MnO_4$ (x=0.0) (not shown here) reveal narrow peaks with FWHM ≃ 0.06˚ indicating a low mosaicity (good crystal quality). At the first glance on the 2θ angel of the (0 0 *l*) reflection of the films, almost no change in *c* lattice constant could be observed by increase in deposition temperature. This is in accordance with the counter map presented in Figure 46b where at the deposition pressure of 200 mTorr, the *c* lattice changes very slightly upon increase in deposition temperature.

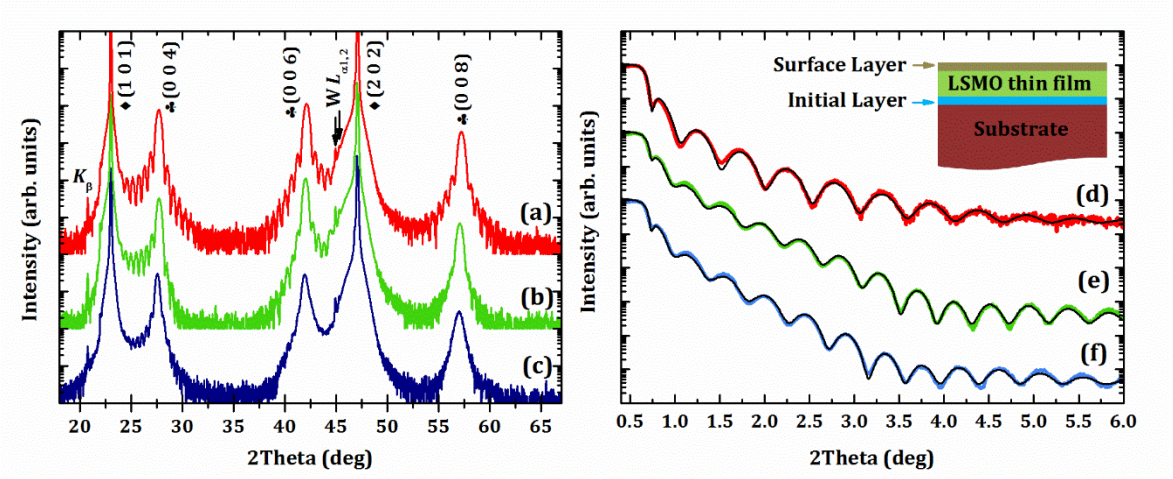

Figure 47: X-ray diffraction pattern of epitaxial (0 0 *l*) $La_{1-x}Sr_{1+x}MnO_4$ (x=0.0) thin films deposited on (1 0 1) NGO substrate at (a) 850; (b) 825 and (c) 800˚C. Reflections assigned with ♦ and ♣ belong to NGO substrate and $La_{1-x}Sr_{1+x}MnO_4$ (x=0.0) film, respectively. For these measurements, the x-ray monochromator was not used, thus, *K*β and W $L\alpha_1$ and $L\alpha_2$ peaks can be seen. X-ray reflectivity of the thin films deposited at (d) 850; (e) 825 and (f) 800˚C. The fitted curves are shown as black narrow lines.

In Figure 47d-f, XRR curves of the films are presented. Fitting XRR curves reveals that all the three films consist of a triple-layered structure. At the interface, there is always a thin initial layer (>1 nm) with density around ~ 8.5 g/cm^3. Similarly at the surface, another thin layer with thickness of 1-2 nm forms. The density of the surface layer is less than the film. However, the density value is not constant which could be due to presence of dangling bonds or uncompleted unit cells or even energetically modified top layers. Interfaces between these three layers as well as surface roughness are very smooth (>1 nm rsm).

Thicknesses of the films are evaluated by fitting the XRR curves (Table V). Alternatively, the thickness can be evaluated by considering the Laue oscillations using following equation [107]:

$$t = \frac{3\lambda}{2(sin\theta^{+} - sin\theta^{-})} \qquad (8)$$

where t stands for the thickness, λ is the wavelength of Cu K_α (average of $K\alpha_1$ and $K\alpha_2$, 1.5418 Å) and finally θ^{+} and θ^{-} are the angels of Laue fringes right after and before the main reflection, respectively. The thickness of the films calculated out of XRR curves (apart from the layers at interface and on the surface) is quite close to what is evaluated using the equation (8) (Table V). This implies that the proposed triple layer structure for the films is valid since the contribution of initial and surface layers cannot be reflected in Laue fringes.

Table V: Lattice parameters, density and thickness of thin (>30 nm) $La_{1-x}Sr_{1+x}MnO_4$ (x=0.0) films calculated out of XRD and XRR measurements.

T (°C)	c (Å) *Nelson-Riley*	c (Å) *RSM*	a (Å) *RSM*	V (Å^3) *RSM*	ρ (g/cm^3) *XRR*	Molar Mass (gr)	d (nm) *XRR*	d (nm) *Laue Oscillations*
800	12.92(4)	12.95(6)	3.85(6)	192.63(9)	6.1(5)	356.6(0)	20.0(7)	20.0(0)
825	12.90(9)	12.93(6)	3.85(8)	192.54(1)	6.0(9)	352.9(4)	20.5(0)	19.6(8)
850	12.85(6)	12.88(6)	3.86(3)	192.29(5)	5.9(9)	346.7(1)	16.6(7)	16.8(2)

To calculate c lattice constant, *Nelson-Riley function* $\left(\frac{cos^2\theta}{\theta} + \frac{cos^2\theta}{sin\,\theta}\right)$ was used and plotted for (*0 0 l*) reflections (Table V). In fact, the fits cannot be done reasonably since slopes of plots (c lattice vs. *Nelson-Riley function*) were not always negative and standard deviation was considerable. To evaluate in- and out-of-plane lattice constants precisely, reciprocal space mapping (RSM) was performed on (1 0 9) asymmetric reflection of $La_{1-x}Sr_{1+x}MnO_4$ (x=0.0) films which is in the vicinity of (3 2 3) reflection of NGO substrate in the reciprocal space (Figure 48). First of all, the q_x of the films and the substrate are on a straight line showing an epitaxial relation where the films are totally strained. Secondly, the q_z of the films deposited at higher

temperatures is slightly closer to the substrate. This means that the *c* lattice constant become slightly smaller with increase in deposition temperature in agreement with the XRD patterns (Figure 47a-c).

Using equations (9)-(11), *a* and *c* lattice constants of the films are evaluated directly from RSM.

$$q_{\perp} = \frac{1}{d_{\perp}} * l\,,\; Q_{||} = \frac{1}{d} * h \tag{9}$$

where

$$q_z = Q_{\perp} = \frac{2\pi}{\lambda} \sin\theta \cos(\theta - \omega) \tag{10}$$

and

$$q_x = Q_{||} = \frac{2\pi}{\lambda} \sin\theta \sin(\theta - \omega) \tag{11}$$

where h and l are Miller indices and ω and θ are incident and reflectance angles, respectively.

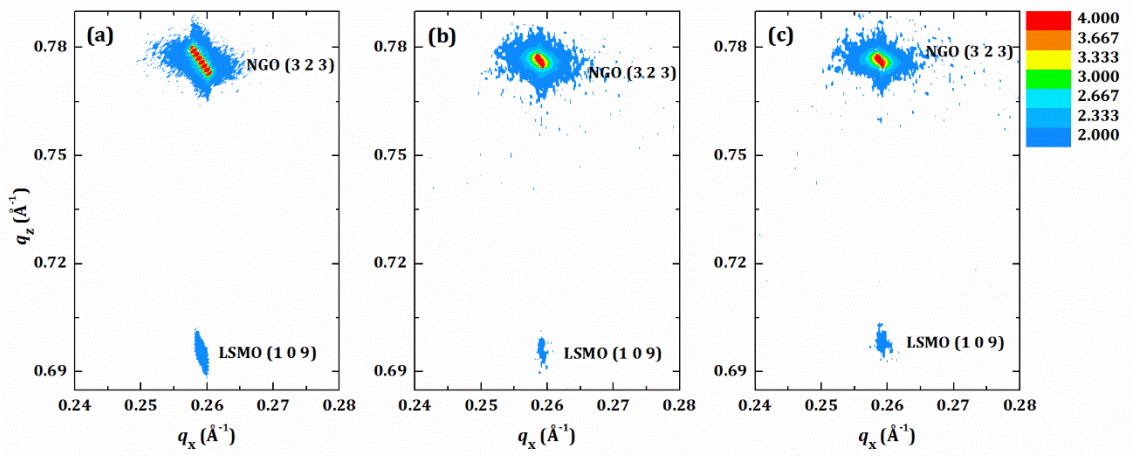

Figure 48: Reciprocal space maps of (1 0 9) asymmetric reflection of $La_{1-x}Sr_{1+x}MnO_4$ (x=0.0) films deposited on (1 0 1) NGO substrate at (a) 800; (b), 825 and (c) 850˚C. Intensity is in logarithmic scale. The (1 0 9) reflection of film is in the vicinity of (3 2 3) reflection of NGO substrate. RSM of the film deposited at 800˚C (a) was recorded with higher integration time showing a higher resolution.

Comparing evaluated *c* lattice constants from *Nelson-Riley function* and RSM, there is always 0.03 nm difference showing uncertainty in former one (Table V).

The results shown in Table V reveal that the in-plane lattice constant as it was expected is similar to the substrate (strained films). Hence, the slight increase in out-of-plane lattice constant results in slight increase in unit cell volume.

Considering the evaluated unit cell volume from RSM measurements and density from XRR curve fittings, the molar mass of the films can be calculated. As it is shown in Table V, the calculated molar mass for the films decreases from 356.6 to 346.7 gram upon increase in

deposition temperature. Since the molar mass of $La_{1-x}Sr_{1+x}MnO_4$ (x=0.0) is 345.5 gram, hence, the film deposited at 850 °C has the closest value to the bulk. To summarize, based on the unit cell volume and density as well as crystal quality, the deposition parameters for growth of $La_{1-x}Sr_{1+x}MnO_4$ (x=0.0) thin film with thickness less than 30 nm is found to be 200 mTorr and 850 °C as deposition pressure and temperature, respectively. Moreover, it was found that through the film deposition, formation of initial layer at the interface and surface layer as the topmost layer is inevitable.

3.5. Strain Engineered $La_{1-x}Sr_{1+x}MnO_4$ (x=0.0, 0.5) Thin films

In order to study the effect of in-plane strain on the orbital occupation of Mn atoms, $La_{1-x}Sr_{1+x}MnO_4$ (x=0.0, 0.5) thin films were deposited on NGO and LSAO substrates at deposition temperature and pressure of 850 ˚C and 200 mTorr, respectively, under argon atmosphere with the fluence of 0.75 J/cm^2 and repetition rate of 2 Hz. Thickness of all films kept between 12-25nm (~10-20 unit cell) in order to avoid relaxation of the films. In such range of thicknesses, one should keep it in mind that below critical thickness, the magnetic and electronic structure are considerably different from the bulk. The critical thickness has not been investigated in this thesis by means of electrical and magnetic characterization[10]. However, the similar study on the perovskite $La_{1-x}Sr_xMnO_3$ (x=0.3) is a good starting point. As it is shown in Figure 49, an insulator non-magnetic state instead of a metallic ferromagnet state was observed for $La_{1-x}Sr_xMnO_3$ (x=0.3) thin films below the critical thickness [108]. The critical thickness for this perovskite manganite was estimated to be around 10 unit cells. The 10 unit cell limit has been obeyed for $La_{1-x}Sr_{1+x}MnO_4$ (x=0.0, 0.5) thin films.

[10] The magnetization measurement on the $La_{1-x}Sr_{1+x}MnO_4$ (x=0.0, 0.5) thin films was not possible due to tiny magnetic contribution of the film showing magnetic moment in the range of 10^{-8}-10^{-9} emu. This is the resolution limit of most SQUID magnetometers. The resistance of the films considering the 10-20 nm thickness shows a value of several gigaohm.

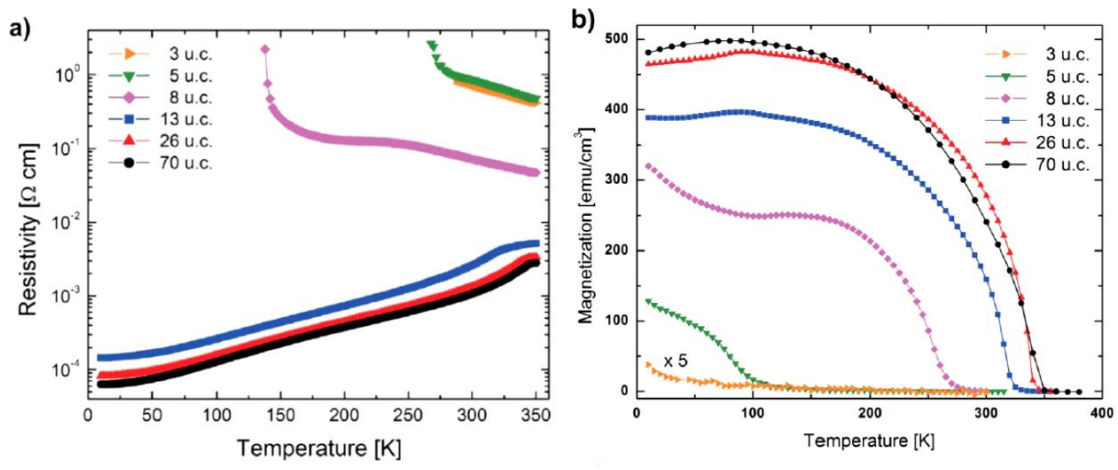

Figure 49: Temperature dependent (a) resistivity and (b) magnetization of $La_{1-x}Sr_xMnO_3$ (x=0.3) thin films with various thickness (u.c. stands for unit cell) [108].

In Figure 50a-b, the XRD patterns of $La_{1-x}Sr_{1+x}MnO_4$ (x=0.0, 0.5) films deposited on NGO substrate are shown. The most intense (0 0 l) reflection of $La_{2-2x}Sr_{1+2x}Mn_2O_7$ phase can be seen on both patterns. It should be mentioned that in order to filter the $K\beta$ and $K\alpha_2$ reflections out, for these measurements, the Ge-2 bounce monochromator was used. Therefore, the shoulders which usually appear around the substrate reflections are diminished, so (0 0 10) reflection of $La_{2-2x}Sr_{1+2x}Mn_2O_7$ comparing to pattern shown before (Figure 47a-c) is more visible. Rocking curve measurements which are shown in the insets reveal good crystal quality with the FWHM of 0.06 degrees. The Laue fringes around (0 0 l) reflections of $La_{1-x}Sr_{1+x}MnO_4$ (x=0.5) film are present but less pronounced. The thickness of this particular film is the highest among the four (see Table IV).

Having a look at Figure 50c-d, the XRD patterns of $La_{1-x}Sr_{1+x}MnO_4$ (x=0.0, 0.5) films deposited on LSAO substrate, one notices that $La_{2-2x}Sr_{1+2x}Mn_2O_7$ phase in these films disappears.

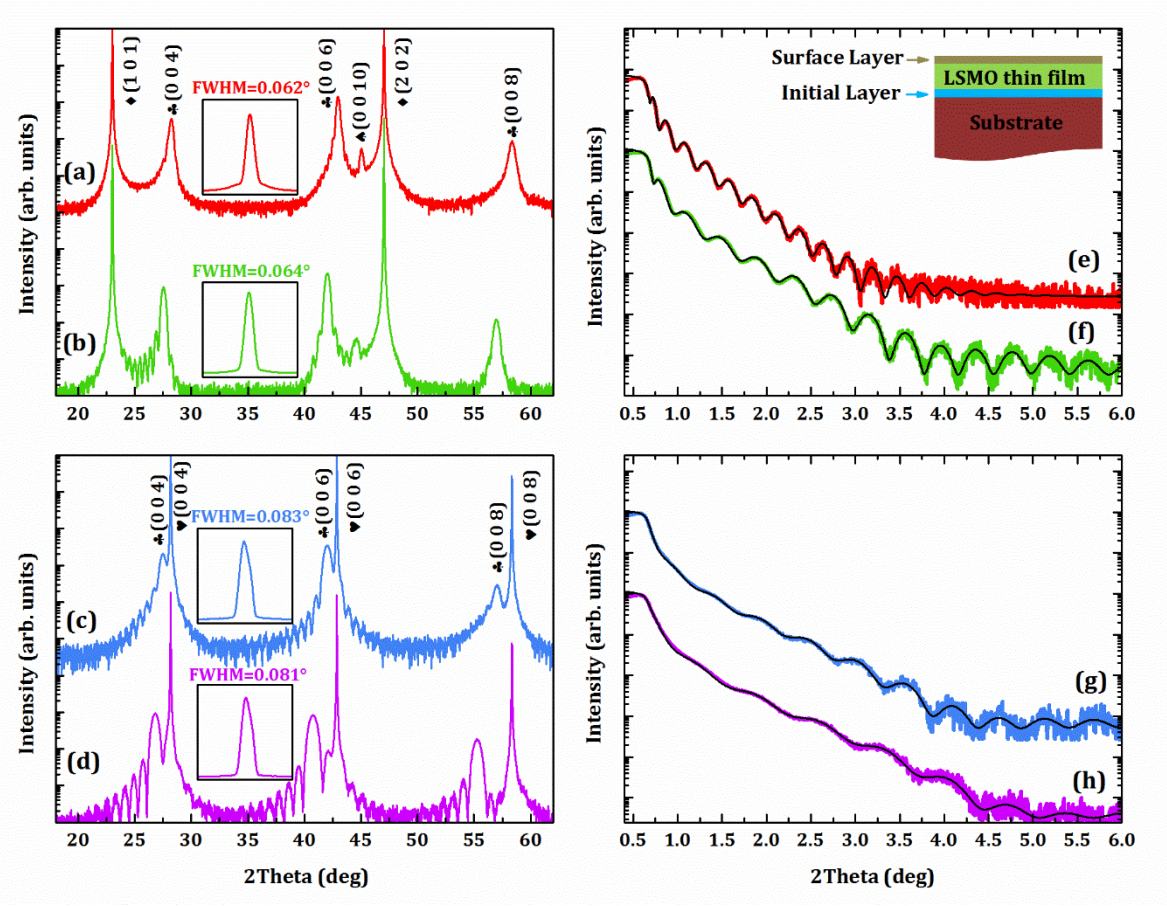

Figure 50: X-ray diffraction pattern of epitaxial $La_{1-x}Sr_{1+x}MnO_4$ (a) x=0.5; (b) x=0.0 thin films deposited on (1 0 1) NGO substrate and (c) x=0.5; (d) x=0.0 on (0 0 1) LSAO substrate. Reflections assigned with ♦, ♥, ♣ and ♠ correspond to NGO substrate, LSAO substrate, $La_{1-x}Sr_{1+x}MnO_4$ phase and $La_{2-2x}Sr_{1+2x}Mn_2O_7$ phase, respectively. X-ray reflectivity of $La_{1-x}Sr_{1+x}MnO_4$ (e) x=0.5; (f) x=0.0 thin films deposited on (1 0 1) NGO substrate and (g) x=0.5; (h) x=0.0 on LSAO substrate. The fitted curves are shown in black narrow lines.

In fact, no second phase has been detected for any thin film deposited on LSAO substrate. The reason could be the similar structure (single-layered Ruddlesden-popper, tetragonal, $I4/mmm$) which both LSAO and $La_{1-x}Sr_{1+x}MnO_4$ crystallize. In the XRD pattern, the amplitude and the number of Laue fringes are different for the four films due to the different thicknesses. Based on the rocking curve measurements, the mosaicity is higher for the films on LSAO substrate comparing to the one on the NGO substrate (see inset of Figure 50c-d). It has to be mentioned that the crystal quality of NGO substrates were better than the LSAO substrates. In fact, before the film growth, the LSAO substrate had to be annealed in oxygen atmosphere for an hour at 350 °C in order to remove the absorbents and hydroxides. The low crystal quality of LSAO substrate led to the growth of the films with higher mosaicity.

Table VI: Density and thickness of initial (I), film (F) and surface (S) layers of $La_{1-x}Sr_{1+x}MnO_4$ (x=0.0, 0.5) evaluated out of fitting the XRR curves.

Sample	d (nm) *(I)*	ρ (g/cm^3) *(I)*	d (nm) *(F)*	ρ (g/cm^3) *(F)*	d (nm) *(S)*	ρ (g/cm^3) *(S)*
x=0.0 on LSAO	1.0(7)	6.7(2)	9.5(4)	6.2(4)	1.7(5)	5.8(7)
x=0.0 on NGO	0.6(8)	8.7(7)	18.2(6)	6.1(7)	2.3(7)	5.1(0)
x=0.5 on LSAO	1.3(0)	7.3(0)	13.4(6)	5.9(4)	1.9(9)	5.0(7)
x=0.5 on NGO	1.9(1)	6.2(8)	28.0(8)	5.7(3)	1.1(1)	4.9(2)

Fitting XRR curves suggests that the films are triple-layered. Density and thickness of the three layers are evaluated and tabulated in Table VI. While in the films on NGO (section 3.4) with the thickness of 30 nm, the initial layer had a constant density of around 8.5 g/cm^3, here the density of initial layer varies from 6.2 to 8.7 g/cm^3. The reasons could be due to having four different interfaces. Similar to the previous study (section 3.4), the density of the surface layer is dissimilar to the film. Moreover, the thickness of the surface layer does not exceed 2 nm.

Table VII: Thickness of middle layer of $La_{1-x}Sr_{1+x}MnO_4$ (x=0.0, 0.5) films deposited on (1 0 1) NGO and (0 0 1) LSAO substrates evaluated out of fitting the XRR curves and calculation out of Laue fringes.

Sample	d (nm) *film* XRR	d (nm) *film* Laue fringes
x=0.0 on LSAO	9.5(4)	10.6(4)
x=0.0 on NGO	18.2(6)	18.7(9)
x=0.5 on LSAO	13.4(6)	14.0(5)
x=0.5 on NGO	28.0(8)	28.6(5)

At the first glace on the densities of the triple layers, a gradient from interface to the surface can be seen. Furthermore, the evaluated film thicknesses (middle layer) from XRR fitting agree quite well with the ones from Laue fringes (Table VII) similar to the ones presented in section 3.4.

The thickness of the films is below 30 nm; hence it is expected that they are fully strained. In order to investigate the epitaxial relation between films and substrates, the RSM on $La_{1-x}Sr_{1+x}MnO_4$ films (x=0.0, 0.5) on LSAO and NGO substrates were performed which are represented in Figure 51 and Figure 52, respectively.

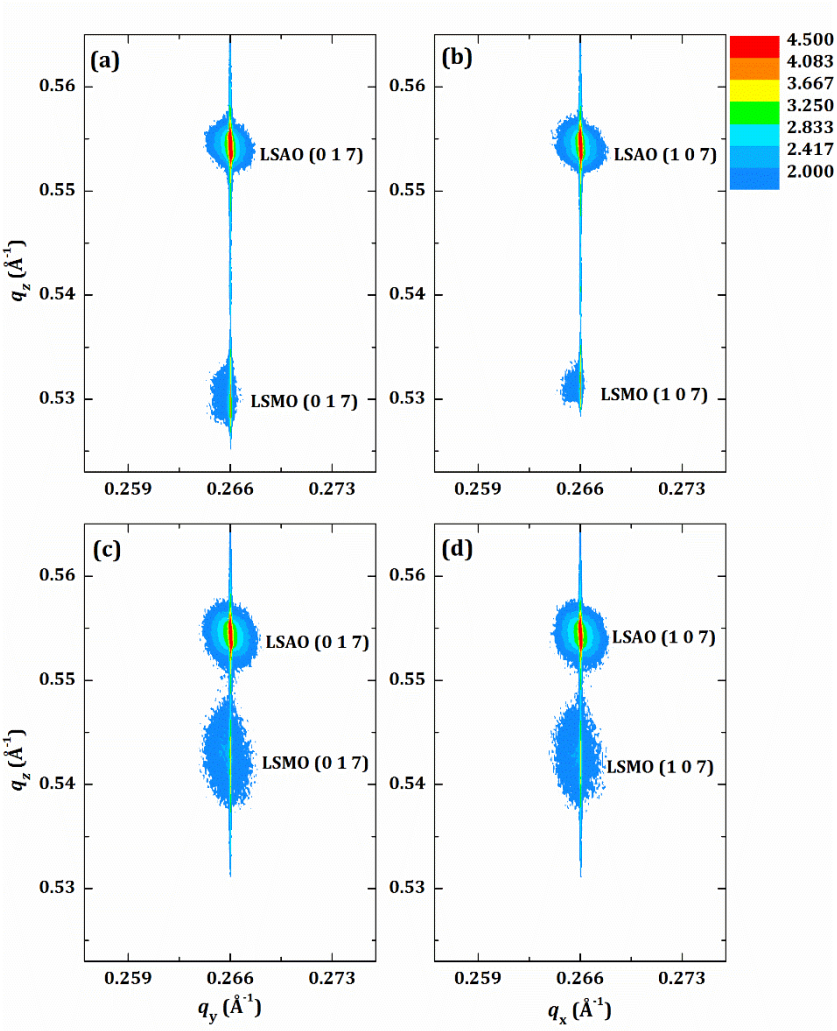

Figure 51: Reciprocal space mapping of (0 1 7) asymmetric reflection of $La_{1-x}Sr_{1+x}MnO_4$ (a) x=0.0 and (c) x=0.5 and (1 0 7) asymmetric reflection of (b) x=0.0 and (d) x=0.5 thin film on (0 0 1) LSAO substrate. Intensity is in logarithmic scale. The range of q_z in all four maps is the same in order to ease the comparison.

All four films are strained as the q_x/q_y of the film and the substrate in each case are identical. For $La_{1-x}Sr_{1+x}MnO_4$ films (x =0.0, 0.5) on LSAO substrate, the RSMs were performed on (1 0 7) or (0 1 7) asymmetric reflections of the film which are in the vicinity of same reflections of LSAO substrate. For each sample, RSMs were performed along two perpendicular in-plane directions. This was achieved by rotating the sample for 90° around normal axis. In this way, the in-plane lattice constants (a, b) can be evaluated. The a and b lattice constants of the films on LSAO substrate (Figure 51a-b or Figure 51c-d) are identical indicating the fact that the tetragonality is conserved for these films. The c lattice constant of $La_{1-x}Sr_{1+x}MnO_4$ (x=0.0) is much bigger than $La_{1-x}Sr_{1+x}MnO_4$ (x=0.5) as in corresponding RSMs, the q_z of the film appears farther from substrate. The lines which are extended vertically connecting the reflections of the film and the substrate are the result of using relatively wide slits. The wide slits were used in order to increase the intensity of the asymmetric reflections of the films.

Same RSM measurements were performed on $La_{1-x}Sr_{1+x}MnO_4$ films (x =0.0, 0.5) deposited on NGO substrates which are presented in Figure 52. Here, the (1 0 9) or (0 1 9) reflections of $La_{1-x}Sr_{1+x}MnO_4$ (x =0.0, 0.5) are in the vicinity of (3 2 3) reflection of NGO substrate. As it is demonstrated, the epitaxial relation of in-plane lattice constants of the film and the substrate is confirmed.

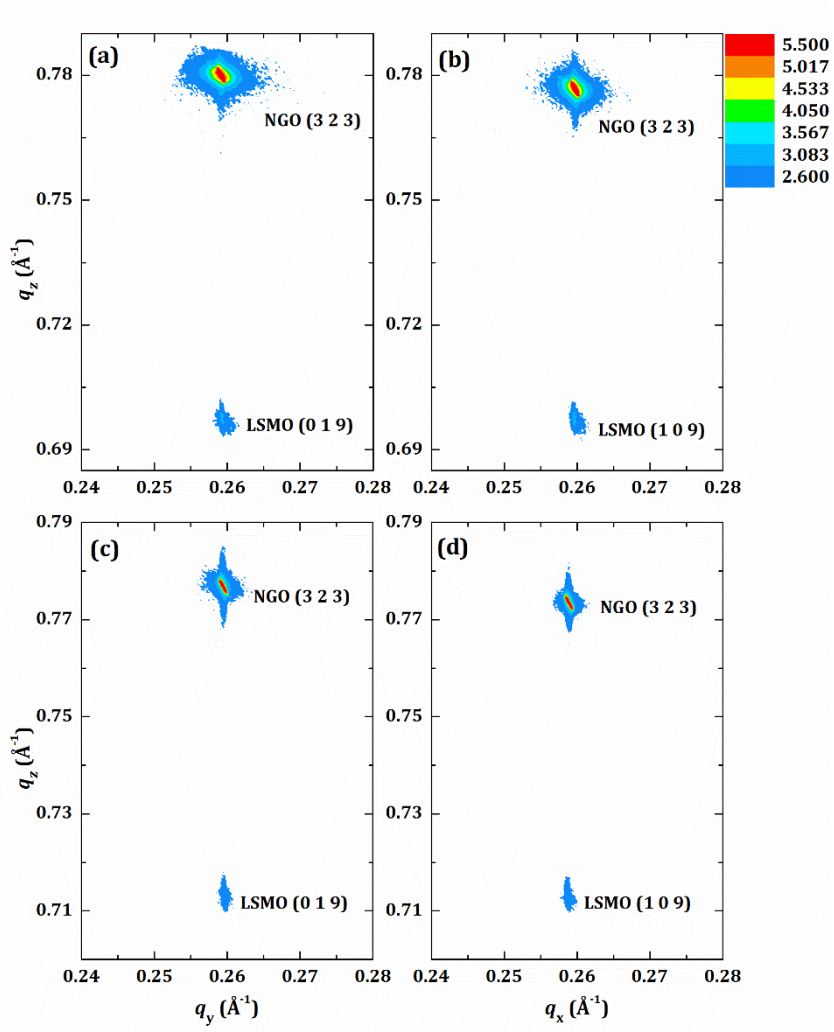

Figure 52: Reciprocal space mapping of (0 1 9) asymmetric reflection of $La_{1-x}Sr_{1+x}MnO_4$ (a) x=0.0 and (c) x=0.5 and (1 0 9) asymmetric reflection of (b) x=0.0 and (d) x=0.5 thin film on (1 0 1) NGO substrate. Intensity of reflections is in logarithmic scale. Note that q_z axis of counter graphs related to each compound scaled similar in order to ease the comparison.

Lattice parameters using equations (9)-(11) are evaluated and listed in Table VIII. Since $La_{1-x}Sr_{1+x}MnO_4$ crystallizes in a tetragonal structure, equation (11) is applicable for both q_x and q_y. In-plane (ε_a) and out-of-plane (ε_c) strains are evaluated using the bulk values of a and c lattice constants as 3.786 and 13.136 Å for $La_{1-x}Sr_{1+x}MnO_4$ (x=0.0) and 3.861 and 12.426 Å for $La_{1-x}Sr_{1+x}MnO_4$ (x=0.5), respectively [32].

Negative (positive) value of ε_a represents a compressive (tensile) in-plane strain. Analogues to in-plane strain, negative (positive) value of ε_c represents a(n) elongation (suppression) of out-of-plane lattice constant.

The unit cell volume is not conserved. While the unit cell volume of the films on LSAO is smaller than the bulk, the films grown on NGO substrate show a bigger unit cell volume than the bulk. The Poisson ratio υ as defined in first approximation by the ratio of the in-plane strain divided by the out-of-plane strain gives typical values of υ = 0.27 for (x=0.0) and υ = 0.20 for (x=0.5). Since the strain in out-of-plane comparing to in-plane lattice is more significant, c/a ratio follows the strain in c lattice. Therefore, c/a ratio (shown with arrows next to c/a ratio in Table VIII) increases with elongation of out-of-plane lattice constant (3.477 and 3.218 for x=0.0 and 0.5, respectively).

Table VIII: Lattice constants of $La_{1-x}Sr_{1+x}MnO_4$ (x=0.0, 0.5) films deposited on (0 0 1) LSAO and (1 0 1) NGO substrates evaluated from RSM measurements (Figure 51 and Figure 52) using equations (9)-(11). In-plane (ε_a) and out-of-plane (ε_c) strains along with deviation of unit cell volume are included.

Sample	a (Å)	ε_a	c (Å)	ε_c	V (Å^3)	ΔV (Å^3)	c/a
x=0.0 on LSAO	3.759	-0.71	13.219	0.43	186.79	-1.89	3.517 ↑
x=0.0 on NGO	3.851	1.72	12.902	-1.98	191.34	2.66	3.350 ↓
x=0.5 on LSAO	3.759	-2.64	12.903	3.84	182.32	-2.92	3.433 ↑
x=0.5 on NGO	3.865	0.1	12.613	1.50	188.42	3.18	3.262 ↑

Regarding almost equal in-plane lattice constants of $La_{1-x}Sr_{1+x}MnO_4$ (x=0.5) and NGO substrate, very small in-plane strain (0.1) generates which is negligible and can be considered as the film with almost no in-plane strain. However, out-of-plane lattice constant changes comparatively large and leads to a deviation in unit cell volume up to 3.18 Å^3. Tetragonal distortion for the films grown on the substrate with almost no in-plane strain has been reported before [109].

4. Analyses of Thin Film Composition by X-ray Photoelectron Spectroscopy

In this chapter, the fundamentals of X-ray Photoelectron Spectroscopy (XPS) and the experimental details of XPS measurements will be presented briefly. Following, characterization of thin films by XPS in order to investigate the effect of laser fluence on the films composition will be discussed. The study of characterization of strained engineered $La_{1-x}Sr_{1+x}MnO_4$ (x=0.0, 0.5) thin films by XPS will be the final pat of this chapter.

4.1. Principles of X-ray Photoelectron Spectroscopy

This section is written based on Ref. [110-113]. In XPS, the sample is irradiated using soft x-rays[11] such as Al $K\alpha$ (1487.6 eV) or Mg $K\alpha$ (1253.6 eV) sources. The *photo-electric effect*, the interaction of x-ray with core level electrons, leads to photoionization, *i.e.* excitation of electrons and generation of holes in the core shell. Thus, a system containing N electrons in the initial state will be left with N-1 electrons and a hole after excitation of one photoelectron (final state). If the interaction of photoelectron with the ionized system is negligible, the kinetic energy of the photoelectron can be derived as $E_K = h\nu - (E_B + \Phi)$ where $h\nu$, E_B, and Φ are the energy of incoming x-ray, the binding energy of the excited electron and the work function of the material (Figure 53).

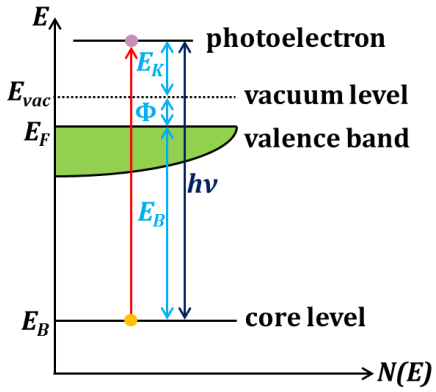

Figure 53: Representation of photoionization process in schematic band structure where E_B, E_F, E_{vac}, Φ, and E_K are the binding energy, the Fermi energy, the energy at the vacuum, the material work function and the kinetic energy of photoelectron.

The binding energy can be considered as the difference between the initial and final states. Hence, the unique XPS spectrum of each element can be used for identification of the composition of the sample.

[11] X-rays with photon energies of more than 5-10 KeV are called hard x-rays, while x-rays with lower energies are known as soft x-rays.

XPS could be described with a three-step model which consists of 1) the excitation of an electron, 2) the propagation of the excited electron in the solid, and 3) escape of excited electron from the solid to vacuum. For the first step, the probability of excitation of an electron is measured by photoexcitation cross-section (σ). For the second step, inelastic mean free path (IMFP) is defined as an index which accounts how far an electron can propagate through the solid. The IMFP of most of core shell electrons is restricted by less than 5 nm which makes XPS a surface sensitive technique.

When the interaction between photoelectron and the ionized system is not negligible which is true in most cases, many additional phenomena should be regarded. The Auger lines, the shake-up lines, the plasmons and the multiplet spitting are some of these phenomena.

The generated core hole can recombine with an outer electron and the recombination energy can be transferred *e.g.* to an electron in another shell. As a result, this electron will be excited to the vacuum known as the Auger electron.

Photoionization process leaves the system in an excited final state which is different from the ground state. Such system deals with the next photoelectron excitation process differently in which the core hole pulls the valence electrons to the Fermi level. Therefore, the photoelectrons will have a lower kinetic energy, *i.e.* higher binding energy which can be identified in the spectrum as the shake-up or satellite lines.

When a core hole after photoionization is created, the unpaired electrons in core shell (especially in transition metals) can couple with the unpaired electrons in the valence shell. These couplings lead to appearance of several final states in the XPS spectra known as multiplet splitting.

The valence electrons can be studied using XPS since the valence band spectra conveys the information of Fermi level and chemical band hybridization.

4.2. X-ray Photoelectron Spectroscopy Measurement Setup

In this study, the XPS measurements were performed with a PHI VersaProbe 5000 spectrometer using monochromatic Al *K*α (hν = 1486.6 eV) and Mg *K*α (hν = 1253.6 eV) radiation with pass energy of 23.5 eV. The resolution of XPS was 0.3 eV where calibration of energy was conducted using standard silver probe.

In order to prevent charging on the surface of the samples during XPS measurements, an integrated argon ion neutralizer was used. Charge neutralization was being monitored by C1s peak for the adventitious carbon at 284.8 eV [113]. XPS measurements were performed at 20, 45, and 75° as the angle between the surface of the sample and the axis of photoelectron detector. The XPS spectra were analyzed using XPSPEAK 4.1 software after background subtraction using Tougaard method. Shape of the characteristic peaks in all spectra was

considered symmetric with a combination of 30% Lorentzian-Gaussian profile, while shape of shake-up and plasmons lines was regarded as Gaussian. Photoelectron lines have a Lorentzian shape due to the hole core lifetime. The Gaussian profile has to be accounted according to the resolution of photoelectron detector.

4.3. The Effect of Laser Fluence on the Thin Film Composition

One the most important parameters in controlling deposition process in PLD is the adjustment of laser fluence. In a multi cation system like $La_{1-x}Sr_{1+x}MnO_4$, due to different ablation rate of different elements, a selective ablation may occur. Thus, finding an optimum laser fluence in order to have a stoichiometric transfer from target to substrate is very important. To gain a clear insight on the optimum laser fluence, thin films deposited using various laser fluences were measured by XPS using monochromatic Al *Kα* radiation at the angle of 45°. High resolution XPS spectra of the $La_{1-x}Sr_{1+x}MnO_4$ (x=0.0) thin film deposited on (1 0 1) NGO with various laser fluences (deposition temperature and pressure kept constant at 850 °C and 200 mTorr, respectively) are shown in Figure 54. In La-3*d* spectrum, due to spin-orbit splitting[12], La-$3d_{5/2}$ and La-$3d_{3/2}$ peaks can be observed. In the photoionization of the 3*d* core level of La, two final-states I ($3d^1$, $4f^0$) and II ($3d^1$, $4f^1$) occur where state II is the result of transfer of a valence electron of O-2*p* to La-4*f* empty shell (with charge transfer) [114]. Here, in the shown spectrum (Figure 54a), the two final-state components I and II of La-$3d_{5/2}$ appear at 833.1 and 837.5 eV, respectively.

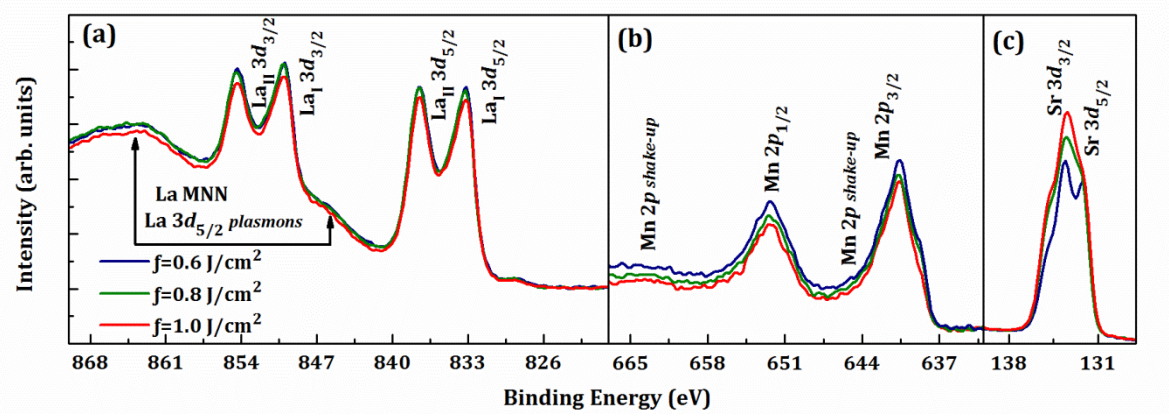

Figure 54: High resolution x-ray photoelectron spectroscopy (XPS) spectra of (a) La-3*d*, (b) Mn-2*p*, and (c) Sr-3*d* measured from $La_{1-x}Sr_{1+x}MnO_4$ (x=0.0) thin film deposited on (1 0 1) NGO substrate using various laser fluences (ƒ). XPS measurements were performed at the angle of 45° as the angle between thin film surface and photoelectron detector.

[12] The two possible states for the *p*, *d* and *f* orbitals which are separated by their corresponding energies.

Energy loss of free electron gas of La during photoionization process causes plasmons energy loss structure lines in the La-3*d* spectrum. Using Al x-ray source, the kinetic energy of plasmons and La Auger $M_{4,5}N_{4.5}N_{4,5}$ electrons (La-MNN) are quite similar. Therefore, the superimposed lines could not be distinguished easily.

Mn-2*p* spectrum splits into Mn-2$p_{3/2}$ and Mn-2$p_{1/2}$ peaks due to spin-orbit splitting. The common shake-up lines are detected as well. In this case, two shake-up lines in Mn-2*p* spectrum were identified.

Sr-3d spectrum involves two sets of Sr-3$d_{5/2}$ and Sr-3$d_{3/2}$ peaks which will be discussed later in details.

At the first glance, both shape and energy position of peaks in La-3*d* and Mn-2*p* for all three spectra are similar. In contrast, different fluences change the shape of Sr-3*d* spectra, drastically. Thus, it indicates that changing fluence actually changes the essence of Sr bonding, *i.e.* chemical environment, while no such effect can be seen for La-3*d* or Mn-2*p* spectra.

The XPS spectrum displays the number of excited electrons versus electron binding energy. Hence, the integrated area of XPS spectrum of each element is proportional to its corresponding atomic content. For all three elements, intensity of spectra scales up or down with laser fluence. The spectra of La-3*d* and Mn-2*p* decreases with fluence, while the spectra of Sr-3*d* increases. This signifies that higher fluences lead to ablation of more Sr and less La and Mn.

In order to obtain a better understanding on elemental ratio, the foreshown spectra were fitted using XPSPEAK 4.1 software [115].

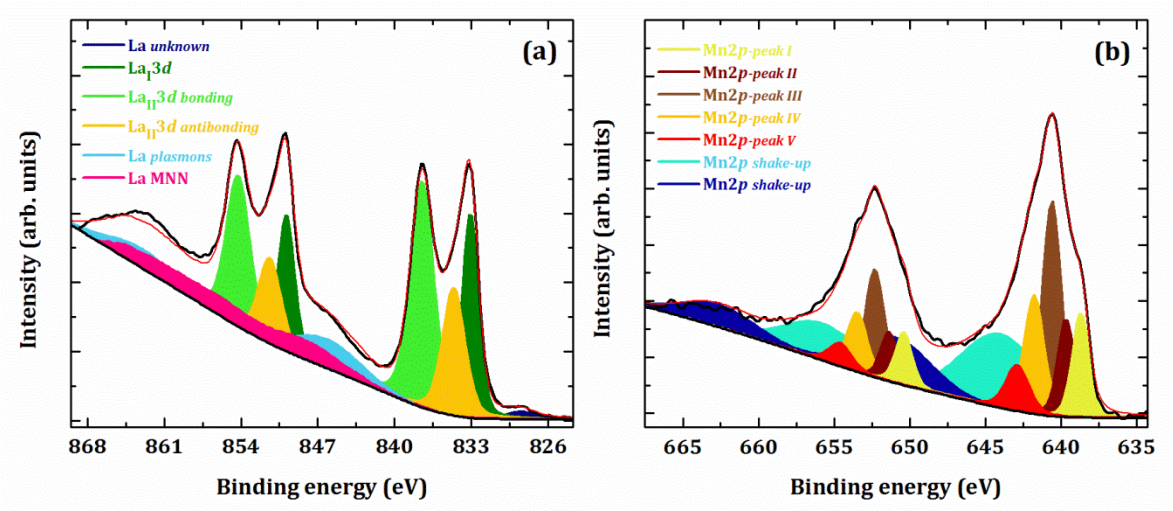

Figure 55: High resolution XPS spectra of (a) La-3*d*; (b) Mn-2*p* of $La_{1-x}Sr_{1+x}MnO_4$ (x=0.0) thin film deposited on NGO (1 0 1) substrate using laser fluence of 0.6 J/cm². Measured spectra and Tougaard background are illustrated with black lines. The sum of fitted peaks is shown with red line

Since the shape of La-3*d* and Mn-2*p* spectra were similar for different samples, here only the results of fitting the spectra of the film deposited using laser fluence of 0.6 J/cm^2 is presented (Figure 55).

To separate the La-MNN and La-3*d* peaks, a method suggested by Ref. [116] was followed and La-MNN and La-3*d* peaks were measured using Mg x-ray ($h\nu$ = 1253.6 eV) radiation. In this way, La-MNN peak shifts to lower energies and eventually separates from La-3*d* peak. Now kinetic energy of La-MNN and La-3*d* electrons are different. Therefore, these spectra should be normalized to the inelastic mean free of corresponding photoelectrons. Consequently, the ratio of La-MNN and La-3*d* measured by Mg x-ray source can be employed to the overlapped spectra measured by Al x-ray source. The details on subtraction of La-MNN from La-3*d* peak can be found in Appendix I.

The spin-orbit splitting energy gap of La-3*d* is considered to be 16.78 eV [113]. In Figure 55a, the final-state II of La-3*d* (La_{II}-3*d*) (with charge transfer) consists of bonding and antibonding counterparts where the antibonding peak has lower binding energy [116].

The energy difference of La-3*d* plasmons peaks was also set to be 16.78 eV. The plasmons peak appears with the energy difference of 13.09 eV from La_I-3$d_{5/2}$ peak. There is an unknown peak of La at binding energy of 828.5 eV which will be discussed later. The binding energy, FWHM and integrated area of each peak are listed in Table IX.

Table IX: La-3*d* and Mn-2*p* spectral fitting parameters: binding energy, spectral area percentage, FWHM.

Peak	Binding energy (eV)	Area (%)	FWHM (eV)
La unknown	828.5	1.0	3.3
La_I-3*d*	833.1	24.7	1.7
La_{II}-3*d antibonding*	834.6	21.5	2.4
La_{II}-3*d bonding*	837.5	39.8	2.5
La-3*d plasmons*	846.2	12.9	7.3
Mn-2*p peak I*	638.7	9.4	1.3
Mn-2*p peak II*	639.7	8.8	1.3
Mn-2*p peak III*	640.6	21.5	1.5
Mn-2*p peak IV*	641.8	12.6	1.5
Mn-2*p peak V*	642.9	5.7	1.8
Mn-2*p shake-up I*	644.0	26.6	6.0
Mn-2*p shake-up II*	651.0	15.3	5.6

Analysis of 2*p* spectra of the 3*d* transition metals and their oxides is complicated due to occurrence of peak asymmetries, complex multiplet splitting, shake-up and plasmon loss structures. Considering these facts, the Mn-2*p* peaks were fitted following the method suggested by Ref. [117]. The fitting parameters are listed in Table IX as well.

The Mn-2*p* can be fitted using five peaks with FWHM ranging from 1.3 to 1.8 eV. Two shake-up lines were found at the energies of 4.1 and 10.9 eV higher than energy of Mn-2*p* main peak (Mn-2*p* peak III).

In contrast with the similar XPS spectra of La-3*d* and Mn-2*p* in films deposited using different laser fluence, as it was mentioned before, Sr-3*d* spectra changes considerably with laser fluence. The Sr-3*d* spectra of the films deposited using 0.6, 0.8 and 1 J\cm^2 are presented in Figure 56. As it can be seen, the spectra evolve two Sr-3*d* peaks at different binding energies.

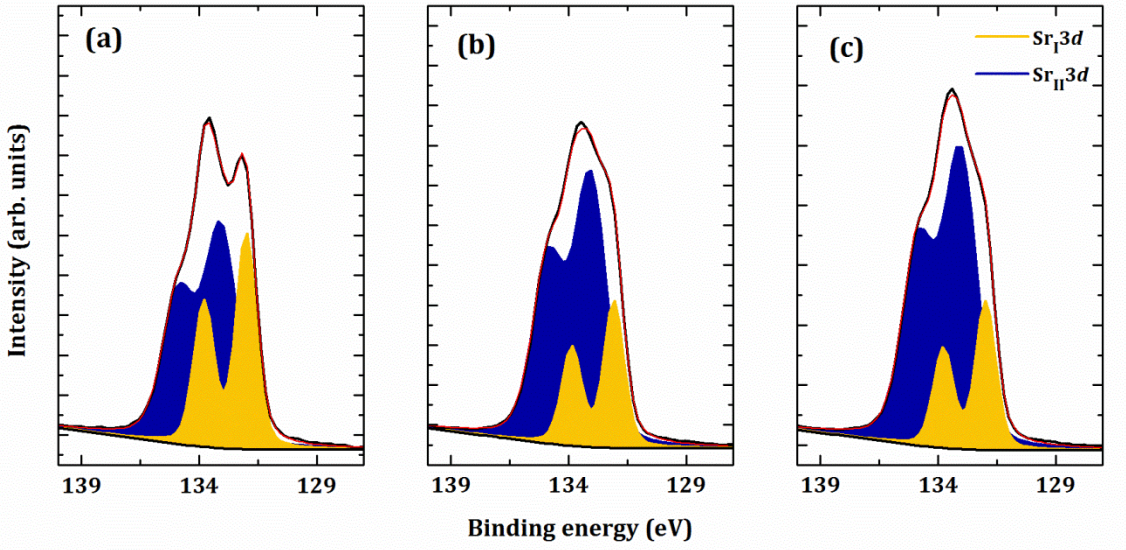

Figure 56: High resolution XPS spectra of Sr3*d* of $La_{1-x}Sr_{1+x}MnO_4$ (x=0.0) thin film deposited on NGO (1 0 1) substrate using laser fluence of (a) 0.6: (b) 0.8, and (c) 1 J\cm^2.

The portion of Sr-3*d* peak with lower binding energy (*peak I*) decreases with applied laser fluence. The fitting parameters of the shown spectra are listed in Table X. The binding energies of Sr-3*d* peaks (132.0 and 133.1) are identical for the three samples. Furthermore, the FWHM width of *peak I* and *peak II* are 1.0 and 1.6 eV, respectively, for all three samples. The only difference is the ratio of these peaks. Presence of two peaks indicates two different Sr-O bonds where the *peak II* has been attributed to SrO compound and *peak I* originates from Sr-O bond in the $La_{1-x}Sr_{1+x}MnO_4$ structure [118].

Table X: Spectral fitting parameters of Sr-3*d* spectra: binding energy, spectral area percentage and FWHM.

Laser fluence (J/cm^2)	Peak	Binding energy (eV)	Area (%)	FWHM (eV)	$\frac{Sr3d\ II}{Sr3d\ I}$
0.6	Sr-3*d peak I*	132.0	38.3	1.0	1.6
	Sr-3*d peak II*	133.1	61.7	1.6	
0.8	Sr-3*d peak I*	132.0	25.6	1.0	2.9
	Sr-3*d peak II*	133.1	74.4	1.6	
1.0	Sr-3*d peak I*	132.0	23.8	1.0	3.2
	Sr-3*d peak II*	133.1	76.2	1.6	

Therefore, to obtain thin films with correct stoichiometry, the lower laser fluence is shown to be the proper choice. It is known that in manganites thin films, strontium segregates on the surface leading to formation of a Sr-rich phase [119-122]. Considering this fact, the ratio of *peak II* to *peak I* (Table X) shows that the significant amount of detected Sr-3*d* photoelectrons originates from Sr-rich phase. This may be originated from the fact that XPS is a surface sensitive tool. To clarify such possibility, the samples were measured at the angle of 20°. At this angle, the detectable photoelectrons are mostly excited from very top layers.

In Figure 57, the spectra of La-3*d*, Mn-2*p* and Sr-3*d* measured at two angles, namely 20° and 45° on the $La_{1-x}Sr_{1+x}MnO_4$ (x=0.0) thin film deposited on NGO (1 0 1) substrate using 1 J/cm^2 are presented. The intensities of the spectra recorded at 20° are two times smaller than the ones measured at 45° due to less probed mass, and hence, less photoelectron cross-section. There are two major differences between these two sets of measurements. First, at the angle of 20°, the unknown peak in La-3*d* spectrum is pronounced by the factor of three. Second, again at the angle of 20°, the portion of Sr-3*d peak II* is significantly increased. This supports the assumption of the presence of Sr-rich phase on the surface. Furthermore, it shows that the unknown peak of La-3*d* initiates from a second phase on the surface.

By calculating the area of high resolution XPS spectra of La-3*d*, Mn-2*p*, and Sr-3*d* and dividing to the corresponding atomic sensitivity factors, the stoichiometry of the studied thin films was evaluated and tabulated in Table XI. For this evaluation, the areas of the components in the spectra were considered as follows. For La-3*d*, the area of La unknown peak and La-MNN peak were disregarded, while the whole area of Mn-2*p* spectrum was considered. For Sr-3*d*, the area of *peak I* was taken only, since *peak II* originates from Sr-rich surface phase.

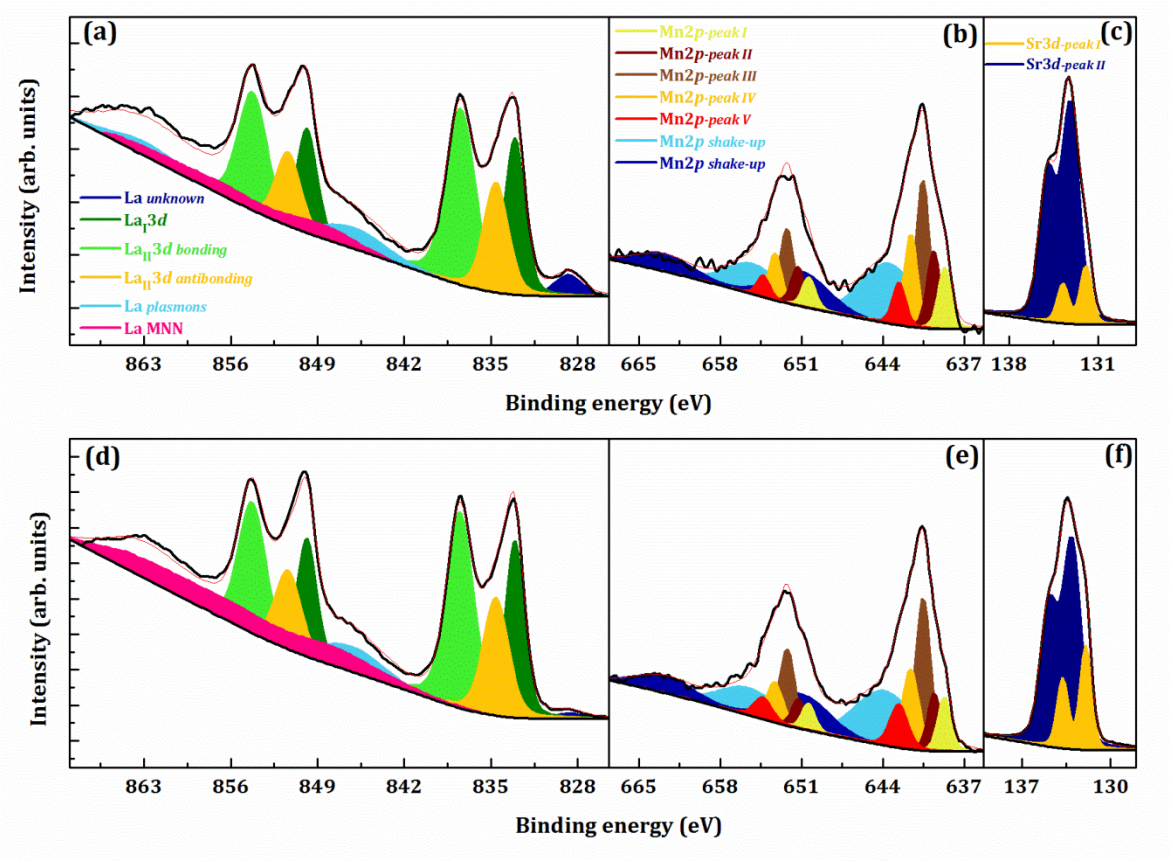

Figure 57: Angle-resolved XPS spectra of (a, d) La-3*d*, (b, e) Mn-2*p*, and (c, e) Sr-3*d* of the $La_{1-x}Sr_{1+x}MnO_4$ (x=0.0) thin film deposited on NGO (1 0 1) substrate using 1 J/cm² laser fluence. The first (second) row shows spectra measured at the angle of 20° (45°).

Using atomic sensitivity factors for qualitative analyses of XPS spectra produces uncertainties up to 10-15%. In Table XI, such error bar is included.

Table XI: Qualitative analyses of XPS spectra recorded for $La_{1-x}Sr_{1+x}MnO_4$ (x=0.0) thin films deposited at various laser fluences.

Laser fluence	La3*d* (%)	Sr3*d* (%)	Mn2*p* (%)	(La+Sr)/Mn	Sr/La
0.6 J/cm²	40 ± 4	32 ± 3	32 ± 3	2.6 ± 0.2	0.8 ± 0.1
0.8 J/cm²	44 ± 4	30 ± 3	26 ± 3	2.8 ± 0.3	0.6 ± 0.1
1.0 J/cm²	40 ± 4	32 ± 3	28 ± 3	2.6 ± 0.2	0.8 ± 0.1

The ratio of (La+Sr)/Mn for all three thin films is about 2.5 which indicates the presence of the extra amount of La and Sr. Moreover, the content of La and Sr is not equal. Even though the ratio of Sr/La is always less than 1, the thin films could be considered as $La_{1-x}Sr_{1+x}MnO_4$ (x=0.0) with some extra amount of La and Sr oxides. The reason for such claim is that the binding energy of Auger peaks of Mn (Mn-LMM) is 852 eV and hence there would be a

superimposition of this peak and La-3*d* spectrum. This means that part of the evaluated atomic percentage of La initiates from Mn-LMM peak.

As a conclusion, the composition of thin films deposited in the range of laser fluences which have been presented does not vary within the resolution of XPS. The true estimation of stoichiometry of films is very challenging due to following reasons:

- superimposition of La-MNN and Mn-LMM peaks with La-3*d*
- formation of La and Sr oxide on the surface during thin film growth
- 10-15% error in evaluation of stoichiometry using atomic sensitivity factor
- lack of information on precise values of inelastic mean free path of electron and cross-section of photoelectrons of each element along with charge carrier and Fermi level values for bulk and thin film of $La_{1-x}Sr_{1+x}MnO_4$ (x=0.0, 0.5)

As it was mentioned before, the above study shows that using lower laser fluences (like 0.6 J/cm^2) leads to elimination of formation of Sr-rich phase on the surface. This result has been confirmed by angle-resolved XPS measurements which were presented.

4.4. XPS study on strained $La_{1-x}Sr_{1+x}MnO_4$ (x=0.0, 0.5) thin films

As it was mentioned before (section 1.2.2), doping $La_{1-x}Sr_{1+x}MnO_4$ (x=0.0, 0.5) with Sr changes the oxidation state of Mn, the lattice, charge and orbital degrees of freedom and affects the electronic and magnetic structures. In order to study the possible preferential orbital occupation of Mn atoms upon changing the doping level, it is vital to control La/Sr ratio. For this aim, the stoichiometry of $La_{1-x}Sr_{1+x}MnO_4$ (x=0.0, 0.5) films deposited on NGO and LSAO substrate[13] were investigated by XPS. In Figure 58, the XPS survey spectra of the films characterized by XRD techniques in section 3.5 are presented.

[13] The films were grown using laser fluence of 0.75 J/cm^2 at the deposition temperature and pressure of 850 °C and 200 mTorr, respectively.

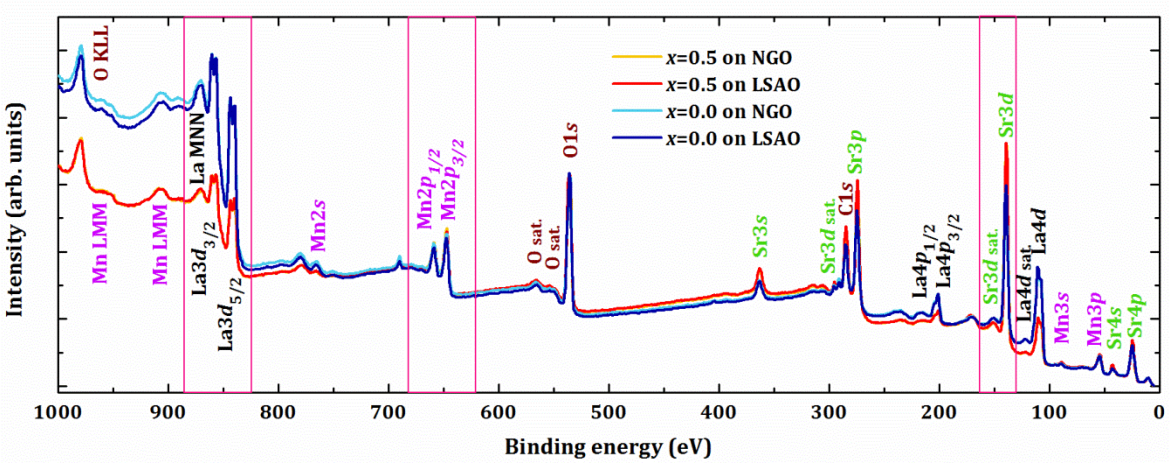

Figure 58: Survey XPS spectra of $La_{1-x}Sr_{1+x}MnO_4$ (x=0.0, 0.5) thin films deposited on (1 0 1) NGO and (0 0 1) LSAO substrates. The regions marked with pink boxes show La-3*d*, Mn-2*p* and Sr-3*d* spectra.

The peaks corresponding to La, Sr and Mn along with the ones related to O and C are marked in the graph. The spectra of $La_{1-x}Sr_{1+x}MnO_4$ (x=0.5) on LSAO and NGO are overlapped, thus the minute differences cannot be distinguished. Similarly, the spectra of $La_{1-x}Sr_{1+x}MnO_4$ (x=0.0) are quite similar at binding energies less than 850 eV. At higher binding energies, the one on NGO has a higher intensity. The intensity of La peaks of $La_{1-x}Sr_{1+x}MnO_4$ (x=0.0) films in the whole spectrum is higher than the ones of $La_{1-x}Sr_{1+x}MnO_4$ (x=0.5), since La/Sr ratio for the former is 1 while for the latter is 0.33. Similarly, the intensity of Sr peaks of $La_{1-x}Sr_{1+x}MnO_4$ (x=0.0) films is lower than the ones belonging to $La_{1-x}Sr_{1+x}MnO_4$ (x=0.5) films. Note that in Figure 58, the regions of La-3*d*, Sr-3*d* and Mn-2*p* are marked with the boxes. On the other hand, the intensity of the peaks corresponding to Mn are similar for all four thin films due to identical atomic percentage of Mn in both $La_{1-x}Sr_{1+x}MnO_4$ (x=0.0, 0.5) compounds.

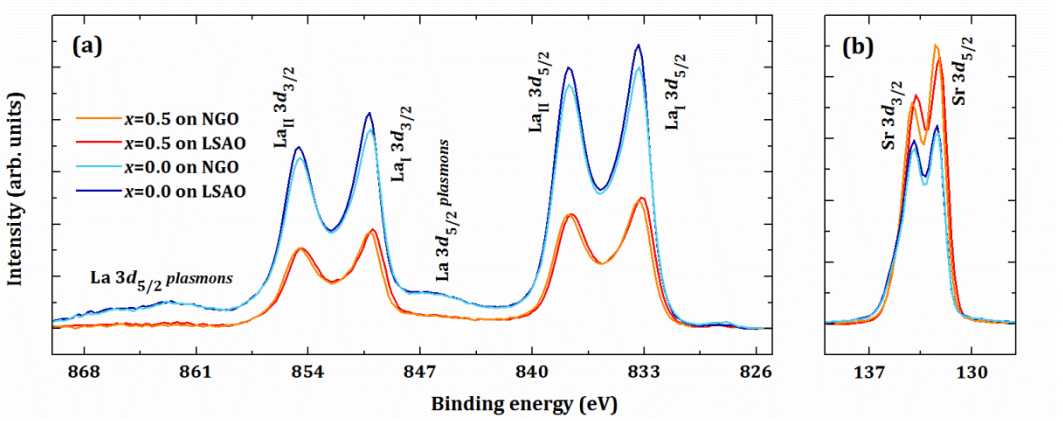

Figure 59: High resolution XPS spectra of (a) La-3*d*; (b) Sr-3*d* of $La_{1-x}Sr_{1+x}MnO_4$ (x=0.0, 0.5) films deposited on (0 0 1) LSAO and (1 0 1) NGO substrates. The backgrounds of spectra are subtracted. In addition, the La-MNN peak was subtracted from La-3*d* spectra.

Having a closer look at La-3*d* and Sr-3*d* spectra in Figure 59, the aforementioned statements can be confirmed. The backgrounds of spectra are subtracted by Tougaard method in order to

ease the comparison. In addition, the La-MNN peak was subtracted from La-3*d* spectra. The binding energies of the peaks both at La-3*d* and Sr-3*d* for all four films are equal. The ratio of $\frac{La3d_{x=0.0}}{La3d_{x=0.5}}$ was calculated out of the area of the spectra and found to be 1.9, while the ratio of $\frac{Sr3d_{x=0.5}}{Sr3d_{x=0.0}}$ was evaluated as 2.8 which shows an offset of 0.1 and 0.2 for La and Sr, respectively. For this comparison, on one hand side, the whole area of La-3*d* spectra was regarded; and on the other hand side, only Sr-3*d* peak at binding energy of 132.1 eV was taken into account.

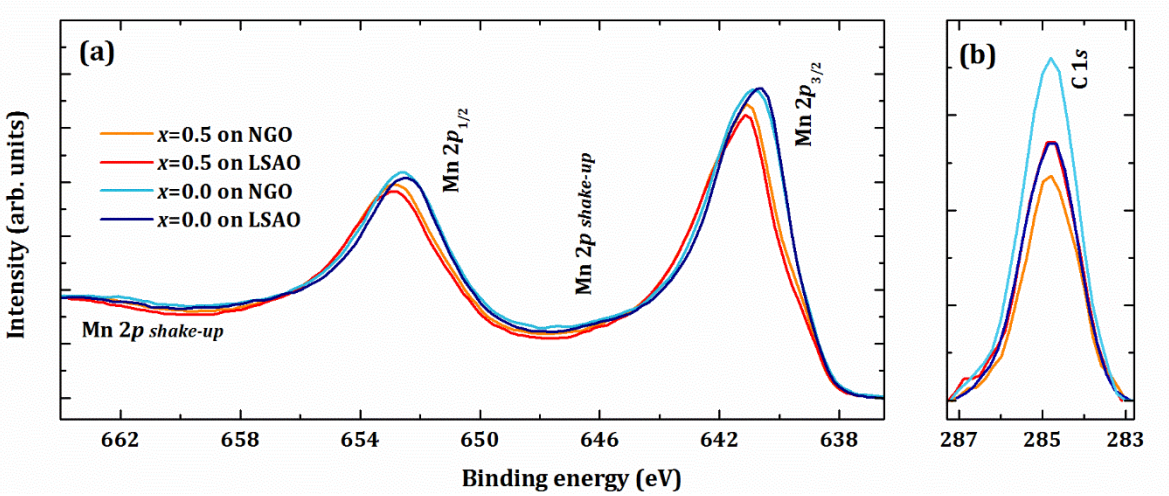

Figure 60: High resolution XPS spectra of (a) Mn-2*p* and (b) C-1*s* of $La_{1-x}Sr_{1+x}MnO_4$ (x=0.0, 0.5) thin films deposited on (1 0 1) NGO and (0 0 1) LSAO substrates. The spectra of Mn-2*p* are normalized to the edges, while the backgrounds of spectra of C 1*s* are subtracted.

High resolution XPS spectra of Mn-2*p* reveal that doping Sr in $La_{1-x}Sr_{1+x}MnO_4$ shifts the spectra of Mn-$2p_{3/2}$ and Mn-$2p_{1/2}$ about 0.5 eV to higher binding energies (Figure 60a). This shift is due to the difference in La/Sr ratio and consequently difference in valence state of Mn.

Although Mn-2*p* spectrum is not very sensitive to the valence state, the mixed valence states of Mn^{3+} and Mn^{4+} in $La_{1-x}Sr_{1+x}MnO_4$ (x=0.5) leads to the aforementioned shift. Note that the spectra of Mn-2*p* for the films with same La/Sr ratio are identical. Since such small shift may occur as a result of measurements errors, the spectra were calibrated with C 1*s* peak as usual. The spectra of C 1*s* peak of corresponding films are shown in Figure 60b.

The valence-band XPS spectra along with the spectra of O-1*s* are presented in Figure 61. The valence-band spectra normalized to the intensity at -2 eV. The spectra of films with similar La/Sr ratio are identical. However, altering La/Sr ratio changes the valence-band spectra in some aspects. First, the spectra of $La_{1-x}Sr_{1+x}MnO_4$ (x=0.5) shift towards Fermi level for about 0.2 eV. This shift is smaller than what has been observed in Mn-2*p* spectra. Second, the very weak band just below the Fermi level at 1 eV looks different for the films with different La/Sr ratios. This shoulder is attributed to e_g band [62, 123-126]. Doping $La_{1-x}Sr_{1+x}MnO_4$ with Sr squeezes e_g band shoulder as its width was evaluated as 1 and 0.5 eV for (x=0.0) and (x=0.5),

respectively. The evaluation of e_g band width was conducted using the transition points of the corresponding second derivatives. Third, the band located at 2 eV for $La_{1-x}Sr_{1+x}MnO_4$ (x=0.0) films smears out in comparison with the one of $La_{1-x}Sr_{1+x}MnO_4$ (x=0.5) films. This band is attributed to t_{2g} band [62, 123-125]. In undoped structure, *i.e.* $La_{1-x}Sr_{1+x}MnO_4$ (x=0.0), one electron in e_g band leads to the weak but relatively wide band at 1 eV. While, in half-doped structure, *i.e.* $La_{1-x}Sr_{1+x}MnO_4$ (x=0.5), the width of the band shrinks to 0.5 eV.

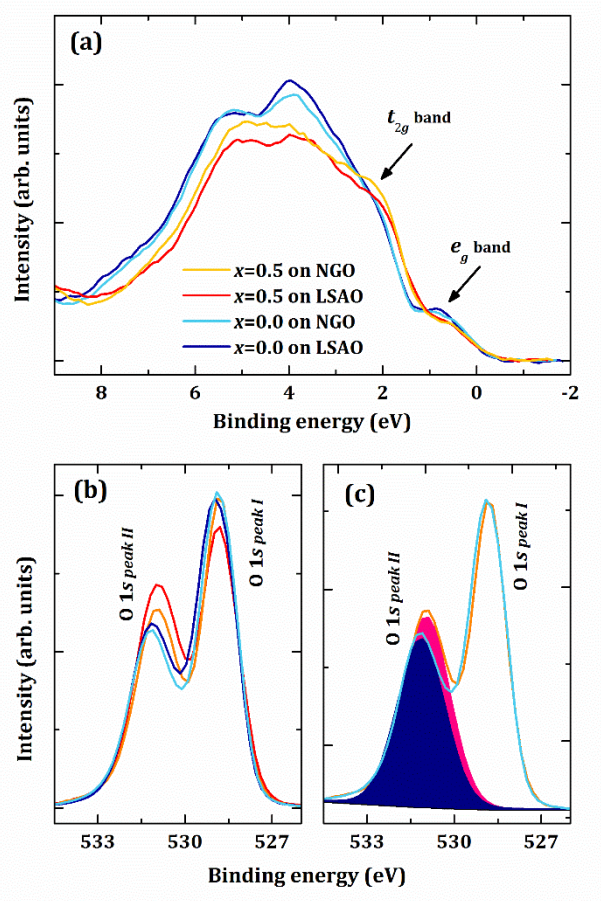

Figure 61: XPS spectra of (a) valence-band; (b) O-1*s* of $La_{1-x}Sr_{1+x}MnO_4$ (x=0.0, 0.5) thin films deposited on (1 0 1) NGO and (0 0 1) LSAO substrates. (c) Fitted O-1*s* spectra of $La_{1-x}Sr_{1+x}MnO_4$ (x=0.0, 0.5) on NGO substrate.

Furthermore, the spectra of O-1*s* (Figure 61b) show the convolution of two peaks where the peak at lower binding energy (*peak I*) is similar in term of binding energy for both compounds $La_{1-x}Sr_{1+x}MnO_4$ (x=0.0, 0.5). In contrast, the binding energy of the peak at higher end of spectra (*peak II*) shifts to lower energies for about 0.3 eV as the amount of Sr increases. The *peak I* can be assigned to the surface absorbent oxygen, while the *peak II* is corresponded to the oxygen atoms within the $La_{1-x}Sr_{1+x}MnO_4$ structure.

Fitting the O-1s spectra (Figure 61c) clearly shows the shift of *peak II* to lower binding energies for about 0.3 eV in $La_{1-x}Sr_{1+x}MnO_4$ (x=0.5) thin films. This shift is similar to what has been observed in valence-band spectra.

5. Orbital Occupation of Mn in $La_{1-x}Sr_{1+x}MnO_4$ (x=0.0, 0.5) thin films

In this chapter, the fundamentals of X-ray Absorption Spectroscopy (XAS) will be presented. Following the chapter, the details of XAS measurements will be presented. The linearly polarized XAS spectra reveal the effect of artificially generated strain on Mn-3*d* preferential orbital occupation will be discussed in the last section of this chapter. The first section covers the fundamental knowledge about the photo-electric effect. Hence, most of the subjects are valid for XPS measurements, as well.

5.1. Principles of X-ray Absorption Spectroscopy

This section is based on Ref. [127-131]. X-rays can be absorbed partly by matter. For each element, at a set of certain range of x-ray energies, the absorption is significantly high. When the energy of photon is equal to the excitation energy of the core level electrons, the photon will be absorbed showing a peak in absorption spectrum. The x-ray nomenclature for electron shells is used in XAS wherein the n = 1 shell is referred to as K-shell, n = 2 to as L-shell, n = 3 to as M-shell, etc. For example, XAS at the L edge is, in principle, the excitation of 2s or 2p core level electrons to the valence band. Due to spin-orbit coupling, the 2p band splits into two levels of energies with the total angular momentum of $j = \frac{3}{2}$ or $j = \frac{1}{2}$ whose transition to the valence band is called L_3 and L_2 edge, respectively.

XAS is usually a synchrotron based measurement. Similar to XPS, the XAS measurement is based on the photo-electric effect (section 4.1) in which the monochromated x-rays interact with the selected core level electrons (initial state) and the consequent excitation leaves a core-hole and an excited state behind (final state). As it is mentioned in section 4.1, this process is known as photoionization.

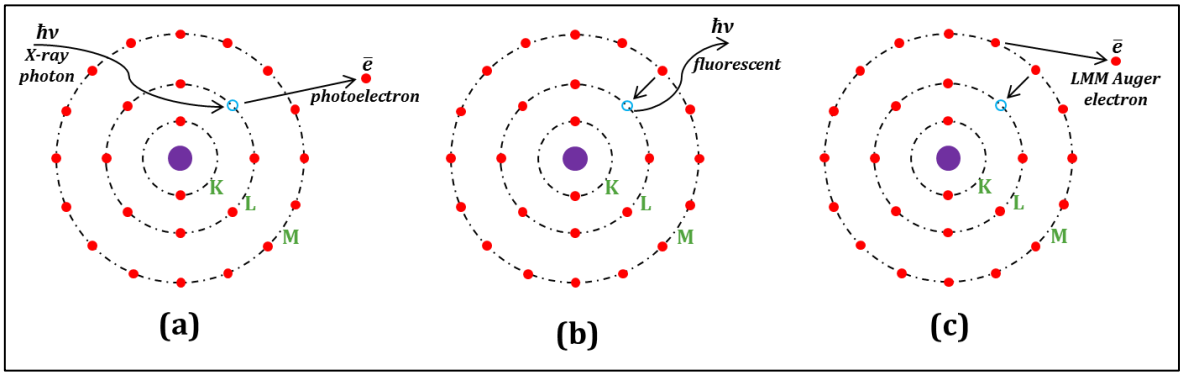

Figure 62: (a) Photoionization process where the incident photon is absorbed by the atom and a photoelectron, in this particular case from L shell, gains enough kinetic energy to leave the atom. (b) The left core-hole can be filled by an electron from another shell. The atom, then, either emits a characteristic photon known as fluorescence or; (c) another electron known as Auger electron.

The core-hole will be filled by another electron (screened electron) from an upper shell. Due to conservation of energy, the difference in energy levels of the excited electron and the screened electron will be compensated by either emitting a characteristic phonon (fluorescence) or emitting another electron from one of the upper shells (Auger electron) (Figure 62).

In an excited state, due to the strong overlap between the core and valence wave functions, the electron-electron interactions are important. This is the origin of atomic multiplet effect which can be described by the Schrödinger equation for the atomic-like system:

$$\boldsymbol{H} = \sum_{N} \frac{p_i^2}{2m} + \sum_{N} \frac{-Ze^2}{r_i} + \sum_{N} \zeta(r_i) l_i \cdot s_i + \sum_{i,\,j} \frac{e^2}{r_{i,\,j}} \qquad (12)$$

where the terms are, respectively, the kinetic energy of the electrons, the electrons-nucleus interactions, the spin-orbit coupling of each pair of electrons, and the electron-electron (electron-hole) interactions. The two first terms describe the given atomic configuration. The third term counts for the total spin-orbit coupling of each pair of electrons where $\boldsymbol{H}_{SO} = \frac{\mu_B}{\hbar m_e e c^2} \frac{1}{r} \frac{\partial U(r)}{\partial r} l \cdot s$ and $\zeta(r_i) = \frac{\mu_B}{\hbar m_e e c^2} \frac{1}{r} \frac{\partial U(r)}{\partial r}$. The last term sums all electron-electron interactions whose energy for the case of $2p$ - $3d$ electrons are quite remarkable. The excitons[14] should be regarded based on the possible electron-hole coupling. For example, Mn^{3+} in $La_{1-x}Sr_{1+x}MnO_4$ (x=0.0) has a $3d$ valence band filled with 4 electrons (d^4). Thus the initial and final states can be written as $2p^6\ 3d^4$ and $2p^5\ 3d^5$. In the final state, the one hole in $2p$ shell can reside in 6 different orbitals, while the photoelectron can reside in 10 different orbitals. Therefore, the other electrons in the $3d$ shell may rearrange in $\frac{10\times9\times8\times7\times6}{2\times3\times4\times5} = 252$ ways. Hence, $252 \times 6 = 1512$ possible final states can be imagined. By the help of term symbols[15] [132], 205 energetically possible final states can be derived. And finally, the number of final states will be reduced to 32 by regarding Hund's rules and of course the selection rules (Appendix II).

The system is somehow more complicated when the atom has a bond with a ligand which is the case for the oxides. For most of the perovskite oxides, and in particular for $La_{1-x}Sr_{1+x}MnO_4$, Mn atoms are surrounded with six oxygen atoms in the octahedral symmetry. This is where the symmetry plays a role and the system demands a proper model to be described. The crystal field multiplet model has been used successfully to explain a vast series of oxide materials.

[14] An exciton is an electrically neutral quasiparticle which is a bound state of an electron and a hole.

[15] The Russell-Saunders term symbol is an abbreviated description of the angular momentum quantum numbers in a multi-electron atom.

As it was stated before, the crystal field splitting in octahedral symmetry splits the *d* orbital to the triply degenerated t_{2g} and doubly degenerated e_g levels. The e_g - e_g, e_g - t_{2g} and t_{2g} - t_{2g} exchange interactions should be taken into account and added to atomic multiplet Hamiltonian. In Figure 63, the effect of crystal field splitting on Mn-$L_{2,3}$ edges is simulated by CTM4XAS software [133]. The spectra show several final states for $L_{2,3}$ edges of Mn where changing the crystal field splitting alters the energy and the intensity ratio of them and consequently changes the shape of the spectrum.

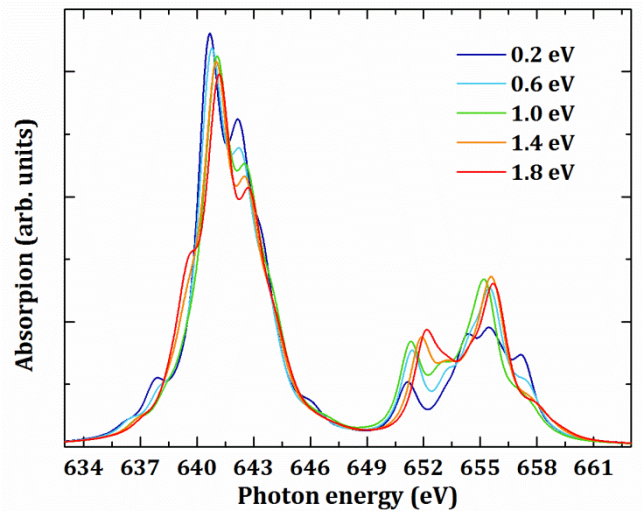

Figure 63: XAS simulation of Mn-$L_{2,3}$ edges considering different crystal field splitting from 0.2 – 1.8 eV. The atomic multiplet effect and spin-orbit coupling are taken into account and set fixed.

For the simulation, the 0.6 Lorentzian broadening was chosen. The shape of the absorption spectrum is Lorentzian due to the uncertainty in the energy based on finite lifetime of the core-hole.

The aforementioned interactions and coupling energies make the XAS spectra at $L_{2,3}$ edges quite complicated, but at the same time, they convey lots of information and will improve our understanding about the geometrical and electrical structure of the exposed matter.

As a reminder, in $La_{1-x}Sr_{1+x}MnO_4$ (x=0.0), Mn^{3+} $\left(t_{2g}^3 e_g^1\right)$, e_g electrons reside in $d_{3z^2-r^2}$ orbitals resulting in a Jahn-Teller distorted octahedra of MnO_6. Hence, the out-of-plane bond length is longer than the in-plane one in accordance with anisotropy in transport and magnetization properties. The anisotropy in bond length or in other words the anisotropy in orbital hybridization can be studied directly using linearly polarized XAS. As it is shown schematically in Figure 64, vertically and horizontally polarized x-rays probe out-of-plane and in-plane orbitals, respectively. For the transition metals with the *d* shell as the valence band *e.g.* Mn, parallel and perpendicular polarized x-rays probe $d_{3z^2-r^2}$ and $d_{x^2-y^2}$ orbitals, respectively. Although, technically the incident angle cannot be set to bigger angles than 75°, yet the linearly polarized XAS in this configuration gives acceptable results.

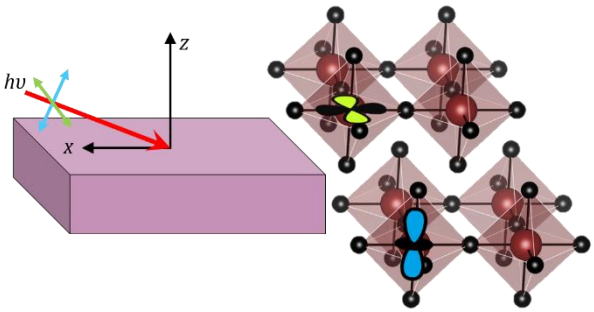

Figure 64 Schematic view of linearly polarized XAS. Vertically and horizontally polarized x-ray beam probes out-of-plane and in-plane orbitals, respectively.

For the tetragonally distorted $La_{1-x}Sr_{1+x}MnO_4$ (x=0.0), linearly polarized XAS spectra should show larger spectral weight for out-of-plane orientation comparing to in-plane indicating more hole consisting in the bonding between Mn and apical oxygen atoms *i.e.* lower electron density within this bond.

As it is mention before, hole-doping establishes a two dimensional charge-orbital order at the doping level of x=0.5 where the e_g electrons reside in 90 degrees oriented $d_{3z^2-r^2}$ orbitals *i.e.* $d_{3x^2-r^2}$ and $d_{3y^2-r^2}$. In this situation, the Mn-O bonds either with the planar or the apical oxygen atoms become identical in length acquiring a symmetric distribution of electrons in both in- and out-of-plane orientation. As a matter of fact, it is expected for $La_{1-x}Sr_{1+x}MnO_4$ (x=0.5) to observe a similar XAS spectra for both polarization directions.

In this context, linear dichroism (LD) can be used as the difference between vertically polarized and horizontally polarized spectra. Since the LD originates mostly from the preferential orbitals occupied by e_g electrons (the contribution of t_{2g} electrons within the aforementioned difference is negligible), it can be used to identify which state of the degenerated d orbital is occupied by e_g electron ($d_{3z^2-r^2}$ or $d_{x^2-y^2}$).

In the following section, a review on numbers of studies will be given where the Mn orbital occupation in single-layered manganite using linearly polarized XAS have been investigated.

5.1.1. Linearly Polarized X-ray Absorption Spectroscopy: Pros and Cons

For the first time in 2004, Huang *et al.* measured linearly polarized XAS on $La_{1-x}Sr_{1+x}MnO_4$ (x=0.5) single crystal in Dragon beamline at National Synchrotron Radiation Research Center in Taiwan [59]. Due to incorrect adjustment in measurement setup, they did not interpret the data correctly and later in 2011, they performed the same measurement but in ID08 beamline at ESRF, Grenoble, France. In Figure 65, the linear dichroism of $La_{1-x}Sr_{1+x}MnO_4$ (x=0.5) is shown. The linear dichroism, here, is the subtraction of perpendicular to parallel XAS with respect to the c axis ($\mathbf{LD} = [(\mathbf{E} \perp c) - (\mathbf{E} \parallel c)]$).

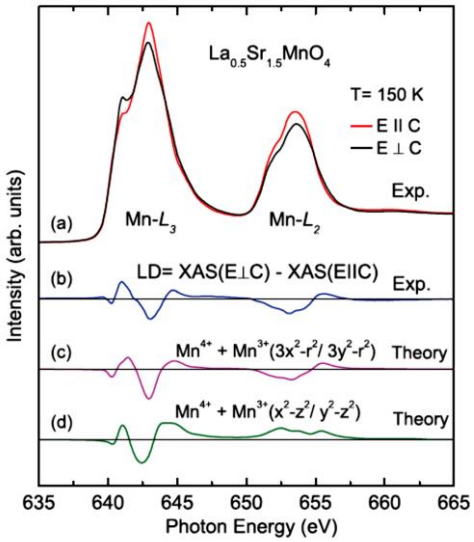

Figure 65: (a) Linear dichroism of Mn $L_{2,3}$-edges of $La_{1-x}Sr_{1+x}MnO_4$ (x=0.5). Here linear dichroism is defined as $\mathbf{LD} = [(\mathbf{E} \perp c) - (\mathbf{E} \parallel c)]$. (b) Calculated LD signals of Mn^{3+} ions with $d_{3x^2-r^2}/d_{3y^2-r^2}$ and $d_{x^2-z^2}/d_{y^2-z^2}$ orbital occupation [134].

Comparing the experimental data with the simulated LDs, they reported $d_{3x^2-r^2}/d_{3y^2-r^2}$ as the preferential orbital occupation of e_g electrons [134].

RIXS measurements at Mn $L_{2,3}$-edges at fixed orbital order vector wave of $\mathbf{q} = \left(\frac{1}{4}, \frac{1}{4}, 0\right)$ by Wilkins *et al.* in 2005 [135] revealed the predominant orbital of e_g electrons in $La_{1-x}Sr_{1+x}MnO_4$ (x=0.5) as $d_{x^2-z^2}/d_{y^2-z^2}$ in agreement with former report by Huang and Wu *et al.* [59, 60].

The linearly polarized XAS measurements at the K-edge of Mn on $La_{1-x}Sr_{1+x}MnO_4$ (x=0.0. 0.3 and 0.5) were performed by Herrero-Martín *et al.* in 2005 showing anisotropy in orbital occupation in agreement with previous studies [61].

As it is shown in Figure 66, the anisotropy between out-of-plane and in-plane polarized XAS decreases by increase of hole-doping. They reported that the absorption edge delta between XAS at the two polarization direction is 3.3, 1.7 and 0.5 eV for x=0.0, 0.3 and 0.5, respectively [61]. The K-edge is a well-structured edge ($1s \longrightarrow 4p$), it represents the oxidation state of probed element quite precisely. Here, the linearly polarized XAS gives, in principle, the difference in

Mn-O bond length between *a b* and *c* orientations. Clearly, due to Jahn-Teller distortion in MnO_6 octahedra for undoped $La_{1-x}Sr_{1+x}MnO_4$, the out-of-plane component exhibits an absorption edge for 3.3 eV lower than in-plane one indicating a distortion in out-of-plane orientation. And, as hole-doping level increase, a more isotropic geometry of Mn-O bonds forms.

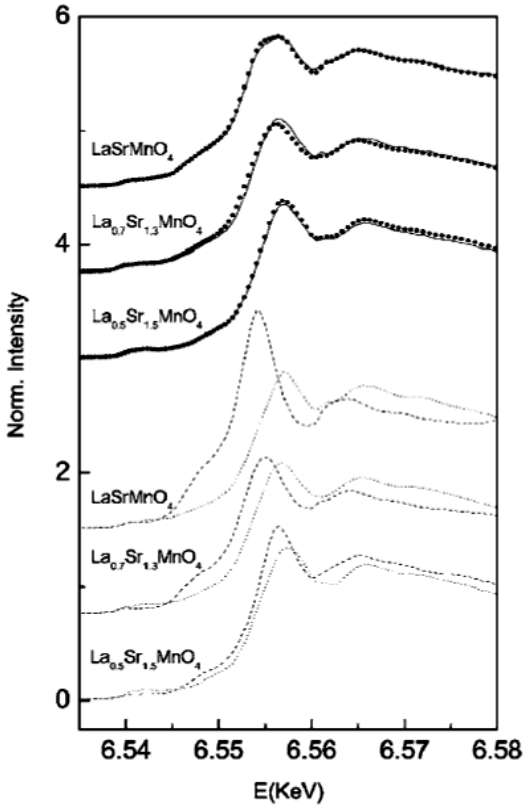

Figure 66: XAS at the *K*-edge of Mn on $La_{1-x}Sr_{1+x}MnO_4$ (x=0.0. 0.3 and 0.5) at room temperature (Up) non-polarized XAS (solid line) and sum of the in- and out-of-plane polarized spectra (circles). (Down) linearly polarized spectra perpendicular $\mathbf{E} \parallel c$ (dashed line) and parallel $\mathbf{E} \perp c$ (dotted line) to the *c* axis [61].

Linearly polarized XAS measurements by Merz *et al.* [63, 136] at O *K*-edge and Mn *L*-edge on a series of $La_{1-x}Sr_{1+x}MnO_4$ single crystal samples (x=0.0, 0.13, 0.25, 0.4 and 0.5) revealed a mixed in- and out-of-plane orbital occupation for Mn.

The Linearly polarized XAS spectra at O *K*-edge $\mathbf{E} \parallel a$ *i.e.* in-plane configuration for $La_{1-x}Sr_{1+x}MnO_4$ $0.0 \leq x \leq 0.5$ are shown in Figure 67. Neglecting the weak contribution of π-type hybridization of Mn-3*d* t_{2g} electrons with O-2*p* electrons, the spectra reflects the hybridization of planar oxygen atoms with the cations *i.e.* Mn, La and Sr. With increase in photon energy, there are three distinctive features in these spectra. These features are associated with valence band, upper Hubbard band and the hybridization of ***A***-site cation and oxygen. The last feature will not be discussed here. The valence band reflects the Mn-O bond strength on one hand side, and also the total number of electrons contributing to the bonding hybridization. The upper Hubbard band is due to the σ-type hybridization of Mn-3*d* e_g with

O-2*p* electrons. By hole-doping, the valence band shifts to lower energies and its spectral weight increase, while the upper Hubbard band position does not change, but its intensity decreases until at x=0.5 completely vanishes.

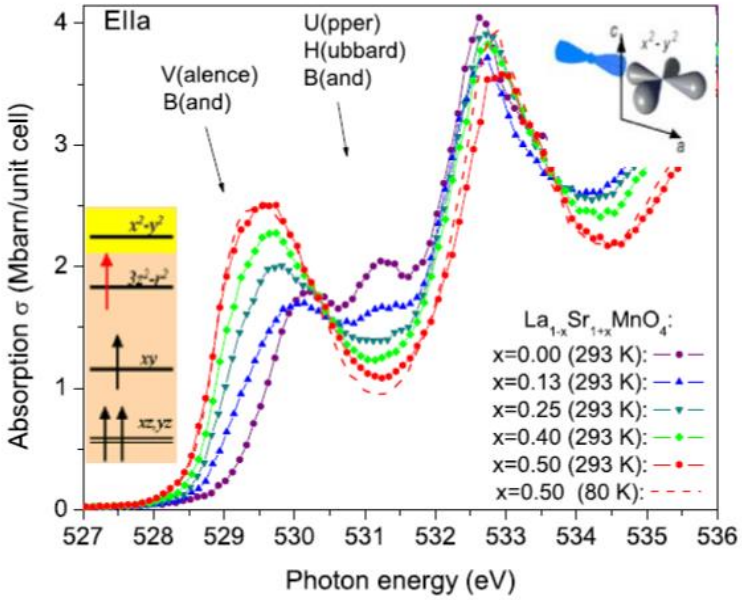

Figure 67: Linearly polarized XAS spectra at O *K*-edge **E** ∥ *a i.e.* **E** ⊥ *c* (in-plane configuration) for $La_{1-x}Sr_{1+x}MnO_4$ $0.0 \leq x \leq 0.5$ [63]. In the top right corner of the graph, the possible in-plane *d* orbital of Mn σ-bonded to O *p* orbital is shown.

A similar trend of evolution for these two features can be seen in the spectra of the other polarization measurements **E** ∥ *c i.e.* out-of-plane configuration (Figure 68).

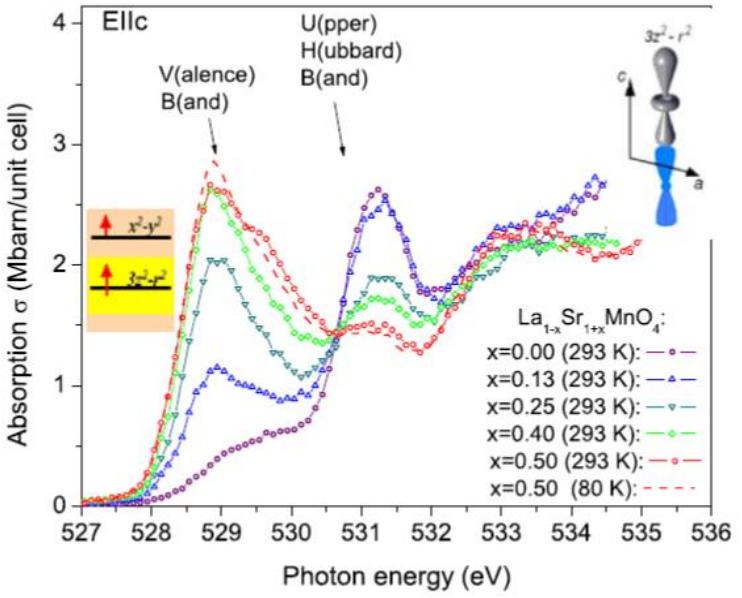

Figure 68: Linearly polarized XAS spectra at O *K*-edge **E** ∥ *c i.e.* (out-of-plane configuration) for $La_{1-x}Sr_{1+x}MnO_4$ $0.0 \leq x \leq 0.5$ [63]. In the top right corner of the graph, the possible out-of-plane *d* orbital of Mn σ-bonded to O *p* orbital is shown.

Upon hole-doping, the very low intense, yet not zero, valence band of undoped $La_{1-x}Sr_{1+x}MnO_4$ evolves, while for quite distinctive upper Hubbard band, a drop in the intensity can be seen (yet not zero). These two complementary pictures indicate that by hole-doping, the e_g electrons from upper Hubbard band transfer to the valence band [63, 136].

For the undoped $La_{1-x}Sr_{1+x}MnO_4$ (x=0.0), Mn^{3+} cations $\left(t_{2g}^3 e_g^1\right)$ are located in the center of Jahn-Teller distorted octahedra (c-axis oriented) and e_g electrons reside in $d_{3z^2-r^2}$ orbital. However, XAS measurements by Merz *et al.* [63, 136] do not substantially confirm this scenario. In the in-plane configuration, still upper Hubbard band is visible indicating the fact that part of the e_g electrons reside in $d_{x^2-y^2}$ orbital. This fact can be also seen in the out-of-plane configuration where still part of the valence band is distinguishable.

Similarly, for half-doped $La_{1-x}Sr_{1+x}MnO_4$ (x=0.5), in the out-of-plane configuration, the upper Hubbard band has not been washed out. Furthermore, valence band is actually a double peak. Merz *et al.* attributed the shoulder on the lower energy of the valence band to the $d_{3z^2-r^2}$ orbital and the shoulder on the higher energy side to the $d_{3x^2-r^2}/d_{3y^2-r^2}$ orbitals [63, 136]. This indicates that part of the e_g electrons in the half-doped $La_{1-x}Sr_{1+x}MnO_4$ reside in out-of-plane orbital. They estimated the fraction of e_g electrons reside in the non-expected orbital for both the undoped and the half-doped $La_{1-x}Sr_{1+x}MnO_4$ as 15%.

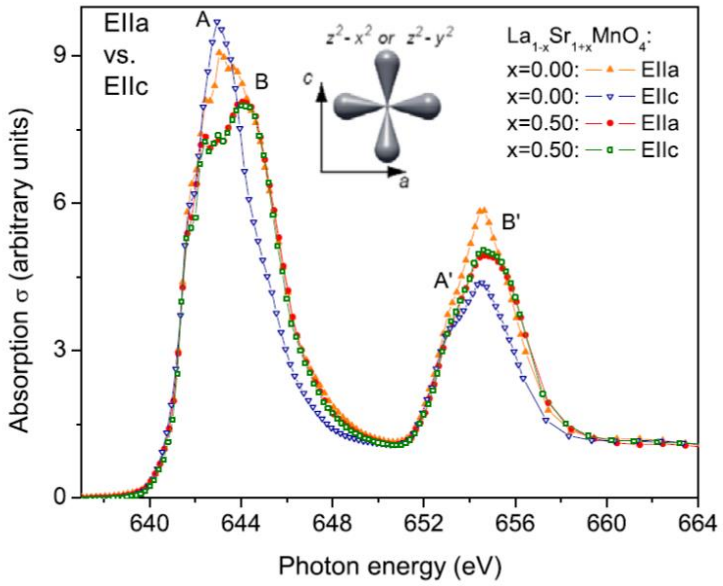

Figure 69 Normalized linearly polarized XAS spectra at Mn $L_{2,3}$-edges of $La_{1-x}Sr_{1+x}MnO_4$ (x=0.0, 0.5) for both polarization direction **E** ∥ c *i.e.* out-of-plane configuration and **E** ∥ a *i.e.* in-plane configuration [63].

The XAS at Mn $L_{2,3}$-edges of $La_{1-x}Sr_{1+x}MnO_4$ (x=0.5) for both polarization direction **E** ∥ c and **E** ∥ a (Figure 69) shows a point-to-point identical spectra mimicking a symmetric non-distorted MnO_6 octahedra. This result suggests that the e_g electrons in half-doped $La_{1-x}Sr_{1+x}MnO_4$ (x=0.5) reside in $d_{3x^2-r^2}/d_{3y^2-r^2}$ orbitals. Here, there is no indication of

fractionally residing of e_g electrons in $d_{3z^2-r^2}$ orbital, yet the authors refer to the O *K*-edge rather than Mn $L_{2,3}$-edges insisting on the aforementioned statement. On the other hand, XAS spectra for undoped component (x=0.0) shows a pronounced **A** (**B**) feature (Figure 69) at out-of-plane (in-plane) configuration. Thus, the feature **A** can be accounted for elongated *c* orientation orbital, while feature **B** reflects the environment of Mn e_g electrons in in-plane orientation which expected to be surrounded by planar oxygen atoms.

In general, the assignment of non-controversial orbital state of e_g electrons in half-doped single-layered manganite has not been achieved. Either residing of e_g electrons in $d_{3x^2-r^2}/d_{3y^2-r^2}$ or $d_{x^2-z^2}/d_{y^2-z^2}$ orbitals or a mixture of these two has been proposed by different groups through various investigations which were reviewed in this section.

5.2. The Effect of Strain on Orbital Occupation of Mn

Linearly polarized XAS were performed at Mn $L_{2,3}$-edges at the Berlin synchrotron radiation source (BESSY II) at UE52-PGM beamline. The excitation energy of 2*p* core level electrons of 3*d* transition metals is in the range of 400-1000 eV. Thus, synchrotron based soft x-rays will be appropriate to investigate the electronic structure of Mn ions in $La_{1-x}Sr_{1+x}MnO_4$ by exciting $2p \longrightarrow 3d$. By grounding the sample to the earth and measuring the electrical current generated by the photoelectrons using a picoammeter, the unoccupied density of states in 3*d* shell can be probed which will reveal indirectly the local geometric and electronic structure of the target element. This is the concept of *total electron yield* (TEY) measurement of XAS.

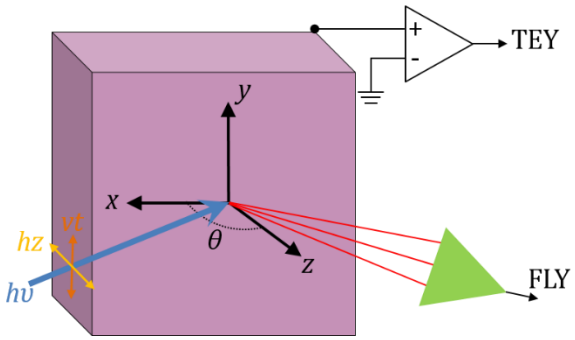

Figure 70: Schematic view of linearly polarized XAS measurement setup.

On the other hand, by using an x-ray fluorescent detector, the characteristic fluorescence can be measured which corresponds to the unoccupied density of states in 3*d* shell, as well. Here, by increase in unoccupied density of state in the 3*d* shell, the energy level of screening electrons will be higher which can be identified based on the characteristic emitted florescence. This is the concept of *fluorescent yield* (FLY) measurement of XAS.

In Figure 70, the schematic view of linearly polarized XAS measurement setup is shown. The samples were placed vertically in the direction of the beam with incident angle of 75°. As it is shown in Figure 70, the horizontally polarized x-ray probes the out-of-plane $d_{3z^2-r^2}$ orbitals, while the vertically polarized beam registers the in-plane $d_{x^2-y^2}$ orbitals.

The spectra were recorded by measuring in TEY mode with photon energy resolution of 0.1 eV and were normalized to about 10 eV above and below the edges. The photon energy was calibrated by the standard Au 4*f* binding energy using integrated photoemission spectrometer. In the shown geometry, the XAS spectra with vertically polarized x-ray beam probe only in-plane-oriented orbitals. However, the spectra recorded at the horizontally polarized x-ray beam reflect a mixed in- and out-of-plane orbital occupation of the Mn cations. As a result, the intensity of XAS at horizontal polarization I_{hz} contains intensity of absorption at both crystal orientation (I_z and I_{xy}). For the spectral intensity measured at the angle θ, the equation proposed by van der Laan *et al.* [137, 138] can be used to separate I_z and I_{xy}:

$$I(\theta) = I_z \cos^2\theta + I_{xy} \sin^2\theta \qquad (13)$$

By applying the equation (13) for the measurements at horizontal polarization, I_{hz} were calculated. In Figure 71, the sum of corrected intensities (pure I_{hz} and I_{vt}) along with sum of as-measured intensities for both polarization direction are shown.

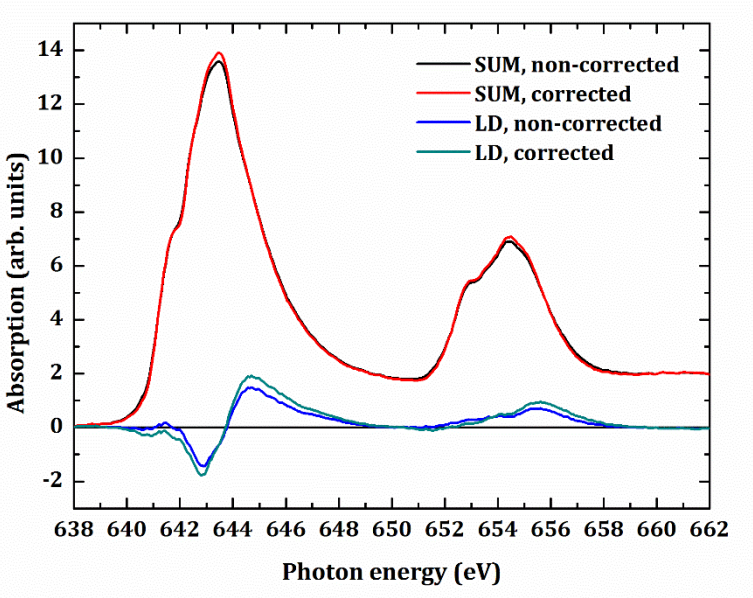

Figure 71: Sum and linear dichroism of as-measured and corrected linearly polarized XAS spectra for La1-xSr1+xMnO4 (x=0.0) on LSAT substrate. The term corrected refer to application of equation (13) on measured spectra.

As it can be seen (Figure 71), there is a minute difference in sum of XAS spectra at the two polarization direction between the corrected and non-corrected one. However, the LD signals *i.e.* $I_{vt} - I_{hz}$ or $\mathbf{E} \parallel a - \mathbf{E} \parallel c$ for the corrected spectra shows a bigger total spectral weight. The

LD signal registers the fine differences between two polarization directions and thus is very sensitive. Thus, it is rational to correct the spectra.

In section 4.4, it has been shown by XPS measurements that the films with similar La/Sr ratio exhibit a similar Mn-2*p* spectrum indicating the fact that, the oxidation state of Mn in these films is conserved and has not been changed during the film deposition process. Moreover, doping $La_{1-x}Sr_{1+x}MnO_4$ with Sr (x=0.5) leads to a shift in the edge of the Mn-2*p* spectrum by 0.5 eV. Furthermore, the valence band structure of films with same La/Sr ratio also shows almost identical features. By having these reminders, the fact that the difference in linearly polarized XAS spectra may originate in different oxidation state of Mn can be ruled out.

To examine the effect of in-plane strain on the orbital occupation *i.e.* MnO_6 octahedra distortion, first the linearly polarized XAS spectra of $La_{1-x}Sr_{1+x}MnO_4$ (x=0.0) on LSAT and NGO substrates is shown (Figure 72). The films on LSAT and NGO substrate are interesting considering their lattice mismatches. LSAT crystallizes in a cubic structure with a half lattice constant of a=3.860 Å. On the other hand, NGO crystallizes in orthorhombic structure with pseudoperovskite lattice constant of a=3.861 Å. Due to the similar in-plane lattice constant, the deposited $La_{1-x}Sr_{1+x}MnO_4$ films show similar in- and out-of-plane lattice constants. Thus, $La_{1-x}Sr_{1+x}MnO_4$ (x=0.0) films are under in-plane tensile strain (Table III and Table VIII) and hence the out-of-plane lattice is suppressed.

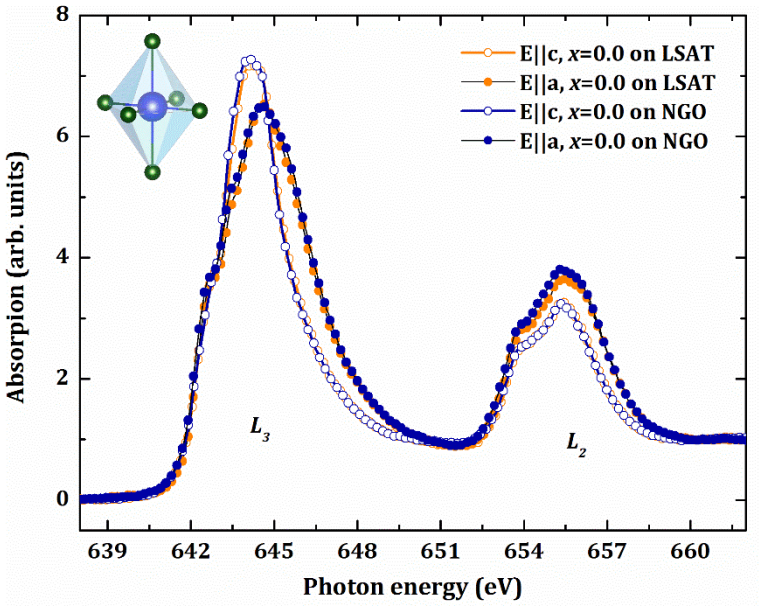

Figure 72: Linearly polarized XAS spectra of $La_{1-x}Sr_{1+x}MnO_4$ (x=0.0) on (0 0 1) LSAT and (1 0 1) NGO substrates recorded at room temperature and energy resolution of 0.5 eV. The measured points are reduced by a factor of 3 for the aim of demonstrating a clearer image. The schematic view of MnO_6 octahedron under out-of-plane suppression is shown on top left part of the figure.

In Figure 72, both linearly polarized XAS spectra for $La_{1-x}Sr_{1+x}MnO_4$ (x=0.0) films on LSAT and NGO substrates are shown. The XAS spectra with polarization direction of **E** ∥ *c* and **E** ∥ *a* of

both films are identical due to their expected similar lattice constants. Figure 72 shows that manipulating the orbital occupation via inducing strain is only a function of the quantity of strain and not the essence of the substrate.

The films of $La_{1-x}Sr_{1+x}MnO_4$ (x=0.0, 0.5) were deposited on LSAO and NGO substrates in order to alter the in- and out-of-plane lattice constants. The crystal structure of the films was presented in section 3.5 by XRD measurements. The stoichiometry of the films as well as the oxidation state of Mn and the valence band was demonstrated in section 4.4. Before presenting the linearly polarized XAS results of the films, the total absorption spectra were compared. By summing the spectra at two polarization directions, the total absorption spectra can be calculated (Figure 73). Since the area of the XAS spectrum registers the cross-section of excited electrons, one should expect equal spectral weight for the films with the same La/Sr ratio. Notice that the Mn-$L_{2,3}$ edges probe the unoccupied density of states in the 3d shell. Therefore, higher the spectrum area is, less the oxidation state will be. The spectral weight of $La_{1-x}Sr_{1+x}MnO_4$ (x=0.5) films, in this sense, should be smaller than the $La_{1-x}Sr_{1+x}MnO_4$ (x=0.0) films. $La_{1-x}Sr_{1+x}MnO_4$ (x=0.5) films show more or less equal spectral weights. However, the spectral weight of $La_{1-x}Sr_{1+x}MnO_4$ (x=0.0) film on LSAO is considerably bigger than the one on NGO. It is common to ascribe the spectral weight at L-edge to the hole concentration in valence shell of the probed element. But one should be careful with using the spectral weight as an indication of oxidation state in the measurements performed by TEY mode.

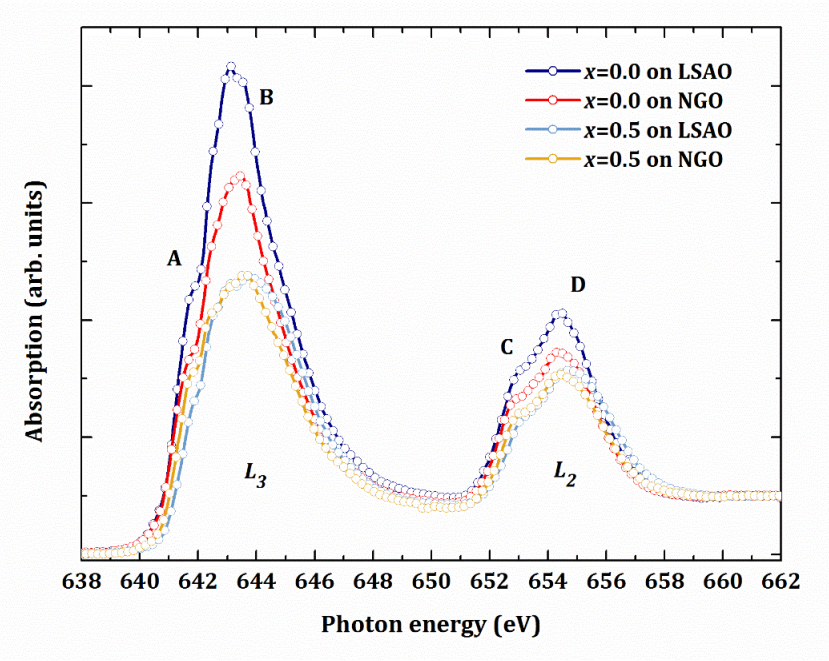

Figure 73: The total absorption intensity at Mn $L_{2,3}$-edges for $La_{1-x}Sr_{1+x}MnO_4$ (x=0.0, 0.5) films deposited on (0 0 1) LSAO and (1 0 1) NGO substrates. The features on L_3- and L_2-edge are marked with letters.

In TEY mode, the induced current upon excitation of electrons is being measured. In this way, the contact between the sample and the ground could be different for different samples. In addition, for thin film samples, the resistivity of the substrate affects the measured current since the film and the substrate form a series circuit. Therefore, assigning the spectral weight to the hole concentration of the valence shell for the samples on different substrate is ambiguous.

In Table XII, the calculated areas of the spectra are listed. The areas were calculated after subtraction of background using tangential step function $\left(arctan(E - E_0) + \frac{\pi}{2}\right) \times \frac{f_{arctan}}{\pi}$ where E_0 is the energy of the maximum of the spectrum and f_{arctan} is the factor that has to be applied in order to have the best possible fit of simulated background to the edges of the spectrum. Note that the background subtraction must be performed for each edge individually.

Table XII: Spectral weight of XAS at Mn-$L_{2,3}$ edges of $La_{1-x}Sr_{1+x}MnO_4$ (x=0.0, 0.5) films on (0 0 1) LSAO and (1 0 1) NGO substrate.

Sample	Area of L_2+ L_3	ratio
x=0.0 on LSAO	40.58	$\frac{40.58}{35.52} = 1.14$
x=0.0 on NGO	35.52	
x=0.5 on LSAO	34.01	$\frac{34.01}{29.84} = 1.14$
x=0.5 on NGO	29.84	

As it is listed in Table XII, the films deposited on LSAO substrates show larger spectral weight. The ratio of areas for films on LSAO to the ones on NGO for both Sr doping level (x=0.0, 0.5) is equal to 1.14. The reason could be found in the setup of the measurements. Both used substrates are dielectric material. The relative permittivity value of $NdGaO_3$ at room temperature is higher than $LaSrAlO_4$ substrate. Even at 6.5 GHz, $NdGaO_3$ has a relative permittivity of 23 [139], while at 10.7 GHz, the same entity for $LaSrAlO_4$ is not better than 17 [140] showing that NGO is a better insulator than LSAO. Hence, the spectra of the films on NGO show smaller areas. Furthermore, the ratio of the areas demonstrates a systematic contribution of the substrate in the XAS measurements.

Many studies have showed that the features in XAS spectra at Mn L-edge vary upon the change in oxidation state of Mn [141, 142]. For example, in Figure 74, it is shown that the position of the most intense peak (marked with B on the spectra shown on right) shifts about 1 eV to higher energies by hole-doping. This means that in perovskite manganite, change in oxidation state of Mn from +3 to +4 results in a shift (about 1 eV) of the feature with highest intensity. As a reference, we have measured the XAS at Mn L-edge of two manganese oxides (purity level 99.99%), namely Mn_2O_3 and MnO_2 with a non-polarized x-ray.

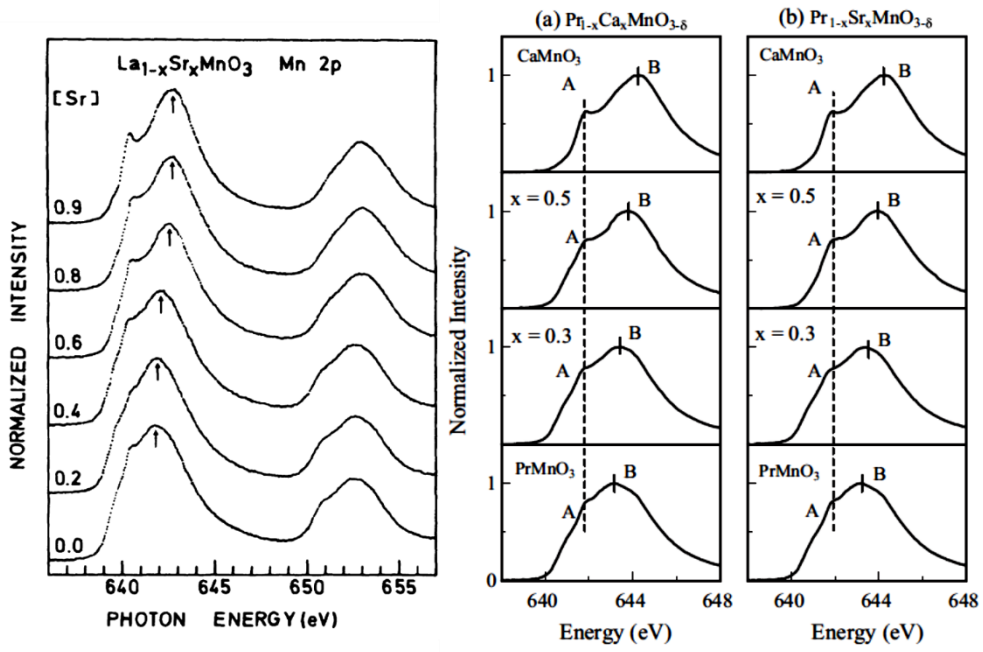

Figure 74: XAS spectra at Mn *L*-edge of (left) $La_{1-x}Sr_xMnO_3$ [141]; (right) $Pr_{1-x}Ca_xMnO_{3-\delta}$ (a) and $Pr_{1-x}Sr_xMnO_{3-\delta}$ (b) [142]. For different doping level of all three compounds, the position of feature (marked with A on the spectra on right) at 641.7 eV does not change, while the most intense peak (marked with B on the spectra on right) shifts to higher energies for higher doping levels.

By summing the different ratios of the measured XAS spectra of Mn_2O_3 and MnO_2, the intermediate oxidation states of Mn from +3 to +4 can be visualized (Figure 75).

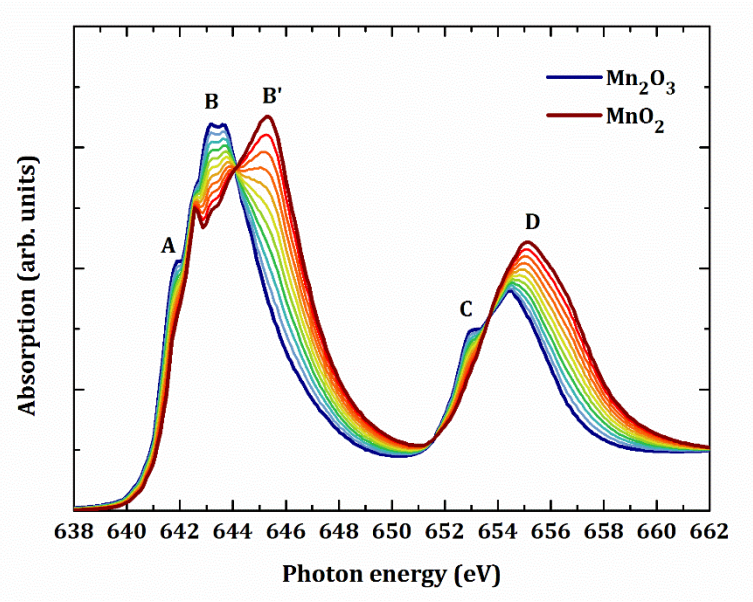

Figure 75: XAS spectra at Mn *L*-edge for Mn_2O_3 and MnO_2 measured with non-polarized x-ray. The thinner lines are the summation of the different ratios of the two measured spectra visualizing intermediate oxidation states of Mn with increment of 0.1 *i.e.* $Mn^{3.1+}$, $Mn^{3.2+}$ and *etc.*.

In agreement with the spectra measured for perovskite manganites [141, 142], the position of feature A does not change (Figure 75). The position of feature B, however, shifts to higher

energies for about 2 eV upon transition in oxidation state of Mn from 3+ to 4+. The shift is double of what has been observed for simple perovskite manganites which roots in the chemical environment of Mn in the binary oxide[16] and perovskite compounds.

The spectra of total absorption for $La_{1-x}Sr_{1+x}MnO_4$ (x=0.0, 0.5) films deposited on LSAO and NGO substrates were compared with the measured and calculate XAS spectra of manganese binary oxides (Figure 76).

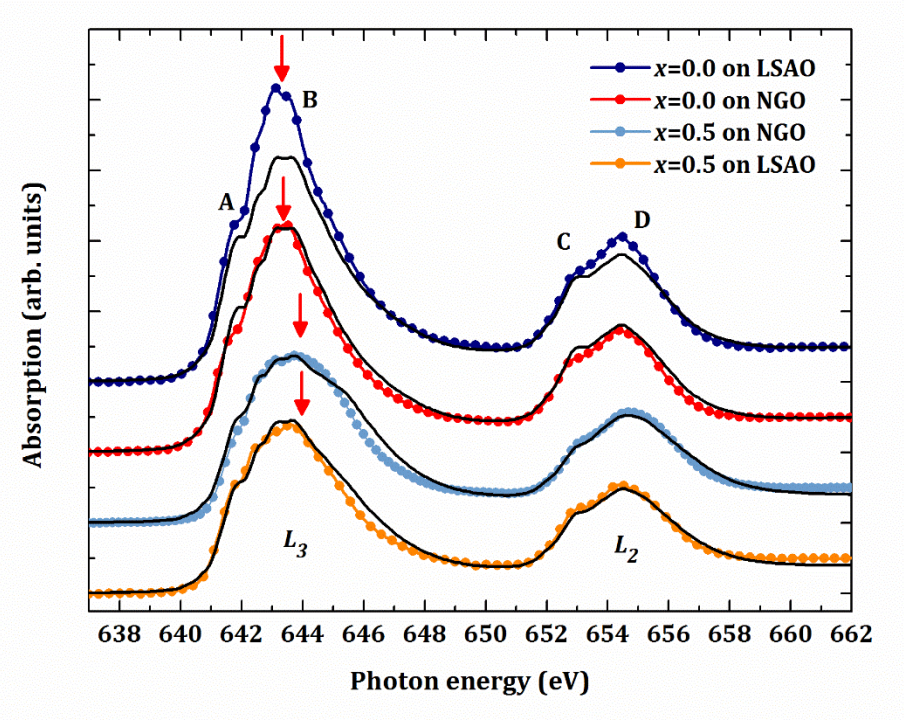

Figure 76: The total absorption intensity at Mn $L_{2,3}$-edges for $La_{1-x}Sr_{1+x}MnO_4$ (x=0.0, 0.5) films deposited on (0 0 1) LSAO and (1 0 1) NGO substrates compared with the measured and calculated XAS spectra of manganese binary oxides. The arrows show the position of most intense peak. The features on L_3- and L_2-edge are marked with letters.

As it is shown, upon hole doping (x=0.0 *vs.* x=0.5), the position of feature B shifts to higher energies by about 0.5 eV. This shift is in agreement with the values reported by Ref. [141, 142] revealing a +0.5 difference in oxidation states among these two sets of films.

Furthermore, the spectra of $La_{1-x}Sr_{1+x}MnO_4$ (x=0.0) films is comparable with Mn_2O_3 considering the similar features and their positions. On the other hand, the spectra of $La_{1-x}Sr_{1+x}MnO_4$ (x=0.5) films is comparable with the calculated intermediate oxidation state of $Mn^{3.3+}$. Regarding the 2 eV shift of feature B in the manganese binary oxide and comparing to half of this shift (1 eV) for perovskite manganite, one can ascribe this to $Mn^{3.5+}$ oxidation state for $La_{1-x}Sr_{1+x}MnO_4$ (x=0.5) films.

[16] Mn_2O_3 adopts the Corundum crystal structure, while MnO_2 crystallizes in Rutile structure.

In addition, in none of the XAS spectra, no peak could be ascribed to Mn^{2+}. The peak position of Mn^{2+} is around 640 eV which were reported for La deficient $LaMnO_3$ thin films. This is surprising considering the fact that TEY mode registers the photoelectrons from the topmost 4-5 nm depth [143]. Regarding the surface sensitivity of TEY measurement, lack of any Mn^{2+} peak suggests the abundance of contribution form surface dangling bonds.

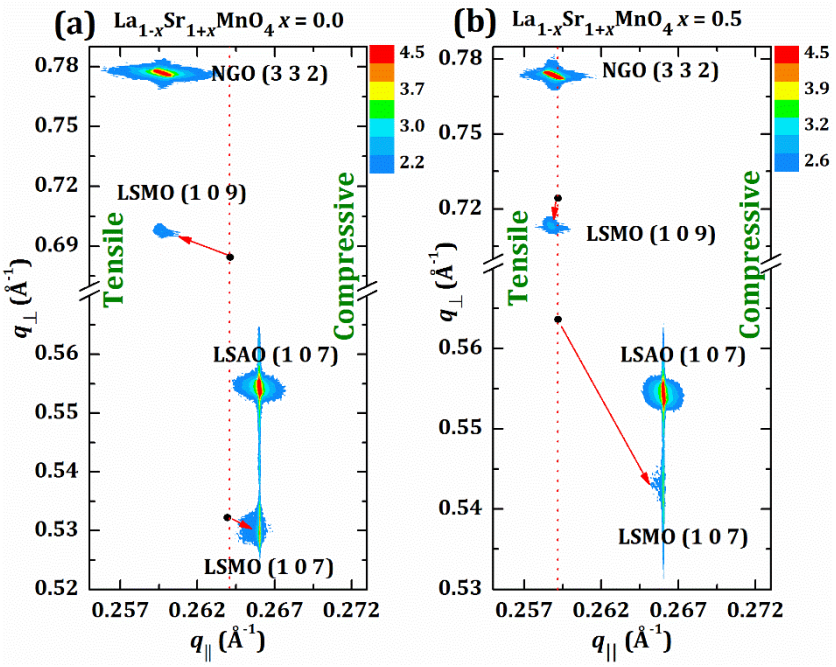

Figure 77: Reciprocal space map of $La_{1-x}Sr_{1+x}MnO_4$ (x=0.0, 0.5) films deposited on (1 0 1) NGO and (0 0 1) LSAO substrates. The black solid dots represent the spatial reflection (107 or 109) of corresponding bulk $La_{1-x}Sr_{1+x}MnO_4$. The red arrows show the change in $q_\perp$ and $q_\parallel$ of spatial reflections of corresponding bulk values upon formation of fully strained thin films. The dotted red vertical lines separate the tensile and compressive strain regions.

In Figure 77, as a reminder the RSM of $La_{1-x}Sr_{1+x}MnO_4$ (x=0.0, 0.5) films deposited on NGO and LSAO substrates are shown.

The $La_{1-x}Sr_{1+x}MnO_4$ (x=0.0) films on LSAO and NGO substrate are under compressive and tensile strains, respectively. The in-plane tensile strain on NGO substrate (1.72%) is more than twice big as compressive strain on LSAO (-0.71%). This leads to suppression of c lattice constant by -1.98% on NGO substrate almost five times as the elongation in same lattice (0.43%) by deposition on LSAO substrate (see Table VIII). Figure 78 represents the XAS spectra at both polarization directions, the total absorption spectra and the LD signals for $La_{1-x}Sr_{1+x}MnO_4$ (x=0.0) film on NGO and LSAO substrates.

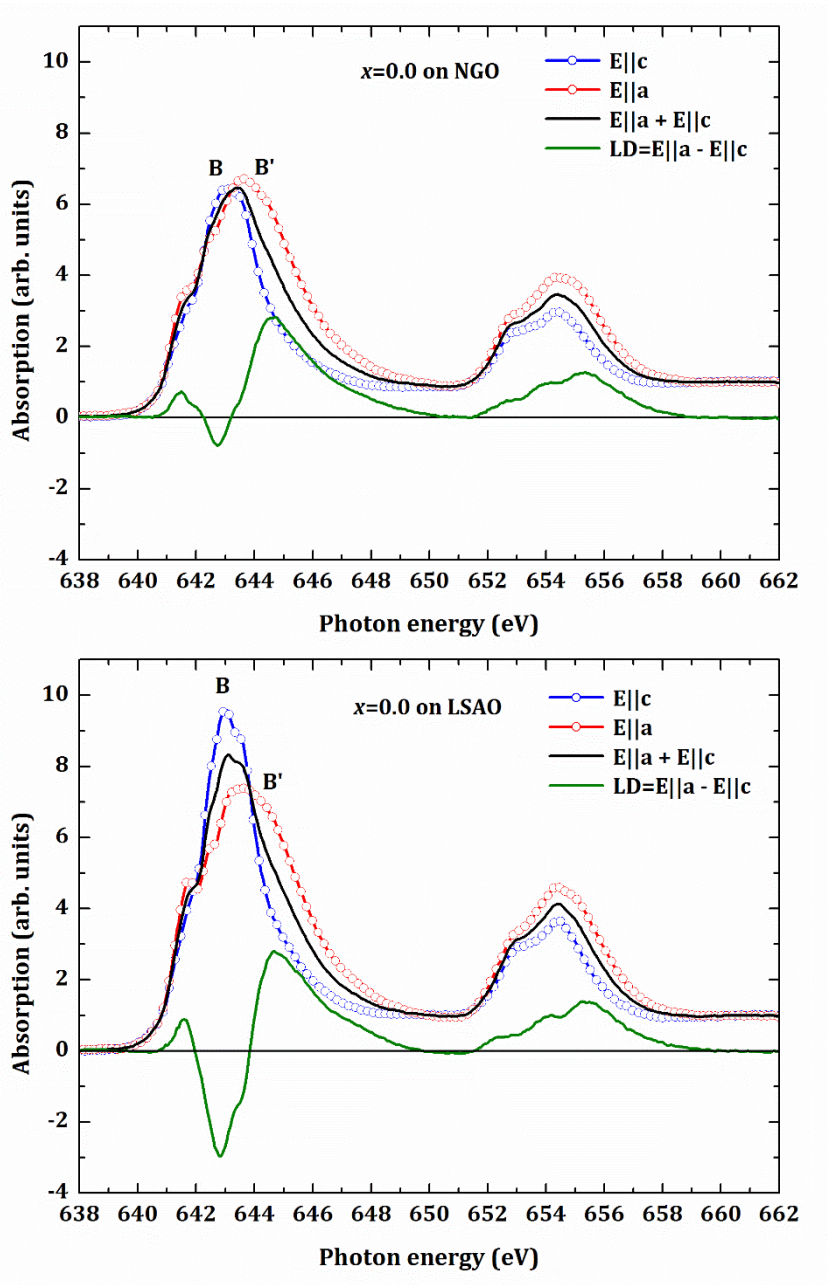

Figure 78: XAS spectra of the $La_{1-x}Sr_{1+x}MnO_4$ (x=0.0) film on (1 0 1) NGO and (0 0 1) LSAO substrates. The sum of XAS at two polarization directions along with linear dichroism (LD= **E**||a - **E**||c) are shown.

The feature B and B' in Figure 78 are ascribed to Mn^{3+} and Mn^{3+x} components, respectively. It had been shown that upon hole-doping, the feature B in total absorption spectra at the L_3-edge shifts towards higher energies forming the feature B'. In other words, upon hole doping, the e_g electrons transfer from out-of-plane orbital to the in-plane one *i.e.* from $d_{3z^2-r^2}$ to $d_{x^2-y^2}$ orbitals. The linear polarized spectra of $La_{1-x}Sr_{1+x}MnO_4$ (x=0.0) reported by Merz *et al.* [63] also show an out-of-plane-like and in-plane-like character at **E**||c and **E**||a polarizations, respectively (Figure 69). By inducing compressive (tensile) strain on $La_{1-x}Sr_{1+x}MnO_4$ (x=0.0) film via deposition on LSAO (NGO) substrate, the out-of-plane character of **E**||c polarized

spectrum is pronounced (eliminated). On the contrary, the signature and shape of spectra with **E**||a polarization does not change considerably.

Several investigations on $La_{1-x}Sr_xMnO_3$ thin films revealed that inducing compressive and tensile strain causes preferential orbital occupation to $d_{3z^2-r^2}$ (out-of-plane configuration) and $d_{x^2-y^2}$(in-plane configuration), respectively [109, 144-148]. Simulation using either single-ion diagonalization [149] or atomic model calculation [109, 147] shows that a preferred $d_{3z^2-r^2}$ ($d_{x^2-r^2}$) orbital generates the XAS spectra at out-of-plane (in-plane) polarization with larger spectral weight, thus the LD would be positive (negative). Using this method, based on LD signature and its sign[17], it could be stated that which orbital is occupied by e_g electrons.

The $La_{1-x}Sr_{1+x}MnO_4$ (x=0.0) films under both compressive and tensile strain show a positive LD (Figure 78) revealing the orbital occupation of e_g electrons on both sides of strain regime as $d_{3z^2-r^2}$. This signifies that even upon in-plane tensile strain up to 1.72%, still the preferred orbital occupation remains in $d_{3z^2-r^2}$ orbital. This result is quite surprising since inducing half of such in-plane strain to perovskite manganite compound ($La_{1-x}Sr_xMnO_3$ on STO, 0.9% in-plane strain) alters the orbital occupation to in-plane one i.e. $d_{x^2-r^2}$ [109, 146].

On the other hand, the $La_{1-x}Sr_{1+x}MnO_4$ (x=0.5) film on NGO shows a tiny in-plane strain in tensile region (Figure 77). This film has been considered as the film without any in-plane strain (see section 3.5). In contrast, the $La_{1-x}Sr_{1+x}MnO_4$ (x=0.5) film on LSAO shows a considerable in-plane compressive strain and consequently also considerable elongation in out-of-plane axis ($q_{\parallel}$ and $q_{\perp}$ are inverse to d-spacing values, see section 3.4). In Figure 79, the XAS spectra at two polarization directions along with the sum of the spectra and LD for the $La_{1-x}Sr_{1+x}MnO_4$ (x=0.5) film on NGO and LSAO substrates are shown. Since there is almost no in-plane strain for $La_{1-x}Sr_{1+x}MnO_4$ (x=0.5) film on NGO, one expects identical spectra for **E**||a and **E**||c, and hence observation of zero LD. The spectra at two polarizations are very similar, yet not completely identical. The reason for such non-absolute similarity is the minute tetragonal distortion which is observed in RSM measurement. Furthermore, the LD for this film is not zero. However, it is a very week LD signal comparing the scale of this film to the ones of $La_{1-x}Sr_{1+x}MnO_4$ (x=0.0) films (Figure 78).

[17] The sign of LD is determined by integration the LD signal over the energy range. For instance, in this study, the energy range of 638-662 eV (L_3 and L_2 edges) was taken into account for the integration.

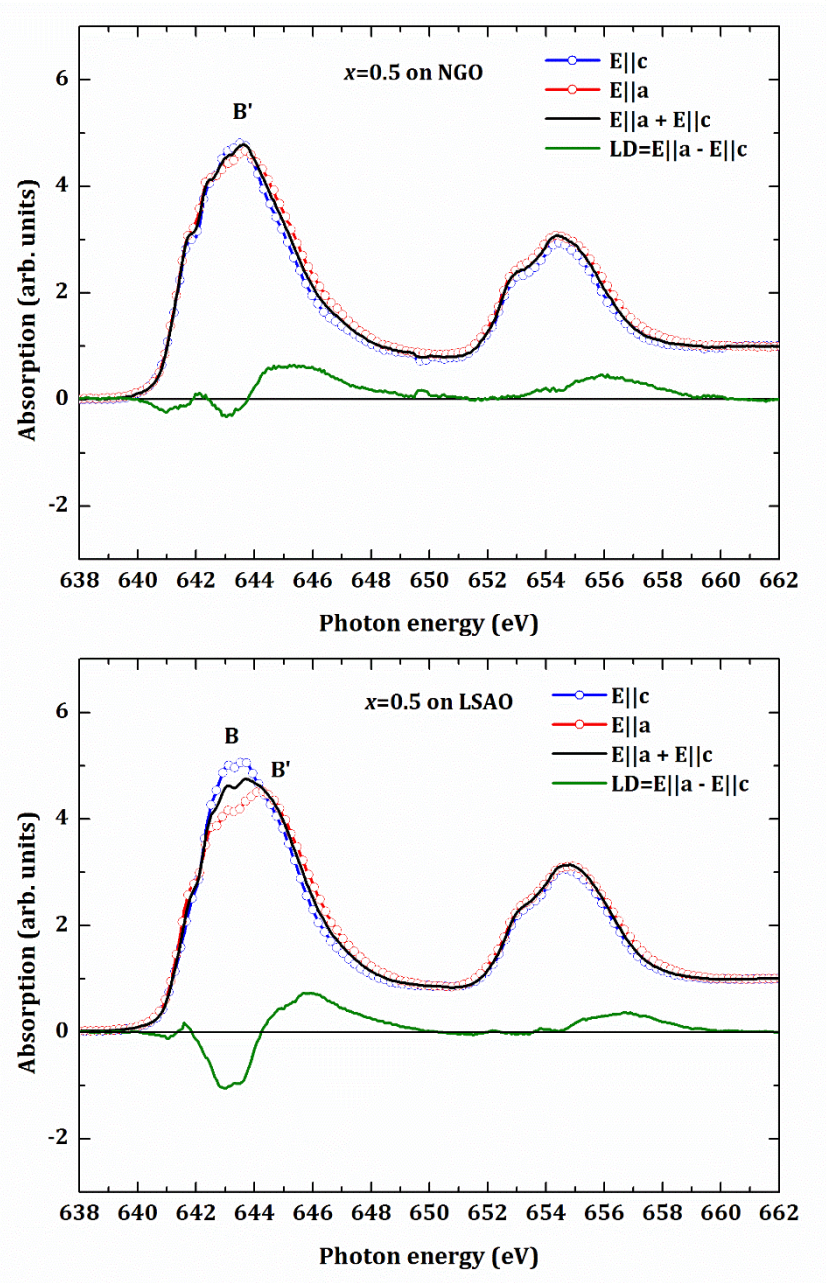

Figure 79: XAS spectra of the $La_{1-x}Sr_{1+x}MnO_4$ (x=0.5) film on (1 0 1) NGO and (0 0 1) LSAO substrates. The sum of XAS at two polarization directions along with linear dichroism (LD= **E**||a - **E**||c) are shown.

Very recently, Pesquera *et al.* reported similar observation for $La_{1-x}Sr_xMnO_3$ (x=0.3) thin films grown on LSAT substrate (with the thickness of 150 unit cells) where due to almost no lattice mismatch between the film and the substrate and, hence, no in-plane strain, it was expected to have zero LD. They reported similar result as we have observed here, a positive LD (preferential orbital occupation is $d_{3z^2-r^2}$) [109]. They also showed that for ultra-thin films (with the thickness of 4 unit cells), the LD is even more positive. They ascribed the observation of positive LD to the very topmost layers in the thin film which are subjected to the *free surface*

regime. This is in accordance with the emergence of more positive LD for ultra-thin film where the alignment of orbitals to out-of-plane configuration *i.e.* $d_{3z^2-r^2}$ is favorable.

For our $La_{1-x}Sr_{1+x}MnO_4$ (x=0.5) film on NGO (no strain), it is expected to have a mixture of $d_{3x^2-r^2}$ and $d_{3y^2-r^2}$ along with $d_{3z^2-r^2}$ orbitals at room temperature giving rise to observation of zero LD [63, 136]. As we know, cooling down below $T_{CO} \sim 220$ K stabilizes a charge-orbital order state where remaining $d_{3z^2-r^2}$ orbitals flip toward in-plane direction and a sole in-plane orbital occupation of $d_{3x^2-r^2}$ and $d_{3y^2-r^2}$ will be dominant [134]. For our relatively thin film with the thickness of 28 nm corresponding to ~21 unit cells, even a very tiny distortion along *c* axis, encourages the e_g electrons to occupy the out-of-plane configuration orbital *i.e.* $d_{3z^2-r^2}$. This means that, if Merz *et al.* [63, 136] reported residing of 15% of e_g electrons in $d_{3z^2-r^2}$ orbital, we established a system where more electrons are in the mentioned orbital.

The $La_{1-x}Sr_{1+x}MnO_4$ (x=0.5) film on LSAO shows a positive LD as well. Here, a compressive strain upon smaller lattice constant of LSAO substrate than the film was induced. The in-plane strain induction in this particular film comparing to the others is gigantic. In Figure 77, the very long arrow illustrates visually the quantity of alteration in both lattice constants. The -2.64% compressive strain leads to an elongation of 3.84% (see Table VIII). Thus, it is anticipated that the compressive in-plane strain provides a situation where out-of-plane configuration orbital *i.e.* $d_{3z^2-r^2}$ is favorable. In this way, a positive LD will be resulted same as what we observed for this film. This means that upon compressive strain, the preferential in-plane configuration *i.e.* $d_{3x^2-r^2}$ and $d_{3y^2-r^2}$ will be altered to $d_{3z^2-r^2}$ orbital. Comparing the feature B in these two spectra (Figure 79), it is noticeable that by inducing compressive strain, once again, a similar trend like what we have seen for the $La_{1-x}Sr_{1+x}MnO_4$ (x=0.0) films, the spectra with **E**||a polarization, does not change in shape and signature, while the spectra with **E**||c polarization transforms to a one with a more out-of-plane-like character.

For the comparison, XAS spectra of presented four films at each polarization direction are shown in Figure 80.

In summary, following points have to be highlighted:

- The XAS spectra with **E**||c polarization which probes the out-of-plane orientated orbitals ($d_{3z^2-r^2}$ for x=0.0) registered a more pronounced (suppressed) spectra for the films under compressive (tensile) strain *i.e.* $La_{1-x}Sr_{1+x}MnO_4$ (x=0.0) on LSAO (NGO) substrate (Figure 80a, b). Similarly, the XAS spectra with **E**||c polarization which probes $d_{x^2-z^2}/d_{y^2-z^2}$ for x=0.5 registered a more pronounced spectrum for the films under compressive strain *i.e.* $La_{1-x}Sr_{1+x}MnO_4$ (x=0.5) on LSAO substrate (Figure 80d)

- The XAS spectra with **E**||a polarization which probes the in-plane orientated orbitals ($d_{x^2-y^2}$ for x=0.0 and $d_{3x^2-r^2}/d_{3y^2-r^2}$ for x=0.5), on the other hand, does not change considerably. Despite of slight changes in some features among $La_{1-x}Sr_{1+x}MnO_4$ (x=0.0, 0.5) films on different substrates, no big pronounced feature can be seen (Figure 80a, b, d, e).

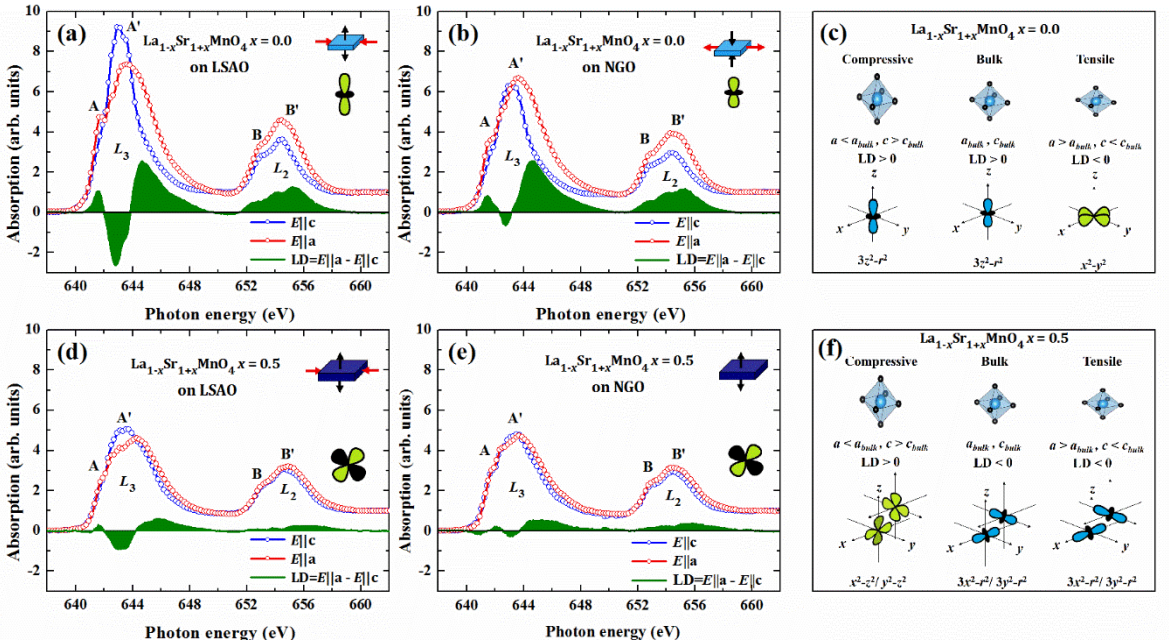

Figure 80: Linearly polarized XAS at Mn $L_{2,3}$-edges of $La_{1-x}Sr_{1+x}MnO_4$ (a, b) (x=0.0) and; (d, e) (x=0.5) films deposited on LSAO and NGO substrates. The directions of the applied compressive and tensile in-plane strain are shown schematically in the top right corners of the panels. The preferential orbital occupation of Mn^{3+} cations in the films is illustrated; (c) and (f) Schematic representation of the preferential orbital occupation of Mn^{3+} cations in $La_{1-x}Sr_{1+x}MnO_4$ (x=0.0) and (x=0.5), respectively: under in-plane compressive strain (left), unstrained bulk (center), and under in-plane tensile strain (right).

- All the LD signals for $La_{1-x}Sr_{1+x}MnO_4$ (x=0.0, 0.5) films on both NGO and LSAO substrates are positive. None of the films under tensile strain show any negative LD (Figure 80a, b, d, e). The positive sign for the films under compressive strain is what is expected (look at schematic orbital occupation in Figure 80c, f). The positive LD for the $La_{1-x}Sr_{1+x}MnO_4$ (x=0.0) film on NGO with in-plane tensile strain is due to not inducing enough tensile strain for encouraging the e_g electrons to reside along in-plane orientated orbitals (Figure 80c). The positive LD for the $La_{1-x}Sr_{1+x}MnO_4$ (x=0.5) film on NGO with almost no strain (Figure 80f) is due to slight tetragonal distortion which was detected for this film using RSM. The integrated area of LD signal for the films at L_3 and L_2 edges are listed in Table XIII for comparison.

Table XIII: The integrated area of LD signal at L_3 and L_2 edges. The in-plane stain calculated for the films out of RSM measurements is included.

Sample	L_3	L_2	L_3+L_2	c/a
x=0.0 on LSAO	4.3	4.7	9.0	3.517
x=0.0 on NGO	8.0	4.5	12.5	3.350
x=0.5 on LSAO	0.5	1.1	1.6	3.433
x=0.5 on NGO	1.7	1.7	3.4	3.263

The LD signal as a function of corresponding c/a ratio is plotted in Figure 81. The LD signals integrated over the Mn $L_{2,3}$ edges for $La_{1-x}Sr_{1+x}MnO_4$ (x=0.5) films are small due to a symmetric distribution of electrons in MnO_6 octahedra. Similarly, Merz *et al.* [63] reported an integrated LD signal equal to zero for $La_{1-x}Sr_{1+x}MnO_4$ (x=0.5) single crystals at room temperature. The observed integrated LD signals for the LSMO films with similar doping level are similar and vary only a little with strain. The integrated LD signals for the undoped $La_{1-x}Sr_{1+x}MnO_4$ (x=0.0) films are approximately 4-6 times larger than for the doped $La_{1-x}Sr_{1+x}MnO_4$ (x=0.5) ones as discussed before.

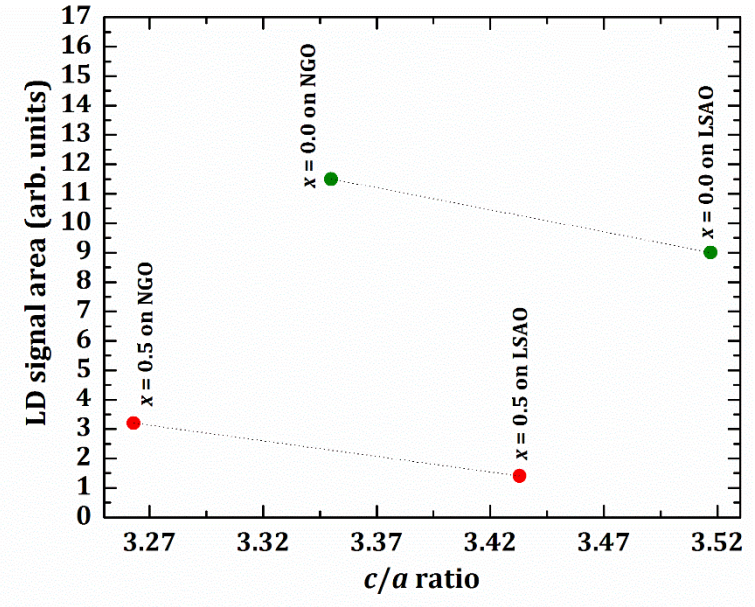

Figure 81: The integrated area of LD signal versus c/a ratio of corresponding films.

The interesting aspect of the Figure 81 is that the change in integrated area of LD signal with c/a ratio for both doping level follows a similar slope. This signifies that on one hand side the doping level has a major impact on the value of integrated area; and on the other hand side, the c/a ratio which reflects the effect of strain has a minor impact on it. By extrapolating the line for $La_{1-x}Sr_{1+x}MnO_4$ (x=0.5) for example, one finds a c/a ratio of 3.65 in order to have a tiny negative integrated area for LD signal. Such c/a ratio can be achieved by depositing $La_{1-x}Sr_{1+x}MnO_4$ (x=0.5) films on a substrate with in-plane lattice constant ranging from 3.6 to

3.7 Å which leads to an in-plane strain of 6.2 to 4.2%. Such strain range evolves very high energy levels which most probably will destroy the crystal lattice or it is more correct to be said that such structure will not form at the first place. It is quite clear that flipping the orbitals by applying strain for $La_{1-x}Sr_{1+x}MnO_4$ (x=0.0) is absolutely impossible considering the 4-6 times higher values for integrated area of LD signal comparing the ones for $La_{1-x}Sr_{1+x}MnO_4$ (x=0.5).

Summary

The deposition parameters for the growth of $La_{1-x}Sr_{1+x}MnO_4$ (x=0.0, 0.5) films were studied systematically. In particular, the deposition pressure and temperature were carefully monitored and optimized by attending to the phase purity, the crystal quality (using XRD) and the density (using XRR) as a guiding entity representing the stoichiometry. The best deposition condition is found to be 200 mTorr and 850 °C as deposition pressure and temperature respectively. The stoichiometry and the elimination of Sr segregation at the surface of the films were studied using angle-resolved XPS measurements. Using XPS, the growth kinetic of thin film growth was optimized by changing the laser fluency. It was shown that using lower laser fluence of 0.6 J/cm^2 eliminates the formation of a Sr-rich phase on the surface. The quantitative analysis of XPS spectra showed that within the measurement error, the films have a stoichiometric elemental ratio. XPS spectra of Mn-2p and O-1s and the valence band showed on one hand an identical spectra for the films with similar La/Sr ratio and on the other hand a shift in binding energy upon an increase in the doping level. The performed RSM measurements revealed that $La_{1-x}Sr_{1+x}MnO_4$ (x=0.0) films on LSAO and NGO substrate are under compressive and tensile strains, respectively. The in-plane tensile strain on NGO substrate (1.72%) is more than twice as big as the compressive strain on LSAO (-0.71%). This leads to a suppression of c lattice constant by -1.98% on NGO substrate, almost five times as much as the elongation in the same lattice (0.43%) by deposition on LSAO substrate. The preferential orbital occupation along in- and out-of-plane orientations was investigated using linearly polarized x-ray absorption spectroscopy. The XAS spectra with **E**||c polarization on $La_{1-x}Sr_{1+x}MnO_4$ (x=0.0) films deposited on LSAO (NGO) substrate registered a more pronounced (suppressed) spectra for the films under compressive (tensile) strain. The XAS spectra with **E**||a polarization on the other hand does not change considerably. Moreover, both films show an LD signal with a positive sign which signifies $d_{3z^2-r^2}$ orbital for Mn atoms. Thus the in-plane tensile strain is not sufficient enough to stabilize the $d_{x^2-y^2}$ orbital. On the other hand the $La_{1-x}Sr_{1+x}MnO_4$ (x=0.5) film on NGO shows a tiny in-plane tensile strain but a slight tetragonal distortion. Such distortion is reflected in the LD signal showing a positive sign ($d_{x^2-z^2}/d_{y^2-z^2}$ orbital). In contrast, the $La_{1-x}Sr_{1+x}MnO_4$ (x=0.5) film on LSAO shows a considerable in-plane compressive strain (-2.64%) and consequently also considerable elongation in out-of-plane axis (3.84%). Although, the sign of LD signal for this film is positive ($d_{x^2-z^2}/d_{y^2-z^2}$ orbital), it does not correlate to the considerable in-plane compressive strain. Comparing the integrated area of LD signal of the films as a function of the corresponding c/a ratio signifies that on the one hand the doping level has a major impact on the value of the integrated area, and on the other hand the c/a ratio which reflects the effect of strain has a minor impact on it. A simple

calculation shows that flipping the orbitals in single-layered manganites is impossible as the crystal structure will not hold together upon conserving a high amount of energy originating from the required applied strains.

Acknowledgement

Foremost, I would like to express my sincere gratitude to Prof. Dr. Lambert Alff for his continuous support, motivation, enthusiasm, and immense knowledge. Undoubtedly, without his guidance and persistent help, this thesis would not have been possible.

I would like to thank my defense committee, Prof. Dr. Wolfgang Donner, Prof. Dr. Wolfgang Ensinger and Prof. Dr. Barbara Albert, for their encouragement, insightful comments, and hard questions.

I am particularly grateful for the assistance, constructive comments and warm encouragement given by Dr. Philipp Komissinskiy who guided me like a big brother in every step I have taken during my Ph.D. studies.

I would like to express my appreciation to Dr. Jochen Geck who made enormous contribution to the investigations using XAS, the opportunity he provided for the measurements at BESSY and his further constructive discussion and comments.

I would like to particularly thank Dipl. Ing. Mehrdad Baghaie Yazdi for his real friendship, never-ending help and support, meticulous comments and his notorious illuminating criticism.

My thanks goes to my colleagues in ATFT group for the stimulating discussions, and for all the fun we have had in the last four years. I also thank Ms. Marion Bracke and Mr. Jürgen Schreeck for their great help.

I would like to thank my colleagues in Synchrotron studies of quantum matter group in IFW Dresden, Roberto Kraus and Dr. Valentina Bisogni for their great help regarding the measurements at BESSY.

I would like to thank my parents and my little sister for always believing in me, for their continuous love and their supports. Without whom I could not have made it here.

Even a single moment of the last four years could not have been spent on this thesis without the unconditional support of my wife. She was always there for me to listen to my work stories, to be a beautiful part of my happiness, to calm my anger down, to support me and to push me forward and to love me.

List of Figures

List of Tables

Appendices

Appendix I

Procedure of subtraction of La-MNN from La-3*d*:

This procedure is written based on Ref [116]. The XPS spectrum intensity (I) is a function of number of atoms per cm^3 (n), flux of incoming X-rays (I_0) in photons per cm^2 s, the photoelectric cross-section (σ), inelastic mean free path of photoelectrons (λ), the fraction of electrons detected by analyzer (D) [150].

$$I = nI_0\sigma\lambda D \tag{14}$$

The equation (14) is also valid for the Auger peaks concerning that the probability of Auger decay (P) should be considered.

$$I = nI_0\sigma\lambda DP \tag{15}$$

The ratio of La-3*d* and La-MNN using different X-ray sources either Al or Mg is the same. Thus

$$\frac{\frac{I_{3d,Al}}{nI_0\sigma_{3d,Al}\lambda_{3d,Al}D_{3d,Al}}}{\frac{I_{MNN,Al}}{nI_0\sigma_{MNN,Al}\lambda_{MNN,Al}D_{MNN,Al}P_{MNN}}} = \frac{\frac{I_{3d,Mg}}{nI_0\sigma_{3d,Mg}\lambda_{3d,Mg}D_{3d,Mg}}}{\frac{I_{MNN,Mg}}{nI_0\sigma_{MNN,Mg}\lambda_{MNN,Mg}D_{MNN,Mg}P_{MNN}}} \tag{16}$$

In equation (16), n, I_0 and P using either Al or Mg X-ray source are identical. Since the La-MNN Auger electrons also originate from 3*d* shell, thus the photoelectric cross-section of La-3*d* and La-MNN are equal. The inelastic mean free path of La-3*d* and La-MNN when using Al X-ray source are equal due to their same kinetic energy. Hence, equation (16) becomes

$$\frac{\frac{I_{3d,Al}}{D_{3d,Al}}}{\frac{I_{MNN,Al}}{D_{MNN,Al}}} = \frac{\frac{I_{3d,Mg}}{\lambda_{3d,Mg}D_{3d,Mg}}}{\frac{I_{MNN,Mg}}{\lambda_{MNN,Mg}D_{MNN,Mg}}} \tag{17}$$

The fraction of the electrons detected by analyzer which is called the transmission function is dependent on the angular efficiency factor of the instrument, the efficiency of photoelectric production, and the efficiency of photoelectrons detection from probed area. The transmission function is included in Tougaard background subtraction method [115, 151]. Thus, the intensity ratio of background subtracted spectra of photoelectron and Auger electrons will be

$$\frac{I_{3d,Al}}{I_{MNN,Al}} \cong \frac{\frac{I_{3d,Mg}}{\lambda_{3d,Mg}}}{\frac{I_{MNN,Mg}}{\lambda_{MNN,Mg}}} \tag{18}$$

Due to the overlap of La-3d and La-MNN spectra using Al X-ray source, equation (18) can be rewritten as

$$I_{MNN,Al} \cong \frac{I_{total,Al}}{1 + \frac{I_{3d,Mg} \times \lambda_{MNN,Mg}}{\lambda_{3d,Mg} \times I_{MNN,Mg}}} \tag{19}$$

where $I_{total,\,Al}$ is the sum of La-3*d* and La-MNN. Calculating the La-MNN and subtracting from overlapped spectra gives La-3*d*.

Appendix II

The three Hund's rules are as follows:

1. For a given electronic configuration, maximum total spin angular momentum $\boldsymbol{S} = \sum_i s_i$ has the lowest energy. In other words, if the orbital can be filled by electrons with parallel spins, it is more favorable than the ones with antiparallel spins.
2. Within the highest $\boldsymbol{S}$, maximum total orbital angular momentum $\boldsymbol{L} = \sum_i l_i$ has the lowest energy.
3. In the presence of spin-orbit coupling, for less than half full orbital, the total angular momentum $\boldsymbol{J} = |\boldsymbol{L} - \boldsymbol{S}|$ should have the minimum, while the maximum $\boldsymbol{J} = \boldsymbol{L} + \boldsymbol{S}$ is favorable when the shell is more than half filled.

The selection rules are as follows:

1. $\Delta \boldsymbol{L} = \pm 1$ states that for a given *p* orbital, the allowed transitions are $p \longrightarrow d$ and $p \longrightarrow s$. Similarly, $s \longrightarrow p$ is the allowed transition for *s* orbital.
2. $\Delta \boldsymbol{S} = 0$ states that the conservation of the spin orientation of the electrons within the transition should not be violated. It means that an up-spin electron can excite to an up-spin hole.
3. $\Delta \boldsymbol{J} = \pm 1, 0$. For instance, in $p \longrightarrow d$ transition, it states that $p_{1/2} \longrightarrow d_{5/2}$ is not allowed [121].

Bibliography

[**1**] T. J. O'Reilly and E. L. Offenbacher "Molecular orbital calculation for trigonally distorted octahedral complexes" J Chem Phys **54**, 3065 (1971).

[**2**] J. H. van Vleck "Theory of the variations in paramagnetic anisotropy among different salts of the iron group" Physical Review **41**, 208 (1932).

[**3**] H. A. Jahn and E. Teller "Stability of polyatomic molecules in degenerate electronic states. I-Orbital degeneracy" Proceedings of the Royal Society of London. Series A - Mathematical and Physical Sciences **161**, 220 (1937).

[**4**] D. N. Argyriou, D. G. Hinks, J. F. Mitchell, C. D. Potter, A. J. Schultz, D. M. Young, J. D. Jorgensen, and S. D. Bader "The room temperature crystal structure of the perovskite $Pr_{0.5}Sr_{0.5}MnO_3$" J Solid State Chem **124**, 381 (1996).

[**5**] P. G. Radaelli, M. Marezio, H. Y. Hwang, and S. W. Cheong "Structural phase diagram of perovskite $A_{0.7}A'_{0.3}MnO_3$ (A = La, Pr; A' = Ca, Sr, Ba): A new *Imma* Allotype" J Solid State Chem **122**, 444 (1996).

[**6**] J. Töpfer and J. B. Goodenough "$LaMnO_{3+\delta}$ Revisited" J Solid State Chem **130**, 117 (1997).

[**7**] E. O. Wollan and W. C. Koehler "Neutron diffraction study of the magnetic properties of the series of perovskite-type Compounds [(1-x)La, xCa]MnO_3" Physical Review **100**, 545 (1955).

[**8**] M. Imada, A. Fujimori, and Y. Tokura "Metal-insulator transitions" Rev Mod Phys **70**, 1039 (1998).

[**9**] P. G. Radaelli, M. Marezio, H. Y. Hwang, S. W. Cheong, and B. Batlogg "Charge localization by static and dynamic distortions of the MnO_6 octahedra in perovskite manganites" Phys Rev B **54**, 8992 (1996).

[**10**] H. Y. Hwang, S. W. Cheong, P. G. Radaelli, M. Marezio, and B. Batlogg "Lattice effects on the magnetoresistance in doped $LaMnO_3$" Phys Rev Lett **75**, 914 (1995).

[**11**] J. B. Goodenough "Theory of the role of covalence in the perovskite-type manganites [La, M(II)]MnO_3" Physical Review **100**, 564 (1955).

[**12**] C. Zener "Interaction between the *d*-shells in the transition metals. II. Ferromagnetic compounds of manganese with perovskite structure" Physical Review **82**, 403 (1951).

[**13**] P. W. Anderson and H. Hasegawa "Considerations on double exchange" Physical Review **100**, 675 (1955).

[**14**] A. Urushibara, Y. Moritomo, T. Arima, A. Asamitsu, G. Kido, and Y. Tokura "Insulator-metal transition and giant magnetoresistance in $La_{1-x}Sr_xMnO_3$" Phys Rev B **51**, 14103 (1995).

[**15**] H. Kawano, R. Kajimoto, M. Kubota, and H. Yoshizawa "Ferromagnetism-induced reentrant structural transition and phase diagram of the lightly doped insulator $La_{1-x}Sr_xMnO_3$ ($x \le 0.17$)" Phys Rev B **53**, R14709 (1996).

[**16**] T. Kimura, Y. Tomioka, H. Kuwahara, A. Asamitsu, M. Tamura, and Y. Tokura "Interplane tunneling magnetoresistance in a layered manganite crystal" Science **274**, 1698 (1996).

[**17**] T. G. Perring, G. Aeppli, T. Kimura, Y. Tokura, and M. A. Adams "Ordered stack of spin valves in a layered magnetoresistive perovskite" Phys Rev B **58**, R14693 (1998).

[**18**] M. Kubota, H. Fujioka, K. Hirota, K. Ohoyama, Y. Moritomo, H. Yoshizawa, and Y. Endoh "Relation between crystal and magnetic structures of layered manganite $La_{2-2x}Sr_{1+2x}Mn_2O_7$ ($0.30 \le x \le 0.50$)" J Phys Soc Jpn **69**, 1606 (2000).

[**19**] D. N. Argyriou, J. F. Mitchell, P. G. Radaelli, H. N. Bordallo, D. E. Cox, M. Medarde, and J. D. Jorgensen "Lattice effects and magnetic structure in the layered colossal magnetoresistance manganite $La_{2-2x}Sr_{1+2x}Mn_2O_7$, x=0.3" Phys Rev B **59**, 8695 (1999).

[**20**] A. Gupta and J. Z. Sun "Spin-polarized transport and magnetoresistance in magnetic oxides" J Magn Magn Mater **200**, 24 (1999).

[**21**] T. Kimura, Y. Tomioka, A. Asamitsu, and Y. Tokura "Anisotropic magnetoelastic phenomena in layered manganite crystals: Implication of change in orbital state" Phys Rev Lett **81**, 5920 (1998).

[**22**] C. D. Ling, J. E. Millburn, J. F. Mitchell, D. N. Argyriou, J. Linton, and H. N. Bordallo "Interplay of spin and orbital ordering in the layered colossal magnetoresistance manganite $La_{2-2x}Sr_{1+2x}Mn_2O_7$ ($0.5 \leq x \leq 1.0$)" Phys Rev B **62**, 15096 (2000).

[**23**] H. Kuwahara and Y. Tokura "***Colossal magnetoresistance, charge ordering and related properties of manganese oxides***" (World Scientific, Singapore, 1998).

[**24**] Y. Tokura "***Colossal magnetoresistive oxides***" (Gordon and Breach Science Publishers, 2000).

[**25**] T. Kimura and Y. Tokura "Layered magnetic manganites" Annu Rev Mater Sci **30**, 451 (2000).

[**26**] Y. Moritomo, A. Asamitsu, H. Kuwahara, and Y. Tokura "Giant magnetoresistance of manganese oxides with a layered perovskite structure" Nature **380**, 141 (1996).

[**27**] C. N. R. Rao, P. Ganguly, K. K. Singh, and R. A. M. Ram "A comparative study of the magnetic and electrical properties of perovskite oxides and the corresponding two-dimensional oxides of K_2NiF_4 structure" J Solid State Chem **72**, 14 (1988).

[**28**] Y. Moritomo, Y. Tomioka, A. Asamitsu, Y. Tokura, and Y. Matsui "Magnetic and electronic properties in hole-doped manganese oxides with layered structures: $La_{1-x}Sr_{1+x}MnO_4$" Phys Rev B **51**, 3297 (1995).

[**29**] Y. Moritomo, A. Nakamura, S. Mori, N. Yamamoto, K. Ohoyama, and M. Ohashi "Lattice effects on the charge-ordering transition in $R_{0.5}Sr_{1.5}MnO_4$" Phys Rev B **56**, 14879 (1997).

[**30**] M. Tokunaga, N. Miura, Y. Moritomo, and Y. Tokura "High-field magnetization and magnetoresistance of $La_{0.5}Sr_{1.5}MnO_4$" Phys Rev B **59**, 11151 (1999).

[**31**] C. Baumann, G. Allodi, B. Büchner, R. De Renzi, P. Reutler, and A. Revcolevschi "Magnetism of $La_{1-x}Sr_{1+x}MnO_4$ as revealed by μSR" Physica B **326**, 505 (2003).

[**32**] D. Senff, et al. "Crystal and magnetic structure of $La_{1-x}Sr_{1+x}MnO_4$: Role of the orbital degree of freedom" Phys Rev B **71**, 024425 (2005).

[**33**] B. J. Sternlieb, J. P. Hill, U. C. Wildgruber, G. M. Luke, B. Nachumi, Y. Moritomo, and Y. Tokura "Charge and magnetic order in $La_{0.5}Sr_{1.5}MnO_4$" Phys Rev Lett **76**, 2169 (1996).

[**34**] R. Klingeler, D. Bruns, C. Baumann, P. Reutler, A. Revcolevschi, and B. Büchner "Temperature driven orbital redistribution in $La_{1-x}Sr_{1+x}MnO_4$" J Magn Magn Mater **290-291**, 944 (2005).

[**35**] S. Larochelle, A. Mehta, L. Lu, P. K. Mang, O. P. Vajk, N. Kaneko, J. W. Lynn, L. Zhou, and M. Greven "Structural and magnetic properties of the single-layer manganese oxide $La_{1-x}Sr_{1+x}MnO_4$" Phys Rev B **71**, 024435 (2005).

[**36**] T. Ogasawara, T. Kimura, T. Ishikawa, M. Kuwata-Gonokami, and Y. Tokura "Dynamics of photoinduced melting of charge/orbital order in a layered manganite $La_{0.5}Sr_{1.5}MnO_4$" Phys Rev B **63**, 113105 (2001).

[**37**] T. Ogasawara, T. Kise, T. Ishikawa, M. Kuwata-Gonokami, and Y. Tokura "Photo-destruction of charge/orbital order in layered perovskite manganite: $La_{0.5}Sr_{1.5}MnO_4$" J Lumin **87–89**, 639 (2000).

[**38**] J. B. Torrance, P. Lacorre, A. I. Nazzal, E. J. Ansaldo, and C. Niedermayer "Systematic study of insulator-metal transitions in perovskites $R NiO_3$ (R = Pr, Nd, Sm, Eu) due to closing of charge-transfer gap" Phys Rev B **45**, 8209 (1992).

[**39**] Y. Tokura and N. Nagaosa "Orbital physics in transition-metal oxides" Science **288**, 462 (2000).

[**40**] R. D. Shannon "Revised effective ionic radii and systematic studies of interatomic distances in halides and chalcogenides" Acta Crystallogr A **32**, 751 (1976).

[**41**] H. Kawano, R. Kajimoto, H. Yoshizawa, Y. Tomioka, H. Kuwahara, and Y. Tokura "Magnetic ordering and relation to the metal-insulator transition in $Pr_{1-x}Sr_xMnO_3$ and $Nd_{1-x}Sr_xMnO_3$ with $x \sim 1/2$" Phys Rev Lett **78**, 4253 (1997).

[**42**] Y. Tomioka, A. Asamitsu, H. Kuwahara, Y. Moritomo, and Y. Tokura "Magnetic-field-induced metal-insulator phenomena in $Pr_{1-x}Ca_xMnO_3$ with controlled charge-ordering instability" Phys Rev B **53**, R1689 (1996).

[**43**] K. Liu, X. W. Wu, K. H. Ahn, T. Sulchek, C. L. Chien, and J. Q. Xiao "Charge ordering and magnetoresistance in $Nd_{1-x}Ca_xMnO_3$ due to reduced double exchange" Phys Rev B **54**, 3007 (1996).

[**44**] Y. Tomioka, A. Asamitsu, H. Kuwahara, Y. Moritomo, M. Kasai, R. Kumai, and Y. Tokura "Magnetic-field-induced metal-insulator transition in perovskite-type manganese oxides" Physica B: Condensed Matter **237–238**, 6 (1997).

[**45**] Y. Tokura "Critical features of colossal magnetoresistive manganites" Reports on Progress in Physics **69**, 797 (2006).

[**46**] C. N. R. Rao, A. Arulraj, A. K. Cheetham, and B. Raveau "Charge ordering in the rare earth manganates: the experimental situation" Journal of Physics: Condensed Matter **12**, R83 (2000).

[**47**] M. B. Salamon and M. Jaime "The physics of manganites: Structure and transport" Rev Mod Phys **73**, 583 (2001).

[**48**] E. Dagotto, T. Hotta, and A. Moreo "Colossal magnetoresistant materials: The key role of phase separation" Physics Reports **344**, 1 (2001).

[**49**] Y. Murakami, et al. "Resonant x-ray scattering from orbital ordering in $LaMnO_3$" Phys Rev Lett **81**, 582 (1998).

[**50**] Y. Tokura and Y. Tomioka "Colossal magnetoresistive manganites" J Magn Magn Mater **200**, 1 (1999).

[**51**] K. Tobe, T. Kimura, and Y. Tokura "Anisotropic optical spectra of doped manganites with pseudocubic perovskite structure" Phys Rev B **69**, 014407 (2004).

[**52**] Y. Moritomo, T. Akimoto, A. Nakamura, K. Ohoyama, and M. Ohashi "Antiferromagnetic metallic state in the heavily doped region of perovskite manganites" Phys Rev B **58**, 5544 (1998).

[**53**] R. Maezono, S. Ishihara, and N. Nagaosa "Phase diagram of manganese oxides" Phys Rev B **58**, 11583 (1998).

[**54**] H. Kuwahara, Y. Tomioka, A. Asamitsu, Y. Moritomo, and Y. Tokura "A first-order phase-transition induced by a magnetic-field" Science **270**, 961 (1995).

[**55**] Y. Murakami, H. Kawada, H. Kawata, M. Tanaka, T. Arima, Y. Moritomo, and Y. Tokura "Direct observation of charge and orbital ordering in $La_{0.5}Sr_{1.5}MnO_4$" Phys Rev Lett **80**, 1932 (1998).

[**56**] T. Ishikawa, K. Ookura, and Y. Tokura "Optical response to orbital and charge ordering in a layered manganite: $La_{1/2}Sr_{3/2}MnO_4$" Phys Rev B **59**, 8367 (1999).

[**57**] J. H. Jung, J. S. Ahn, J. Yu, T. W. Noh, J. Lee, Y. Moritomo, I. Solovyev, and K. Terakura "Optical investigations of the charge gap in orbital-ordered $La_{1/2}Sr_{3/2}MnO_4$" Phys Rev B **61**, 6902 (2000).

[**58**] D. S. Dessau, Y. D. Chuang, A. Gromko, T. Saitoh, T. Kimura, and Y. Tokura "Electronic structure of CMR oxides: high resolution electron-spectroscopic studies and a pseudogap" J Electron Spectrosc **117-118**, 265 (2001).

[**59**] D. J. Huang, et al. "Orbital ordering in $La_{0.5}Sr_{1.5}MnO_4$ studied by soft x-ray linear dichroism" Phys Rev Lett **92**, 087202 (2004).

[**60**] W. B. Wu, et al. "Orbital polarization of $LaSrMnO_4$ studied by soft x-ray linear dichroism" J Electron Spectrosc **137**, 641 (2004).

[**61**] J. Herrero-Martín, J. García, G. Subías, J. Blasco, and M. C. Sánchez "Polarized x-ray absorption spectra of $La_{1-x}Sr_{1+x}MnO_4$: Electronic state of Mn atoms" Phys Rev B **72**, 085105 (2005).

[**62**] K. Kuepper, R. Klingeler, P. Reutler, B. Büchner, and M. Neumann "Excited and ground state properties of $LaSrMnO_4$: A combined X-ray spectroscopic study" Phys Rev B **74**, 115103 (2006).

[**63**] M. Merz, P. Reutler, B. Büchner, D. Arena, J. Dvorak, Y. U. Idzerda, S. Tokumitsu, and S. Schuppler "O1*s* and Mn2*p* NEXAFS on single-layered $La_{1-x}Sr_{1+x}MnO_4$: Crystal field effect versus orbital coupling mechanism" Eur Phys J B **51**, 315 (2006).

[**64**] D. Senff, O. Schumann, M. Benomar, M. Kriener, T. Lorenz, Y. Sidis, K. Habicht, P. Link, and M. Braden "Melting of magnetic correlations in charge-orbital ordered $La_{1/2}Sr_{3/2}MnO_4$: Competition of ferromagnetic and antiferromagnetic states" Phys Rev B **77**, 184413 (2008).

[**65**] S. Ishihara and S. Maekawa "Theory of anomalous x-ray scattering in orbital-ordered manganites" Phys Rev Lett **80**, 3799 (1998).

[**66**] M. Benfatto, Y. Joly, and C. R. Natoli "Critical reexamination of the experimental evidence of orbital ordering in $LaMnO_3$ and $La_{0.5}Sr_{1.5}MnO_4$" Phys Rev Lett **83**, 636 (1999).

[**67**] I. S. Elfimov, V. I. Anisimov, and G. A. Sawatzky "Orbital ordering, Jahn-Teller distortion, and anomalous x-ray scattering in manganates" Phys Rev Lett **82**, 4264 (1999).

[**68**] P. Mahadevan, K. Terakura, and D. D. Sarma "Spin, charge, and orbital ordering in $La_{0.5}Sr_{1.5}MnO_4$" Phys Rev Lett **87**, 066404 (2001).

[**69**] S. B. Wilkins, P. D. Spencer, P. D. Hatton, S. P. Collins, M. D. Roper, D. Prabhakaran, and A. T. Boothroyd "Direct observation of orbital ordering in $La_{0.5}Sr_{1.5}MnO_4$ using soft x-ray diffraction" Phys Rev Lett **91**, 167205 (2003).

[**70**] C. W. M. Castleton and M. Altarelli "Orbital ordering in the manganites: Resonant x-ray scattering predictions at the manganese L_{II} and L_{III} edges" Phys Rev B **62**, 1033 (2000).

[**71**] S. S. Dhesi, et al. "Unraveling orbital ordering in $La_{0.5}Sr_{1.5}MnO_4$" Phys Rev Lett **92**, 056403 (2004).

[**72**] C. H. Chen, S. W. Cheong, and A. S. Cooper "Charge modulations in $La_{2-x}Sr_xNiO_{4+y}$: Ordering of polarons" Phys Rev Lett **71**, 2461 (1993).

[**73**] J. M. Tranquada, J. E. Lorenzo, D. J. Buttrey, and V. Sachan "Cooperative ordering of holes and spins in $La_2NiO_{4.125}$" Phys Rev B **52**, 3581 (1995).

[**74**] J. M. Tranquada, B. J. Sternlieb, J. D. Axe, Y. Nakamura, and S. Uchida "Evidence for stripe correlations of spins and holes in copper oxide superconductors" Nature **375**, 561 (1995).

[**75**] S. W. Cheong, G. Aeppli, T. E. Mason, H. Mook, S. M. Hayden, P. C. Canfield, Z. Fisk, K. N. Clausen, and J. L. Martinez "Incommensurate magnetic fluctuations in $La_{2-x}Sr_xCuO_4$" Phys Rev Lett **67**, 1791 (1991).

[**76**] B. Lake, et al. "Antiferromagnetic order induced by an applied magnetic field in a high-temperature superconductor" Nature **415**, 299 (2002).

[**77**] Q. Li, M. Hücker, G. D. Gu, A. M. Tsvelik, and J. M. Tranquada "Two-dimensional superconducting fluctuations in stripe-ordered $La_{1.875}Ba_{0.125}CuO_4$" Phys Rev Lett **99**, 067001 (2007).

[**78**] S. Larochelle, A. Mehta, N. Kaneko, P. K. Mang, A. F. Panchula, L. Zhou, J. Arthur, and M. Greven "Nature of e_g Electron Order in $La_{1-x}Sr_{1+x}MnO_4$" Phys Rev Lett **87**, 095502 (2001).

[**79**] W. Norimatsu and Y. Koyama "Evolution of orthorhombic domain structures during the tetragonal-to-orthorhombic phase transition in the layered perovskite $Sr_{2-x}La_xMnO_4$" Phys Rev B **74**, 085113 (2006).

[**80**] K. H. Ahn, T. Lookman, and A. R. Bishop "Strain-induced metal-insulator phase coexistence in perovskite manganites" Nature **428**, 401 (2004).

[**81**] M. Arao, Y. Inoue, K. Toyoda, and Y. Koyama "Transverse and longitudinal lattice modulations in the charge-orbital-ordered manganite $Sr_{2-x}La_xMnO_4$ around $x = 0.5$" Phys Rev B **84**, 014102 (2011).

[**82**] H. Ulbrich, D. Senff, P. Steffens, O. J. Schumann, Y. Sidis, P. Reutler, A. Revcolevschi, and M. Braden "Evidence for charge orbital and spin stripe order in an overdoped manganite" Phys Rev Lett **106**, 157201 (2011).

[**83**] J. Herrero-Martín, J. Blasco, J. García, G. Subías, and C. Mazzoli "Structural changes at the semiconductor-insulator phase transition in the single-layered perovskite $La_{0.5}Sr_{1.5}MnO_4$" Phys Rev B **83**, 184101 (2011).

[**84**] J. Herrero-Martín, J. García, J. Blasco, and G. Subías "Mn *K* edge resonant x-ray scattering of half-doped manganites" European Physical Journal-Special Topics **208**, 107 (2012).

[**85**] J. García, J. Herrero-Martín, G. Subías, J. Blasco, J. S. Andreu, and M. C. Sánchez "Incommensurate sinusoidal oxygen modulations in layered manganites $La_{1-x}Sr_{1+x}MnO_4$ ($x \geq 0.5$)" Phys Rev Lett **109**, 107202 (2012).

[**86**] A. Biswas, M. Rajeswari, R. C. Srivastava, Y. H. Li, T. Venkatesan, R. L. Greene, and A. J. Millis "Two-phase behavior in strained thin films of hole-doped manganites" Phys Rev B **61**, 9665 (2000).

[**87**] J. Klein, J. B. Philipp, G. Carbone, A. Vigliante, L. Alff, and R. Gross "Transport anisotropy in biaxially strained $La_{2/3}Ca_{1/3}MnO_3$ thin films" Phys Rev B **66**, 052414 (2002).

[**88**] M. Ziese, H. C. Semmelhack, K. H. Han, S. P. Sena, and H. J. Blythe "Thickness dependent magnetic and magnetotransport properties of strain-relaxed $La_{0.7}Ca_{0.3}MnO_3$ films" J Appl Phys **91**, 9930 (2002).

[**89**] Y. Konishi, Z. Fang, M. Izumi, T. Manako, M. Kasai, H. Kuwahara, M. Kawasaki, K. Terakura, and Y. Tokura "Orbital-state-mediated phase-control of manganites" J Phys Soc Jpn **68**, 3790 (1999).

[**90**] Z. Fang, I. V. Solovyev, and K. Terakura "Phase diagram of tetragonal manganites" Phys Rev Lett **84**, 3169 (2000).

[**91**] D. B. Chrisey and G. K. Hubler "***Pulsed laser deposition of thin films***" (John Wiley & Sons, Inc., United States of America, 1994).

[**92**] R. Eason "***Pulsed laser deposition of thin films: Applications-led growth of functional materials***" (John Wiely & Sons, Inc., United States of America, 2007).

[**93**] A. N. Grundy, M. Chen, B. Hallstedt, and L. J. Gauckler "Assessment of the La-Mn-O system" J Phase Equilib Diff **26**, 131 (2005).

[**94**] A. N. Grundy, B. Hallstedt, and L. J. Gauckler "Assessment of the Sr-Mn-O system" J Phase Equilib Diff **25**, 311 (2004).

[**95**] A. N. Grundy, B. Hallstedt, and L. J. Gauckler "Assessment of the La-Sr-Mn-O system" Calphad **28**, 191 (2004).

[**96**] J. Als-Nielsen and D. McMorrow "***Elements of modern x-ray physics***" (John Wiley & Sons, Ltd., England, 2001).

[**97**] M. Birkholz, P. F. Fewster, and C. Genzel "***Thin film analysis by x-ray scattering***" (Wiley-VCH Verlag GmbH & Co. KGaA, Germany, 2005).

[**98**] D. K. Bowen and B. K. Tanner "***High resolution x-ray diffractometry and topography***" (Taylor & Francis Ltd., United Kingdom, 1998).

[**99**] B. D. Cullity "***Elements of x-ray diffraction***" (Addison-Wesley Publishing Co., Inc., United States of America, 1956).

[**100**] M. M. Woolfson "***An inroduction to x-ray crystallography***" (Cambridge University Press, United Kingdom, 1997).

[**101**] K. Tezuka, M. Inamura, Y. Hinatsu, Y. Shimojo, and Y. Morii "Crystal structures and magnetic properties of $Ca_{2-x}Sr_xMnO_4$" J Solid State Chem **145**, 705 (1999).

[**102**] C. S. Hong, E. O. Chi, W. S. Kim, N. H. Hur, K. W. Lee, and C. H. Lee "Magnetic properties and structural evolution in $Nd_{0.5}Sr_{1.5}MnO_4$" Chem Mater **13**, 945 (2001).

[**103**] J. F. Mitchell, J. E. Millburn, M. Medarde, S. Short, J. D. Jorgensen, and M. T. Fernández-Díaz "$Sr_3Mn_2O_7$: Mn^{4+} parent compound of the *n*=2 layered CMR manganites" J Solid State Chem **141**, 599 (1998).

[**104**] T. Akimoto, Y. Moritomo, K. Ohoyama, S. Okamoto, S. Ishihara, S. Maekawa, and A. Nakamura "Interrelation between orbital polarization and magnetic structure in bilayer manganites" Phys Rev B **59**, R14153 (1999).

[**105**] L. Malavasi, E. Di Tullio, H. Ründlof, C. Tealdi, and G. Flor "High-temperature neutron diffraction study of the bilayered manganite $La_{1.4}Sr_{1.6}Mn_2O_7$" Phys Rev B **72**, 054115 (2005).

[**106**] I. B. Sharma and D. Singh "Preparation and study of structural, electrical and magnetic properties of $La_2SrFe_2O_7$ and $La_2SrMn_2O_7$" Journal of Chemical Sciences **107**, 189 (1995).

[**107**] G. Linker, R. Smithey, J. Geerk, F. Ratzel, R. Schneider, and A. Zaitsev "The growth of ultra-thin epitaxial CeO_2 films on r-plane sapphire" Thin Solid Films **471**, 320 (2005).

[**108**] M. Huijben, L. W. Martin, Y. H. Chu, M. B. Holcomb, P. Yu, G. Rijnders, D. H. A. Blank, and R. Ramesh "Critical thickness and orbital ordering in ultrathin $La_{0.7}Sr_{0.3}MnO_3$ films" Phys Rev B **78**, 094413 (2008).

[**109**] D. Pesquera, G. Herranz, A. Barla, E. Pellegrin, F. Bondino, E. Magnano, F. Sánchez, and J. Fontcuberta "Surface symmetry-breaking and strain effects on orbital occupancy in transition metal perovskite epitaxial films" Nature Communications **3**, 1 (2012).

[**110**] F. Bassani, G. L. Liedl, and P. Wyder "***Encyclopedia of condensed matter physics***" (Elsevier Academic Press, 2005).

[**111**] D. Briggs and M. Seah "***Practical surface analysis, auger and x-ray photoelectron spectroscopy***" (John Wiley ans Sons, Ltd., 1996).

[**112**] G. Gauglitz and T. Vo-Dinh "***Handbook of spectroscopy***" (Wiely-VCH Verlag GmbH & Co., Germany, 2003).

[**113**] J. F. Moulder, W. F. Stickle, P. E. Sobol, and K. D. Bomben "***Handbook of X-ray Photoelectron Spectroscopy***" (Physical Electronics, Inc., Minnesota, 1995).

[**114**] J. C. Fuggle, M. Campagna, Z. Zolnierek, R. Lässer, and A. Platau "Observation of a relationship between core-level line shapes in photoelectron spectroscopy and the localization of screening orbitals" Phys Rev Lett **45**, 1597 (1980).

[**115**] S. Tougaard "Practical algorithm for background subtraction" Surf Sci **216**, 343 (1989).

[**116**] M. F. Sunding, K. Hadidi, S. Diplas, O. M. Løvvik, T. E. Norby, and A. E. Gunnæs "XPS characterisation of *in situ* treated lanthanum oxide and hydroxide using tailored charge referencing and peak fitting procedures" J Electron Spectrosc **184**, 399 (2011).

[**117**] M. C. Biesinger, B. P. Payne, A. P. Grosvenor, L. W. M. Lau, A. R. Gerson, and R. S. C. Smart "Resolving surface chemical states in XPS analysis of first row transition metals, oxides and hydroxides: Cr, Mn, Fe, Co and Ni" Appl Surf Sci **257**, 2717 (2011).

[**118**] R. Bertacco, J. P. Contour, A. Barthélemy, and J. Olivier "Evidence for strontium segregation in $La_{0.7}Sr_{0.3}MnO_3$ thin films grown by pulsed laser deposition: consequences for tunnelling junctions" Surf Sci **511**, 366 (2002).

[**119**] T. T. Fister, D. D. Fong, J. A. Eastman, P. M. Baldo, M. J. Highland, P. H. Fuoss, K. R. Balasubramaniam, J. C. Meador, and P. A. Salvador "*In situ* characterization of strontium surface segregation in epitaxial $La_{0.7}Sr_{0.3}MnO_3$ thin films as a function of oxygen partial pressure" Appl Phys Lett **93**, 15904 (2008).

[**120**] K. Katsiev, B. Yildiz, K. Balasubramaniam, and P. A. Salvador "Electron tunneling characteristics on $La_{0.7}Sr_{0.3}MnO_3$ thin-film surfaces at high temperature" Appl Phys Lett **95**, 092106 (2009).

[**121**] P. Abellán, C. Moreno, F. Sandiumenge, X. Obradors, and M. J. Casanove "Misfit relaxation of $La_{0.7}Sr_{0.3}MnO_3$ thin films by a nanodot segregation mechanism" Appl Phys Lett **98**, 041903 (2011).

[**122**] Z. P. Li, et al. "Interface and surface cation stoichiometry modified by oxygen vacancies in epitaxial manganite films" Adv Funct Mater **22**, 4312 (2012).

[**123**] J. Y. Son, T. Mizokawa, J. W. Quilty, S. Hirata, K. Takubo, T. Kimura, and Y. Tokura "Electronic structure of $La_{2-2x}Sr_{1+2x}Mn_2O_7$ studied by x-ray photoemission spectroscopy" Phys Rev B **70**, 012411 (2004).

[**124**] K. Kuepper, R. Klingeler, P. Reutler, B. Büchner, and M. Neumann "Electronic structure of $LaSrMnO_4$: X-ray photoelectron spectroscopy and x-ray emission spectroscopy studies" J Appl Phys **99**, 08Q308 (2006).

[**125**] D. S. Dessau, T. Saitoh, C. H. Park, Z. X. Shen, P. Villella, N. Hamada, Y. Moritomo, and Y. Tokura "κ-dependent electronic structure, a large "ghost" Fermi surface, and a pseudogap in a layered magnetoresistive oxide" Phys Rev Lett **81**, 192 (1998).

[**126**] T. Saitoh, A. E. Bocquet, T. Mizokawa, H. Namatame, A. Fujimori, M. Abbate, Y. Takeda, and M. Takano "Electronic structure of $La_{1-x}Sr_xMnO_3$ studied by photoemission and x-ray-absorption spectroscopy" Phys Rev B **51**, 13942 (1995).

[**127**] D. Attwood "***Soft x-ray and extreme ultraviolet radiation***" (Cambridge University Press, United States of America, 1999).

[**128**] G. Bunker "***Introduction to XAFS: A practical guide to x-ray absorption fine structure spectroscopy***" (Cambridge University Press, United States of America, 2010).

[**129**] F. de Groot "High resolution x-ray emission and x-ray absorption spectroscopy" Chem Rev **101**, 1779 (2001).

[**130**] F. de Groot "Multiplet effects in x-ray spectroscopy" Coordin Chem Rev **249**, 31 (2005).

[**131**] J. Stöhr "***NEXAFS Spectroscopy***" (Springer-Verlag United States of America, 1996).

[**132**] D. H. McDaniel "Spin factoring as an aid in the determination of spectroscopic terms" Journal of Chemical Education **54**, 147 (1977).

[**133**] E. Stavitski and F. M. F. de Groot "The CTM4XAS program for EELS and XAS spectral shape analysis of transition metal *L* edges" Micron **41**, 687 (2010).

[**134**] H. Wu, et al. "Orbital order in $La_{0.5}Sr_{1.5}MnO_4$: Beyond a common local Jahn-Teller picture" Phys Rev B **84**, 155126 (2011).

[**135**] S. B. Wilkins, et al. "Resonant soft x-ray scattering investigation of orbital and magnetic ordering in $La_{0.5}Sr_{1.5}MnO_4$" Phys Rev B **71**, 245102 (2005).

[**136**] M. Merz, G. Roth, P. Reutler, B. Büchner, D. Arena, J. Dvorak, Y. U. Idzerda, S. Tokumitsu, and S. Schuppler "Orbital degree of freedom in single-layered $La_{1-x}Sr_{1+x}MnO_4$: Doping- and temperature-dependent rearrangement of orbital states" Phys Rev B **74**, 184414 (2006).

[**137**] P. F. Schofield, G. van der Laan, C. M. B. Henderson, and G. Cressey "A single crystal, linearly polarized Fe 2*p* x-ray absorption study of gillespite" Mineral Mag **62**, 65 (1998).

[**138**] G. van der Laan, B. T. Thole, G. A. Sawatzky, J. B. Goedkoop, J. C. Fuggle, J. M. Esteva, R. Karnatak, J. P. Remeika, and H. A. Dabkowska "Experimental proof of magnetic x-ray dichroism" Phys Rev B **34**, 6529 (1986).

[**139**] T. Konaka, M. Sato, H. Asano, and S. Kubo "Relative permittivity and dielectric loss tangent of substrate materials for high-T_C superconducting film" J Supercond **4**, 283 (1991).

[**140**] X. Q. Liu, X. M. Chen, and Y. Xiao "Preparation and characterization of $LaSrAlO_4$ microwave dielectric ceramics" Mat Sci Eng B-Solid **103**, 276 (2003).

[**141**] M. Abbate, et al. "Controlled-valence properties of $La_{1-x}Sr_xFeO_3$ and $La_{1-x}Sr_xMnO_3$ studied by soft-x-ray absorption spectroscopy" Phys Rev B **46**, 4511 (1992).

[**142**] H. Kanamori, T. Yoshioka, K. Hirose, and T. Yamamoto "Determination of valence state of Mn ions in $Pr_{1-x}A_xMnO_{3-\delta}$ (A = Ca, Sr) by Mn-L_3 x-ray absorption near-edge structure analysis" J Electron Spectrosc **185**, 129 (2012).

[**143**] W. Gudat and C. Kunz "Close similarity between photoelectric yield and photoabsorption spectra in soft-x-ray range" Phys Rev Lett **29**, 169 (1972).

[**144**] A. Tebano, et al. "Evidence of orbital reconstruction at interfaces in ultrathin $La_{0.67}Sr_{0.33}MnO_3$ films" Phys Rev Lett **100**, 137401 (2008).

[**145**] C. Aruta, G. Balestrino, A. Tebano, G. Ghiringhelli, and N. B. Brookes "Cooperative enhancement of in-plane orbital ordering by oxygen deficiency and in-plane tensile strain in $La_{0.7}Sr_{0.3}MnO_{3-\delta}$ thin films" Epl-Europhys Lett **80**, 37003 (2007).

[**146**] C. Aruta, G. Ghiringhelli, V. Bisogni, L. Braicovich, N. B. Brookes, A. Tebano, and G. Balestrino "Orbital occupation, atomic moments, and magnetic ordering at interfaces of manganite thin films" Phys Rev B **80**, 014431 (2009).

[**147**] C. Aruta, G. Ghiringhelli, A. Tebano, N. G. Boggio, N. B. Brookes, P. G. Medaglia, and G. Balestrino "Strain induced x-ray absorption linear dichroism in $La_{0.7}Sr_{0.3}MnO_3$ thin films" Phys Rev B **73**, 235121 (2006).

[**148**] W. B. Wu, D. J. Huang, C. M. Huang, C. H. Hsu, C. F. Chang, H. J. Lin, and C. T. Chen "Orbital polarization and Jahn-Teller distortion of strained $La_{0.5}Sr_{0.5}MnO_3$ thin films" J Magn Magn Mater **310**, 813 (2007).

[**149**] H. B. Huang, T. Shishidou, and T. Jo "Strong linear dichroism in Mn $L_{2,3}$ absorption predicted for orbital ordering in $LaMnO_3$" J Phys Soc Jpn **69**, 2399 (2000).

[**150**] C. D. Wagner, L. E. Davis, M. V. Zeller, J. A. Taylor, R. H. Raymond, and L. H. Gale "Empirical atomic sensitivity factors for quantitative analysis by electron spectroscopy for chemical analysis" Surf Interface Anal **3**, 211 (1981).

[**151**] S. Tougaard and C. Jansson "Background correction in XPS: Comparison of validity of different methods" Surf Interface Anal **19**, 171 (1992).